DISS. ETH NO. 23153

Fundamental Studies on Effects of Carrier Gas Mixtures on Elemental Fractionation in Laser Ablation Inductively Coupled Plasma Mass Spectrometry

A thesis submitted to attain the degree of

DOCTOR OF SCIENCES of ETH ZURICH
(Dr. sc. ETH Zurich)

presented by
STEFFEN ALLNER

MSc. ETH in Chemistry, ETH Zurich

born on 09.11.1986

citizen of the Federal Republic of Germany

accepted on the recommendation of
Prof. Dr. Detlef Günther, examiner
Prof. Dr. Thomas Lippert, co-examiner
Dr. Joachim Koch, co-examiner

2015

δὶς ἐς τὸν αὐτὸν ποταμὸν οὐκ ἂν ἐμβαίης.
You could not step twice into the same river.

(Heraclitus of Ephesus)

Contents

Abstract

In recent years, geochronology, the science of assigning an age to a geological object, has become an important application of laser ablation coupled to inductively coupled plasma mass spectrometry (LA-ICPMS). Advantages such as high sensitivity, high sample throughput and high spatial resolution on the sample have contributed to its wide use, which also includes the analysis of zircon ($ZrSiO_4$). Because of the high U^{4+} and low Pb^{2+} inclusion into the crystal lattice during crystallisation, zircons often allow single grain U-Pb age determination.

Besides these advantages of LA-ICPMS, there are also some remaining challenges. One of them is matrix matching for calibration leading to accurate results, but finding zircons for perfect matrix matching is not trivial. The reason is a phenomenon termed *down-hole fractionation*, *i.e.* the change of Pb/U ratio over the ablation process, which is not identical for all zircons.

To investigate the influence of the laser ablation (LA) process on the result of the measurement, a separation of the fractionation originating from the variation in the ablation conditions and from the ICPMS was performed. In this work, this was realised using a gas exchange device (GED). This device facilitates an exchange of carrier gas (e.g. He → Ar) and, therefore, experiments with different conditions in the ablation process while maintaining

constant conditions at the ICPMS site and vice versa. The conditions were altered by mixing N_2, O_2, H_2, and H_2O to the carrier gas, thus changing the gas composition present in the system. The gases were added in two different amounts for each gas and three different reference materials were measured: NIST SRM 610 glass standard (NIST 610), and two natural zircon reference materials 91500 and Plešovice. In the setup, two different laser systems were employed to investigate the effect on nanosecond (ns) and femtosecond (fs) ablation using an ArF excimer system operating at a wavelength of 193 nm and a Yb:KGW solid state system at 257 nm. These systems were coupled with a GED, which was in turn connected to a quadrupole ICPMS.

A two-fold strategy was used for the analysis of the transient $^{206}Pb/^{238}U$ signals. First, the acquired signals were integrated over the ablation time and the resulting ratios were compared. In a second step, a linear regression was applied to the transient signals of all measurements and the intercept was interpreted as a measure for mass bias in the ICP, and the slope as a measure for the laser-induced down-hole fractionation during the ablation.

When using ns-LA, the general influence of diatomic gases in the carrier gas mixture was predominantly on the ICP site. For example, the $^{206}Pb/^{238}U$ ratio for the addition of 10 mL/min O_2 resulted in a decrease of approximately 35 %, 25 %, and 20 % of NIST 610, 91500, and Plešovice, respectively, regardless of whether the gases were introduced before the ablation chamber or directly before the ICP. When the gases were added before the ablation chamber and exchanged via GED, such deviation was not observed. For the slope, on the other hand, a difference from the He-only conditions could be seen for the addition of H_2O to the carrier gas. The slope was lowered and eventually turned negative. Thus, it can be concluded that the addition of H_2O can change the fractionation behaviour.

The age of Plešovice, determined with 91500 as reference and conventional signal inte-

gration, showed no reduction in deviation from the accepted age in most cases, regardless of the type of gas addition. Therefore, no systematic improvement by changing the ablation or plasma condition was observed.

Under corresponding conditions, the experiments with fs-LA produced signals that were less stable when compared to ns-LA. While it was possible to apply 600 shots on a spot with 24 µm diameter using the ns-LA, only 200 to 300 shots could be applied with the fs-LA before the overall signal declined to background level. The addition of H_2O in this case reduced the down-hole fractionation at the LA, but also increased the fractionation, when added before the ICP. The resulting ages were by trend approximately 10 Ma (3 %) older than with ns-LA and showed a larger variation (-3 % to +19 %). Fs-LA was found to be less robust to gas impurities than ns-LA.

Besides the well established U-Pb decay system, other decay systems are investigated by geochemists to provide an additional way to cross-validate the age of a rock, or to unlock other minerals for radiometric dating purposes. One of these systems with potential application for lanthanide rich minerals is the La-Ba decay system ($^{138}La \rightarrow {}^{138}Ba$). To enable the analysis by LA-ICPMS, an online separation procedure for ^{138}La and ^{138}Ba has to be developed. Here, O_2 was mixed into the carrier gas to enable a separation by selective oxidation of La. This allowed a reduction of ^{138}La vs. ^{138}Ba down to 0.1 % at a concentration ratio of La:Ba of 1000:1, which equals to a suppression factor of approximately 1000. These results were achieved by introducing desolvated aerosol into a quadrupole ICPMS and reproduced on a multicollector inductively coupled plasma mass spectrometry (MC-ICPMS). Furthermore, different detector configurations for the MC-ICPMS were tested and evaluated with the La-Ba system. This proof of concept is the foundation for analysis of La-Ba ages with LA-ICPMS.

Zusammenfassung

Geochronologie, die Wissenschaft einem geologischen Objekt ein Alter zuzuweisen, ist in den letzten Jahren zu einer wichtigen Anwendung von Laserablation in Kombination mit induktiv gekoppelter Plasma-Massenspektrometrie (LA-ICPMS) geworden. Vorteile wie hohe Sensitivität, schneller Probendurchsatz und hoher Ortsauflösung auf der Probenoberfläche haben zu der weiten Anwendbarkeit beigetragen, zu der auch die Analyse von Zirkonen ($ZrSiO_4$) gehört. Aufgrund des Einschlusses von U^{4+} und des Ausschlusses von Pb^{2+} während der Kristallisation ist es bei Zirkonen oft möglich, mittels U-Pb Datierung das Alter einzelner Kristalle zu bestimmen.

Neben den Vorteilen der LA-ICPMS existieren auch noch offene Herausforderungen: Matrixanpassung ist die bevorzugte Methode um eine korrekte Kalibration und entsprechend richtige Alter zu erhalten. Allerdings ist es nicht trivial, eine genau angepasste Zirkonmatrix zu finden. Die Fraktionierung im Ablationskrater, also die Veränderung des Pb/U Verhältnisses über den Ablationsprozess, ist nicht identisch für alle Zirkone.

Um den Einfluss des Ablationsprozesses auf das Messresultat zu untersuchen, ist eine Differenzierung der Fraktionierung nach Herkunft, also entweder LA oder ICPMS, erforderlich. Dies wurde in der vorliegenden Arbeit mit einem Gasaustauscher (GED) untersucht. Der GED erlaubt den Austausch des Trägergases nach der Ablationszelle, beispielsweise

He → Ar, und somit die Messung unter wechselnden Bedingungen für den LA-Prozess bei konstanten Bedingungen im ICPMS und umgekehrt. Die Bedingungen wurden in den Experimenten durch das Hinzufügen von N_2, O_2, H_2 und H_2O zum Trägergas verändert. Die Zugabe erfolgte jeweils in zwei verschiedenen Konzentrationen. Gemessen wurden drei verschiedene Referenzmaterialien (Glasstandard NIST SRM 610 und zwei natürliche Zirkonrefenzmaterialien 91500 und Plešovice). Der experimentelle Aufbau bestand aus einem Agilent 7500cs Quadrupole-ICPMS, welches mit einem GED verbunden war. Um sowohl die Effekte bei Nanosekunden- und Femtosekundenablation zu untersuchen, wurden zwei verschiedene Lasersysteme eingesetzt: ein ArF Excimersystem mit einer Wellenlänge von 193 nm und ein Yb:KGW Festkörperlasersystem mit einer Wellenlänge von 257 nm.

Die transienten Signale wurden auf zwei Wegen analysiert: 1. Die Signale wurden über einen gewissen Zeitraum integriert und danach ihre Verhältnisse verglichen. 2. Auf die transienten Daten wurde eine lineare Regression angewandt, wobei der erhaltene Ordinatenabschnitt als Maß für die Massendiskriminierung im ICP und die Steigung als Maß für die vom Laser induzierte Fraktionierung über den Ablationsprozess interpretiert wurde.

Bei der Verwendung des ns-Lasers zeigte sich der Einfluss der zweiatomigen Gase vor allem im ICP. Zum Beispiel resultierte die Zugabe von 10 mL/min O_2 in einer Verringerung des $^{206}Pb/^{238}U$-Verhältnisses um 35 % für NIST 610, 25 % für 91500, und 20 % für Plešovice, unabhängig davon, ob die Zugabe vor der Ablationszelle oder erst direkt vor dem ICP erfolgte. Wurde das Trägergasgemisch nach der Zelle durch den Gasaustauscher ersetzt, zeigte sich keine Veränderung. Bei der Steigung wurde ein Unterschied nur bei der Addition von H_2 festgestellt. Da sich die Steigung verringerte und sogar ins negative veränderte, kann man darauf schließen, dass H_2 die Fraktionierung beeinflusst.

Bei dem bestimmten Alter von Plešovice, mit 91500 als Referenz, konnte keine Reduktion

in der Abweichung vom akzeptierten Alter festgestellt werden, und somit auch keine Verbesserung durch Veränderungen der Ablations- oder Plasmabedingungen.

Die Experimente mit dem fs-Laser sind nur schwer direkt mit den ns Experimenten vergleichbar, da die Signalstabilität grundverschieden war. Während es mit dem ns-Laser möglich war 600 Schüsse bei 24 µm Kraterdurchmesser zu ablatieren, konnten mit dem fs-Laser nur 200-300 Schüsse appliziert werden, bevor das Signal aller Isotope aus Mangel an ablatiertem Material abnahm.

Neben dem etablierten U-Pb-System werden in der Geochemie auch andere Zerfallssysteme untersucht, um entweder eine Kreuzvalidierung des Alters zu ermöglichen, oder um bisher schwer zugängliche Minerale auch für die Altersbestimmung zu erschließen. Eines dieser Systeme ist das La-Ba-System ($^{138}La \rightarrow {}^{138}Ba$), welches vorteilhaft für Minerale mit hohem Lanthanidenanteil ist. Um eine Analyse mittels LA-ICPMS zu ermöglichen, muss allerdings eine *in-situ* Trennung von ^{138}La und ^{138}Ba erfolgen.

Um eine Trennung mittels selektive Oxidation von La zu ermöglichen, wurde in dieser Arbeit O_2 zu dem Trägergas hinzugefügt. Damit wurde eine Reduktion von ^{138}La auf ^{138}Ba auf 0.1 % bei einem Konzentrationsverhältnis von La:Ba von 1000:1 erreicht. Dies entspricht einer Abschwächung um einen Faktor 1000. Diese Ergebnisse konnten mittels Eintrag von desolvatisiertem Aerosol in das Agilent 7500cs (Quadrupole-ICPMS) erreicht werden und waren auf einem NuPlasma Multikollektor-ICPMS (MC-ICPMS) reproduzierbar. Weiterhin wurden verschiedene Detektorkonfigurationen auf dem NuPlasma für die Benutzung mit dem La-Ba-System evaluiert.

Acknowledgements

First of all, I want to thank Detlef Günther, for directing me in the field of analytical chemistry at different parts of my scientific education and giving me the opportunity to do a PhD in his group. Furthermore, for providing space and time to work for myself and on my own and for the trust in me.

There are of course more people to thank, who have helped me over the time to do the research and to write this thesis in various ways:

Thomas Lippert and Joachim Koch for being co-referees for my thesis.

Caro for being with me in the group from the beginning and

Beni and Thomas for the Arbeitsbesprechungen and for interesting insights of the life in HCI.

Bodo for the help with broken instrument and critical questions in the group seminar.

Joachim for discussions about (fs-)lasers and the support in the second part of my PhD.

Nicole for always providing an helping hand and open ear when necessary.

Roland Mäder and the whole workshop of D-CHAB, for the quick response on small problems and for long discussion at PhD-aperos.

Alex for scientific discussions and for showing me together with *Abi* a different side of being American.

Adrian and Stefan being very interested semester students.

The running elements of the Günther group – Nicole, Sabrina, Caro, Daniel T., Daniel F., Julien, Frank, Alex, Debora and Lyndsey – for providing fresh air and fruitful discussion on the Gubrist.

The former and current inhabitants (Sabrina, Olga, Natalyia, Hao, Kathrin, Debora and Lyndsey) of G141 for sharing the view, the sweets and scientific discussions.

All the current and former members (Abi, Alex, Beni, Bodo, Caro, Ceren, Daniel F., Daniel T., Davide, Debora, Giovanni, Gisela, Gunnar, Hao, Joachim, Karin, Kathrin H., Kathrin L., Kevin, Ladina, Luca, Marcel B., Marcel G., Markus, Mattias, Mohamed, Natalyia, Nicole, Niko, Olga, Peter, Reto, Robert B., Robert K., Sabrina, Tatiana, Thomas) of the Günther group for building up and maintaining the knowledge, the methods and the infrastructure, which were the basis for this research, and of course for all discussions, coffee breaks and parties.

Remo, Lukas and Fabian for being excellent presidents of the VAC and to all members of the board for discussions about politics and for the events.

Mario for a different view on many topics, including the life after ETH.

Frali, Chris, Gasper, Veronica and Nicola for tastings and moral support.

Ein ganz besonderer Dank geht an meine Familie in Halle und Umgebung. Danke für die Inseln des Rückzugs, alle Hilfestellungen und die nötige Erdung. Ohne Euch wäre diese Arbeit nicht möglich gewesen.

Last, but not least, I want to thank Bettina for the distraction and dancing, when needed, but also for keeping the focus at the right time, for the patience and for all the other things.

Glossary

91500	a natural zircon reference material with an age of approximately 1065 Ma
AES	atomic emission spectroscopy
APD	aerosol penetration depth
DC	direct current
ETV	electrothermal vaporization
excimer	excited dimer
fs	femtosecond, 10^{-15} s
Ga	billion years, 10^{9} a
GED	gas exchange device
ICP	inductively coupled plasma
ICP-OES	inductively coupled plasma optical emission spectroscopy
ICPMS	inductively coupled plasma mass spectrometry
ID-TIMS	isotope dilution-thermal ionisation mass spectrometry
LA	laser ablation

LA-ICPMS	laser ablation coupled to inductively coupled plasma mass spectrometry
LOD	limit of detection
m/z	mass to charge ratio
Ma	million years, 10^6 a
MC-ICPMS	multicollector inductively coupled plasma mass spectrometry
MES	multi-element solution
MGG	metallic gas generator
MOR	mean of ratios
MS	mass spectrometry
Nd:YAG	neodymium-doped yttrium aluminium garnet; $Nd:Y_3Al_5O_{12}$
NIR	near-infrared
NIST 610	NIST SRM 610 glass standard
ns	nanosecond, 10^{-9} s
PLD	pulsed laser depositin
Plešovice	a natural zircon reference material with an age of approximately 337 Ma
ps	picosecond, 10^{-12} s
PSD	particle size distribution
REE	rare earth elements: scandium, yttrium, lanthanides

RF	radiofrequency
RH	relative humidity
ROM	ratio of means
SEM	scanning electron microscopy
SEM	secondary electron multiplier
SES	single-element solution
SHRIMP	sensitive high mass-resolution ion microprobe
SIMS	secondary ion mass spectrometry
SN	solution nebulisation
t	tetragonal
UV	utraviolet
Yb:KGW	ytterbium-doped potassium gadolinium tungstate; Yb:$KGd(WO_4)_2$
zircon	$ZrSiO_4$, accessory mineral used for age determination

1. Introduction

1.1. Geochronology

Age is an important topic for every human. Our own ages can be counted from the years passing by usually at birthdays. In contrast to human ageing, which is a fairly continuous process, the age of a tree is counted by the number of yearly developed rings in the cross-section of a trunk. Here, a periodically changing pattern in the environment is responsible for a change in the properties of the trunk. Similar to tree rings, layers in geological formations show changing properties, such as sediments in rivers, solidified lava or debris from volcano eruptions, sediments in oceans consisting of died organisms or fossils. By comparing various layers at different places, conclusion about age can be drawn in this discipline known as stratigraphy.

But as these stratigraphic analyses can only deliver a relative age, the geological sciences took a leap forward, and used the discovered radioactive decay as an opportunity to perform absolute age determination. Boltwood[1] was the first in 1907 to estimate the age of minerals based on the $U \rightarrow Pb$ decay. At this time, the existence of isotopes was not uncovered yet, and only the decay of a Ra intermediate in the decay chain was used to determine ages from 400 to 2200 Ma for a set of uranites and other minerals. This

contradicted the earlier approximation for the age of the Earth by Lord Kelvin of roughly 500 Ma[2] and intensified the research activity in this field.

1.1.1. Historical Development of U-Pb Age Determination

Soon after, the first ages of zircons were estimated to approximately 600 Ma. Lord Rayleigh used borax melts and measured the He, Th, and U content, effectively using the $^{238}U \rightarrow {}^{230}Th + 2\alpha + 2\beta^-$ decay part of the uranium series. He was already aware that, due to He loss, this age estimation represented the minimal age of the sample mineral. For the next three decades the U-Pb system was studied by simply measuring the U and Pb concentrations in the sample, as isotopes had not been discovered in the beginning. After the discovery of isotopes, reliable methods for quantitative determination had to be developed. A great step towards this goal was done by Nier in 1939, when he adopted a mass spectrometer for the determination of U isotope ratios.[3]

Zircon was already considered as a preferable mineral for age determination because of its inertness to chemical and physical damage. A wide range of methods was applied over the years, such as Pb-α counting,[4] isotope dilution-thermal ionisation mass spectrometry (ID-TIMS),[5] sensitive high mass-resolution ion microprobe (SHRIMP)[6] and secondary ion mass spectrometry (SIMS).[7] Although the precision and accuracy of ID-TIMS and SHRIMP are among the best, that could be achieved during the evolution in this field, limited sample throughput and high costs have been a limiting step for fast routine analysis. Based on a similar basic principle as SHRIMP, i.e. the erosion of the surface with a beam, LA was coupled with inductively coupled plasma mass spectrometry (ICPMS) by Gray in 1985.[8] This allowed for an additional boost in research activity in the field of U-Pb geochronology, which will be covered in Section 1.2.

1.1.2. La-Ba Age Determination

The decay systems originating from ^{138}La are mainly used for minerals with high content of rare earth elements (REEs), such as monazite $(La,Ce,Nd)[PO_4]$,[9] allanite $(Ca,La,Nd,Y)(Al_2Fe^{2+})[O|OH|SiO_4|Si_2O_7]$,[10] epidote $Ca_2(Fe^{3+},Al)Al_2[O|OH|SiO_4|Si_2O_7]$[10] or bastnaesite $(Ca,La,Nd,Y)[(F,OH)|CO_3]$.[11] These minerals can have La/Ba total concentration ratios from 1000:1 to 100:1, which should allow us to see the change in the $^{138}La/^{138}Ba$ ratio during analysis.

In all former studies, the minerals have been dissolved or digested, and the separation of La^{3+} and Ba^{2+} has been done with cation-exchange chromatography. In order to simplify the sample treatment and increase the sample throughput, Hirata proposed the idea of cool plasma condition in the inductively coupled plasma (ICP) for this type of analysis,[12] with liquid sample introduction systems and an ICP running as low as 500 W. It was shown that the $^{139}La^{16}O^+/^{139}La^+$ ratio increased up to 2 000 000 times, while the $^{138}Ba^{16}O^+/^{138}Ba^+$ ratio increased only up to 200 times. This is actually a selective oxidation of La versus Ba and leads to a chemical separation of both elements in the ICP.

Up to now, no LA-ICPMS studies have been reported on La-Ba age determination, mainly because of the fact that the separation of the two elements is not straightforward with laser-generated aerosol. Additionally, the cool plasma conditions do not immediately enable this separation, as the aerosol is generally dry and only contains limited amounts of O_2 gas. This is mostly seen as an advantage of LA-ICPMS experiments, as this results in reduced oxide rates (MO^+/M^+) compared to liquid introduction systems. Thus, isobaric interferences (signal of $^{m}M^{16}O^+$ on $^{m+16}M^+$), especially on the REEs, are greatly reduced and the sensitivity can be enhanced. Indeed, less ions form $^{m}M^{16}O^+$ and contribute to the $^{m}M^+$

instead. One way to model laser-generated aerosol is to use a desolvation system[13], which removes humidity from the gas stream introduced into to the ICPMS. These techniques will be further described in Section 3.6.

1.1.3. Other Decay Systems

Next to the U-Pb system, several other radio-active decay systems have been used for age determination of different samples; see Table 1.1.

The different systems have certain properties that make them more or less preferable in certain situations. Because of the long half-life, the U-Th-Pb system is suitable for old ages. In particular, if combined with zircon as sampled mineral, the high closure temperature of 900 °C allows the determination of very old samples, ultimately of minerals from the formation of the Earth 4.5 Ga ago.[14] The Rb-Sr and Sm-Nd systems are used for old samples but the closure temperatures are lower and, therefore, a geological event is more likely to reset the radiometric clock. The Lu-Hf system is often used on zircons for modelling the processes concerned with the Earth's mantle and crust.[15] Re-Os is used with metal and sulphide samples, such as meteorites, as the compatibility is higher in these phases.

Table 1.1.: Different decay systems used for age determination in geology after Elburg [16]

System	λ [a^{-1}]	Half-life [Ga]	Comment	Ref.
$^{39}Ar/^{40}Ar$, $^{40}K/^{40}Ar$	5.543×10^{-10}	1.25	potential Ar loss as tracer for closure temperature, not for ICPMS	[17]
$^{87}Rb/^{87}Sr$	1.42×10^{-11}	48	different compatibility of elements, low closure temperature	[18]
$^{138}La/^{138}Ba$	4.15×10^{-12}†	167	good for REE-rich minerals	[10]
$^{138}La/^{138}Ce$	2.77×10^{-12}†	250	good for REE-rich minerals	[10]
$^{147}Sm/^{143}Nd$	6.54×10^{-12}	106	similar to Rb/Sr	[19]
$^{176}Lu/^{176}Hf$	1.867×10^{-11}	37.1	used on metamorphic processes	[19]
$^{187}Re/^{187}Os$	1.667×10^{-11}	41.6	siderophile elements, age determination in metals and sulphides	[20]
$^{232}Th/^{208}Pb$	4.9475×10^{-11}	14.01	often found next to U-Pb system	[18]
$^{235}U/^{207}Pb$	9.8485×10^{-10}	0.704	combination with $^{238}U/^{206}Pb$ as a double system for better accuracy	[18]
$^{238}U/^{206}Pb$	1.55125×10^{-10}	4.468	precise dating possible for ages below 1000 Ma	[18]

† decay constant still uncertain, $\lambda_{EC,Ba} = 4.4 \cdot 10^{-12}$ and $\lambda_{\beta^-,Ce} = 2.25 \cdot 10^{-12}$ after [21]

1.2. Laser Ablation Inductively Coupled Plasma Mass Spectrometry of Zircons in Geochronology

LA-ICPMS has been used in a variety of geological applications due to the fact that it enables an analysis of minerals with minimal sample consumption rate, without digestion steps in sample preparation and eventually high spatial resolution.[22] Besides quantification of concentration in geological samples, the determination of isotope ratios for age determination is one of the main applications.[23] Two good reviews for best practices with broader geological applications can be found in short courses of the Mineralogical Association of Canada.[24,25]

1.2.1. Fractionation with ns- and fs-LA-ICPMS

When applying laser shots to a sample and measuring the resulting signal ratios of element pairs in the ICPMS, a gradual change can be found for certain elements. This process is known as (elemental) fractionation and has particular relevance to the quantification procedure in LA-ICPMS. If the fractionation between two elements is different between sample and reference material, a quantification will show a systematical error.

In an initial study, Fryer *et al.*[22] investigated the fractionation indices of 60 elements in NIST 610 relative to Ca and found the highest fractionation for elements such as Ag, Au, Bi, Cd, Pb, Sb, Te, Tl and Zn, which all have a low to medium melting point. Outridge *et al.*[26] studied the different contributions of ablative fractionation and transport fractionation with a near-infrared (NIR) ns-laser for NIST 610 and a copper standard, with the result, that the transport fractionation for most elements is higher than the ablative fractionation in NIST 610. This effect is increased for less-refractory and volatile elements, which indicates a different partitioning in vapour and particulate phase during the ablation event. With the copper standard, a reverse effect is seen: the ablative fractionation is the most relevant source of fractionation, indicating that for conductive samples phase transformation and zone refinement at the ablation spot is responsible for the fractionation.

Under such conditions a quantification of conductive samples with a non matrix-matched reference material will not lead to acceptable results.

Fractionation can be found at different points over the whole measurement system, starting at the ablation site, following the transport path along tubings, entering the torch and plasma, passing through the interface and finally undergo fractionation in the ion optics of the mass spectrometry (MS) system. For the parts before the interface the nature and

properties of the laser-generated aerosol seems to be most influential to the fractionation processes.

Kuhn *et al.* have shown, that the particle size of the aerosol plays an important role for fractionation, as particles with diameters above 150 nm might not be completely vaporised, atomised and ionised in the ICP for a wider range of plasma parameters.[27] The 266 nm Nd:YAG laser used in the study produced larger particles during the first 100 laser shots, already using helium as carrier gas. The use of He instead of Ar as carrier gas reduces the general partical size and in combination with a 193 nm laser shifts 90 % of the ablated volume in the range of 100-200 nm particles.[28] Additionally, more smaller particles are produced with this setup, in contrast to setups with lasers emitting larger wavelength photons, or setups which use Ne or Ar as carrier gas. This has the effect of a more complete ionisation in the ICP and results in generally higher signals for NIST 600 series glasses and synthetic quartz glass. Further studies showed, that in general the carrier gas composition[28–30] can change the particle size distribution (PSD) as well as various ablation parameters such as the aspect ratio of the ablation spot,[31,32] the wavelength of the laser used,[33,34] the fluence on the sample surface[35,36] and the pulse duration of the laser,[37,38] which is particular important for conductive samples.

As result of those studies, the current model of the laser-matter-interaction and the generation of particles can be summarised as follows:[39] The photons impacts on the surface and and transfer their energy by coupling with electrons in the time range of fs. Within ps the energy is further transferred to the lattice by electron-phonon coupling and a plasma is created above the surface. From this point on, if more energy is delivered into the system by ns laser pulse, melting and vaporisation of the sample occurs and the plasma absorbs already most of the energy in this time range (plasma shielding). After the laser

pulse stops, the plasma collapses and particles can be created either via nucleation and condensation[34,38] or agglomeration and coagulation.

To summarise: Elemental fractionation is fundamentally connected to the particles generated during the laser ablation, either because particle composition differs from bulk composition — e.g. melting and solidification of elements with different vaporisation temperatures — or because of the generation of particles that are too large to be completely ionised in the ICP.

1.2.2. U-Pb Fractionation During Analysis of Minerals

U-Pb age determination can in principal be applied to all minerals which have enough U incorporated during crystallisation and are old enough, that a measurable amount of Pb could have been generated. In addition, for a reasonable interpretation of the age it is required that the radiometric system is closed, i.e. the diffusion of the respective elements is low enough that the daughter isotope is not diffusing out of the lattice structure and a reset of the radiometric clock occurs. Silicates and phosphates have the advantage for generally showing a higher closing temperature for U-Pb. The determined age of minerals with different closing temperatures of one rock can be used to get some insights into the temporal temperature development over the lifetime of the rock. This could be also coupled with other radiometric systems.

Typical minerals for U-Pb age determination are zircon (which will be covered in Section 1.2.3), monazite, apatite,[40–42] titanite (also known as sphene),[43–47] allanite,[48] columbite-tantalite[49] and rutile.[50] Problematic with minerals other than zircon or monazite are the typical high values of common, i.e. non-radiogenic Pb in the mineral. Common Pb introduces an intercept in the age equation (3.4) as there is a amount of initial daughter

isotope present during crystallisation. This can be corrected by measuring a non-radiogenic isotope of Pb (in this case ^{204}Pb) and subtract intensity from the other isotopes according to the natural abundance of Pb-isotopes. With SIMS, this can be done easily, there are normally no significant isobaric interferences on 204, although higher amounts of tungsten can lead to the formation of $^{186}W^{18}O$.[6] In contrast, for LA-ICPMS analysis Hg present in the gas or sample will show as an isobaric interference on mass 204. A correction method could either be the measurement of other Hg isotopes (e.g. 202) and subtract the values accordingly or to use mathematical corrections based on the measured Pb/U and Pb/Th ratios.[51]

U-Pb geochronology is also performed on minerals, which are not considered accessory minerals such as uranitite and perovskite. Uranitite was first analysed with LA-ICPMS by Chipley *et al.* using 91500 zircon as external standard.[52] Further research showed that for uranitites even with fs-LA a matrix-matched standard is beneficial as otherwise a deviation up to 17 % was reported.[53] Perovskite can be present as primary magmatic mineral in rocks with a high U and Th content and, therefore, is also candidate for geochronology studies. The common Pb present in the mineral and the need of reference materials exacerbate the analysis with LA-ICPMS, nevertheless, a weighted mean $^{206}Pb/^{238}U$ age of 131 ± 7 Ma was obtained, which equals to a precision of 5 %.

Apart from the potentially higher common Pb in the mineral a critical requirement for LA-ICPMS in the availability of suitable standard to get accurate result from the analysis and to ensure comparability for between different laboratories. In general, LA-ICPMS analyses require a matrix-matched standard, although with some applications the use of a fs-laser system allows to use NIST 610 as only non-matrix-matched reference material.[54,55] For zircon, a variety of around ten larger, natural zircon crystals have been prepared and

distributed by the geochronology community in the recent years (see Table 3.1). This also allows to adapt to the respective age, or U and Pb concentration in the sample. This adaptation is actually necessary, as fractionation (see Section 1.2.4) varies between different zircons with respect to age, α-damage and other parameters.[56] The use of NIST 610 as non-matrix-matched reference material is not advised as accurate results are only produced when specific aspect ratios of the ablation crater are used.[57,58] Following these reports, it has to bee assumed, that also for other minerals different fractionation effects are possible and further efforts in the field of reference materials is required. In reality, the range of matrix-matched standards available is typically smaller for other minerals than for zircon.

1.2.3. Zircon

The analysis of the U-Pb decay system in zircons ($ZrSiO_4$, tetragonal (t) form) is widely used. The main advantage is that zircon incorporates U^{4+} as substitute for Zr^{4+} or Si^{4+} during crystallisation, but excludes Pb^{2+}. Therefore, it contains little to no initial lead.[59] In this case, all Pb measured in a zircon can be considered radiogenic, which allows the determination of concordant ages from a single measurement of $^{206}Pb/^{238}U$ and $^{206}Pb/^{207}Pb$. The concordance of ages can be disturbed, if crystals undergo metamorphosis during which Pb is preferentially lost by diffusion at elevated temperatures.[60] An enhanced Pb diffusion in zircon can be observed in 100 µm crystals at temperatures over 900 °C .[61] Due to the chemical and physical stability, the ages obtained from zircons is usually the oldest in the rock. It is also possible, that another layer is formed during a later crystallisation events, which produced zoned zircon grains with different ages in the various layers. Special abrasion techniques for layer-by-layer analysis[5] and spatially resolving methods such as SHRIMP and LA-ICPMS have to be employed to elucidate the entire formation history for

one grain.

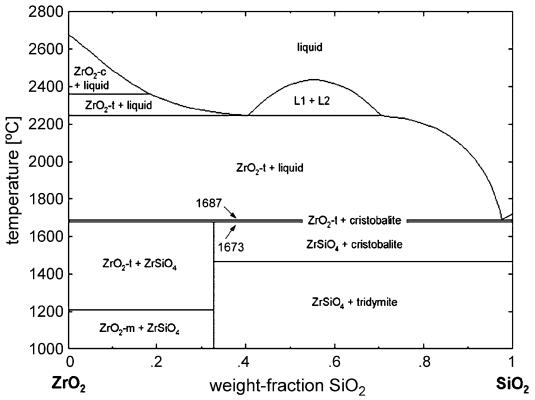

Figure 1.1.: Phase diagram of ZrO_2-SiO_2 after Kaiser *et al.*[62]

Possible phase transition can be seen in the phase diagram (see Figure 1.1). $ZrSiO_4$ dissociates at 1673 °C in t-ZrO_2 and SiO_2, and at temperatures higher than 1687 °C the only solid phase remaining is t-ZrO_2. As a plasma generated by LA can have temperatures in the range of 5 000 to 10 000 K, phase transitions are an issue during melting and re-solidification.[58]

1.2.4. U-Pb Fractionation at Zircon Analysis

In the early studies of LA-ICPMS for U-Pb age determination many challenges have been identified:[63] e.g. unstable signals for spot ablation, prominent down-hole fractionation, limited sensitivity for low Pb concentration in young or U poor zircons, long washout of generated aerosol, slow signal processing and, therefore, limited amount of sample throughput. Most of these points have been addressed and partially solved by the improvements of state of the art LA units and ICPMS systems: Laser systems with nanosecond pulses in the UV range allow for a more reproducible material removal from the ablation spot, reducing down-hole fractionation.[64,65] Together with the use of helium as a carrier gas, they yield

smaller particles sizes and provide narrower PSD.[28] For fs-lasers, a reduction of down-hole fractionation in the Pb/U ratio has been reported in the first part of the ablation process of a NIR-fs-laser,[66] but then a wider range of particle sizes and subsequent phase separation in these particles have been reported for both IR- and UV-fs-laser.[67] The development of fast washout ablation cells[68,69] allow for better separation of aerosols from different ablation spots, yield a higher signal per time unit and, finally, make it possible to acquire a data point from a single zircon grain in 6 to 14 s.[70] As the handling of laser systems became easier and the instruments more affordable, it became feasible to make an inter-laboratory round robin test to asses the quality of results from different laboratories analysing a synthetic set of detrital zircons.[71] The accuracy ranged from 3.5 to 8 % in terms of ages for the different zircons. Although, there are still more difficulties with low concentrations of Pb, the main source of deviation was found to be in data reduction methods and applied uncertainty propagation. An overall inter-laboratory deviation of 2 % in the ages has been reported.[71]

Despite this progress, the problem of down-hole fractionation is still present, especially for analyses that last longer than a few seconds. A range of mathematical approximation and correction procedures have been applied to the raw signal to reduce the uncertainty and correct for differences even between matrix-matched reference materials, i.e. zircons. A linear model of the fractionation has been used to correct the fractionation over the whole ablation time.[72] The intercept method assumes that the fractionation is least pronounced at the beginning of the ablation and, therefore, the intercept of a linear fit to this point is taken as value of $^{206}Pb/^{238}U$ for further calculations.[30] Fisher *et al.* compared the intercept method with the ratio of means (ROM) and mean of ratios (MOR) for a range of samples, and found higher relative standard deviations of isotope ratios and higher deviations from the accepted ages for the intercept method, recommending ROM and MOR for higher

precision.[73] Recently, the idea of using a smooth spline to fit the time trace data to retain more data points per measurement has been introduced.[74] Although the correction with mathematical methods is currently a valid way to cope with the fractionation problem, more knowledge about the underlying processes helps to understand the reason for fractionation and may offer solutions for better correction.

Košler *et al.*[58] showed in a scanning electron microscopy (SEM) study on ablation pits of zircons acquired with a Nd:YAG 266 nm laser and the deposited debris, that during the ablation process a phase separation occurs into SiO_2 and ZrO_2, which then also results in fractionation of Pb and U in these phases. In those experiments, a 266 nm laser was shown to generate larger particles during the first 250 laser pulses (< 2.5 µm) reducing the size afterwards(< 0.3 µm). For 91500, the small spherical particles, are mostly pure baddeleyite (crystalline ZrO_2) with amorphous Si attached to the surface, which is a different phase than the bulk zircon. Additionally, the $^{206}Pb/^{238}U$ ratio in the particle debris around the ablation crater was found to be decreasing from up to 0.35 at the crater rim to about 0.15 roughly 900 µm away from the rim. This phase transition was also observed inside the crater, as the inner crater wall showed a baddeleyite phase in combination with amorphous SiO_2. It was proposed that the melting during the ablation process leads to a phase separation and with it a retention of U in the newly formed baddeleyite phase.

In a follow up to this initial study, a 193 nm ArF excimer laser was used to look more closely at the effect of phase separation at the crater walls.[75] Under these conditions, depositions of partially crystalline ZrO_2, amorphous SiO_2 and small amounts of $ZrSiO_4$ have been found, which indicate a phase separation within the ablation crater. The study also investigated this phenomenon and the down-hole fractionation with respect to the dependence on the addition of O_2 to the ablation chamber. An increase in the fractionation

of $^{29}Si/^{96}Zr$ has been reported with increasing O_2, while the $^{206}Pb/^{238}U$ did not change significantly. The setup of this study directly introduced the He-O_2-particle mixture into the ICP; thus, no differentiation between the effect of O_2 during ablation and within the ICP could be made.

Allen and Campbell investigated the elemental fractionation and the resulting age offset between LA-ICPMS and ID-TIMS from a different perspective.[56] They reported a correlation between the radiogenic Pb and the age difference between these two methods for a range of zircons. Another correlation between radiogenic Pb and down-hole fractionation was found. To overcome this effects, the authors applied an annealing procedure to repair the damages in the crystal lattice produced by α-radiation from U decay, in which they kept the zircons for 48 h at 850 °C under air. As a result, the $^{206}Pb/^{238}U$ offset was reduced to 0.52 % or lower, which is equivalent to 2 s.e. uncertainty of the Temora 3 reference. Additionally, the systematic differences in down-hole fractionation was not visible anymore.

2. Motivation

Driven by the fact that U-Pb radiometric dating by LA-ICPMS on zircons is a widely used method in geochronology, and that the down-hole fractionation during the ablation process causes an uncertainty in the determination of the supposedly correct age of a sample, a deeper understanding on the process of down-hole fractionation could help to overcome this uncertainty. As the gas composition, under which the ablation takes place, is an important factor on the ablation process, variation of gas mixtures could lead to better results. To study the effects of the ablation gas mixture on the resulting signal in the ICPMS, a separation of the conditions on the ablation spot and in the ICP is necessary.

It has been previously reported to mix additional gases before and after the ablation chamber to the carrier gas of the system with the aim to study the effect on the laser ablation. The major drawback in those setups is the presence of the added gas in the ICP in both strategies. Only with the availability of the GED it became possible to add gas before the ablation chamber and then analyse the resulting aerosol without affecting the ICP by the gas addition.

In the first part of this work, the described setup was applied to zircon reference standards with the aim to separate the laser effect and the plasma effect on fractionation and evaluate whether there are optimal conditions for U-Pb age determination.

In the second part, the addition of O_2 to laser-generated aerosol was used to facilitate an online separation of ^{138}La from ^{138}Ba on m/z 138 for ICPMS with sample introduction of dry aerosols. This would allow researchers to reduce the sample treatment before analysis and could enable a broader use of the $^{138}La \rightarrow {}^{138}Ba$ decay in geochronology.

3. Methods and Experimental

3.1. Geochronology

Geochronology is mainly focused on radioactive decay systems since the discovery of isotopes and their utilisation for analytical systems.

The principles of this method can be found in textbooks such as ref. [21]. The most important equations and relations will be discussed in this section.

Radioactive decay is the transformation of a parent isotope P into a daughter isotope D under the emission of radiation. In the classical sense this would be either α ($^4He^{2+}$), β^- (electron) or γ (a highly energetic photon) radiation. In addition to these, further decay modes have been discovered, of which β^+ (positron) emission and electron capture play a more important role for geochronological systems.

$$P \xrightarrow{\lambda} D \quad (+\alpha, \beta^-, \beta^+ \ldots) \tag{3.1}$$

Equation (3.1) describes a general decay with a decay constant λ. The amount of isotopes in a closed system at a time t can be expressed as:

$$N_P(t) = N_P(0)\, e^{-\lambda t} \tag{3.2}$$

$$N_D(t) = N_D(0) + N_P(t)(e^{-\lambda t} - 1) \tag{3.3}$$

with $N_P(0)$ and $N_D(0)$ denoting the initial amount of parent and daughter isotope at the closing time of the system, and $N_P(t)$ and $N_D(t)$ the amounts of at time t after closing. From Equation (3.3) it is easy to derive the age equation:

$$t = \frac{1}{\lambda} \ln \left\{ \left[\frac{N_D(t) - N_D(0)}{N_P(t)} \right] + 1 \right\} \tag{3.4}$$

If the amount of the daughter isotope at the beginning is zero or negligible, then Equation (3.4) can be simplified to

$$t = \frac{1}{\lambda} \ln \left\{ \left[\frac{N_D(t)}{N_P(t)} \right] + 1 \right\}. \tag{3.5}$$

This is, for example, true for the Rb-Sr system in minerals with low Sr concentration and also for the U-Pb system in most zircons:

$$t = \frac{1}{\lambda_{238}} \ln \left\{ \left[\frac{^{206}\mathrm{Pb}(t)}{^{238}\mathrm{U}(t)} \right] + 1 \right\} \tag{3.6}$$

However, this is not the case for the La-Ba system, as there is usually a certain amount of Ba in the respective minerals. For U-Pb decay systems, there is the situation of two combined decay chain systems: $^{238}U \rightarrow {}^{206}Pb$ and $^{235}U \rightarrow {}^{207}Pb$. This allows researches to combine both systems for age determination. If both ages are very similar, they are called concordant. An easy visual representation can be realised with a concordia plot (see Figure 3.1a):

$$t = \frac{1}{\lambda_{235}} \ln\left\{\left[\frac{^{207}Pb(t)}{^{235}U(t)}\right] + 1\right\} \tag{3.7}$$

together with Equation (3.6) this allows us to calculate a curve in a $^{206}Pb/^{238}U$ vs $^{207}Pb/^{235}U$ diagram.

$$\frac{1}{\lambda_{238}} \ln\left\{\left[\frac{^{206}Pb(t)}{^{238}U(t)}\right] + 1\right\} = \frac{1}{\lambda_{235}} \ln\left\{\left[\frac{^{207}Pb(t)}{^{235}U(t)}\right] + 1\right\}. \tag{3.8}$$

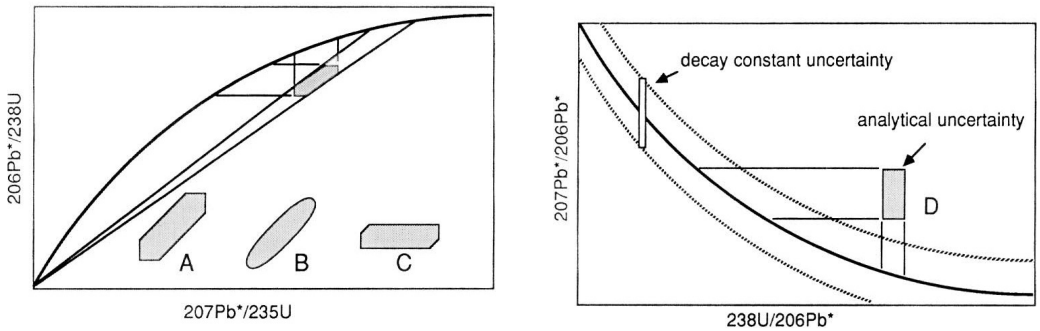

Figure 3.1.: Schematics of a conventional (a)[60] and a Tera-Wasserburg concordia (b)[76]

For the determination of the age out of the $^{206}Pb/^{207}Pb$ ratio, a two-equation system is

used:

$$^{206}\mathrm{Pb}(t) = {}^{238}\mathrm{U}(t)\left(\mathrm{e}^{\lambda_{238}t} - 1\right) \tag{3.9}$$

$$^{207}\mathrm{Pb}(t) = {}^{235}\mathrm{U}(t)\left(\mathrm{e}^{\lambda_{235}t} - 1\right) \tag{3.10}$$

The ratio of these equations in combination with the U isotope ratio of $^{238}\mathrm{U}/^{235}\mathrm{U} = 137.8$ allows for an implicit calculation of the age from the $^{206}\mathrm{Pb}/^{207}\mathrm{Pb}$ ratio:

$$\left(\frac{^{206}\mathrm{Pb}}{^{207}\mathrm{Pb}}\right)_t = \frac{1}{137.8}\left(\frac{\mathrm{e}^{\lambda_{238}t} - 1}{\mathrm{e}^{\lambda_{235}t} - 1}\right) \tag{3.11}$$

This equation also allows the calculation of the $^{206}\mathrm{Pb}/^{207}\mathrm{Pb}$ ratio for a given age, which allows for an alternative concordia plot called Tera-Wasserburg plot[76] (named after the inventors, see Figure 3.1b). Both concordia diagrams can be used to estimate how much Pb was lost or U was gained after the closing of the mineral, and at which points in time.[21,77] Depending on the estimated age of the sample, $^{206}\mathrm{Pb}/^{238}\mathrm{U}$ is preferred for samples younger than 1.2 Ga, as the precision is higher up to this age than for $^{206}\mathrm{Pb}/^{207}\mathrm{Pb}$ ratio, which is more favourable for samples older then 1.2 Ga (see Figure 3.2).

3.1.1. External Calibration

As mentioned in Section 1.2.4, the external calibration approach for U-Pb age determination on zircons has reached its limits. As the differences in age, U content, alpha damage and absorptivity can influence the ablation behaviour and laser-induced fractionation, it seems that until now no single zircon could be used as universal reference material to determine more accurate and precise ages. A set of natural zircons used in LA-ICPMS is compiled in

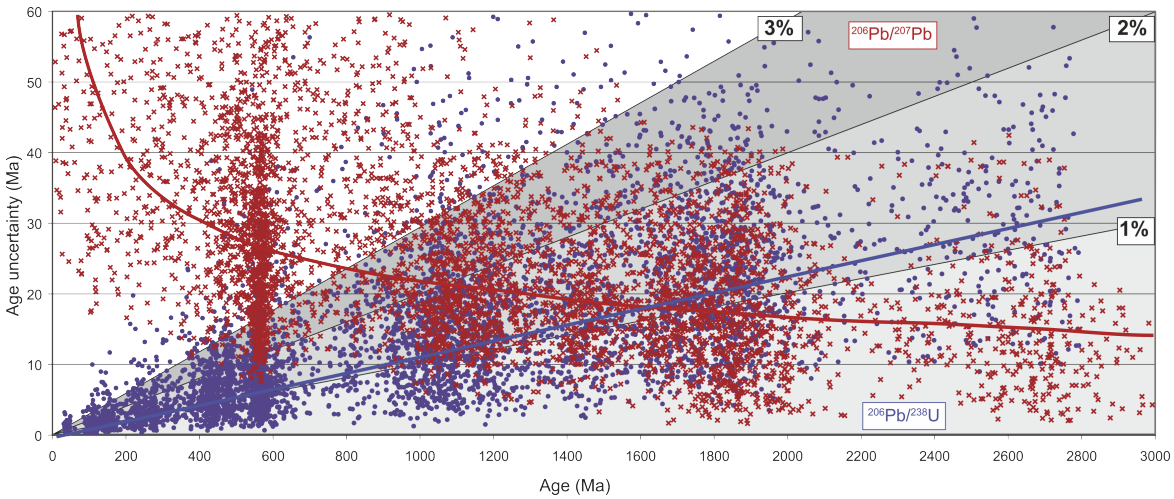

Figure 3.2.: Measurement errors (1σ) of over 5200 sample ages indicating 1.2 Ga as a limit to switch the preferred type. Reproduced from ref. [78]

Table 3.1.

Nevertheless, the following procedure is still applied when determining $^{206}Pb/^{238}U$-ages. For each sample, at least four spots are measured. A series typically consist of 1. the reference material, 2. if needed a secondary standard, 3. the samples and 4. again the reference material at the end of an ablation series. If even higher precision is required, a standard-sample-bracketing can be applied.[73] The correction factor k for $^{206}Pb/^{238}U$ ratio can be derived from Equation (3.6) and the known age of the standard t_{std}:

$$k = \frac{e^{\lambda_{238} t_{std}} - 1}{\left(\frac{^{206}Pb}{^{238}U}\right)_{std,meas}} \tag{3.12}$$

Table 3.1.: Overview of natural zircon reference materials used for LA-ICPMS , after Sláma *et al.*,[79] modified with GeoRem values[80]

Reference Material	Age (Ma)	U (ppm)	Pb (ppm)	Hf (ppm)	Grain size	Comments
QCNG[81]	1850	35-1151		10600 ± 340	0.05-0.3 mm	Inhomogeneous Pb/U ratio, probably Pb loss
AS3[82]	1099	113-626	22-135		Up to 0.5 mm	Probably Pb loss
91500[83]	1065	71-86	13-16	3488-7353	Variable size, 238 g	Almost exhausted supply
Mud tank[84]	732	6.1-36.5	0.73-4.39		mm-cm	
GJ-1[85]	609	212-422	19.3-37.4		ca 1 cm	Inhomogeneous Pb/U ratio, discordant age
SL 13[15]	572	149	15			Inhomogeneous Pb/U ratio, probably Pb loss
Z6266(Br266)[86]	559	871 - 958	76.5 - 84.2		2-6 mm	
R33[87]	419	61 -398				probably Pb loss
Temora 1[88]	417	195	14.3	7801	Up to 0.6 mm	
Temora 2[87]	417	45 - 755		8479	0.05 - 0.3 mm	Different host rock than Temora 1, but same age
Plešovice[79]	337.1	465 - 3084	21 - 158	8980 - 14431	1 - 6 mm	Wide range of results from pristine and actinide zircon domains

The correction factor for a certain sample is either the average of multiple standard measurements or the interpolation for this sample in between standard measurements via linear regression. One of those ways yields a k' for correction of the sample:

$$\left(\frac{^{206}\mathrm{Pb}}{^{238}\mathrm{U}}\right)_{sam,corr} = k' \cdot \left(\frac{^{206}\mathrm{Pb}}{^{238}\mathrm{U}}\right)_{sam,meas} \tag{3.13}$$

From this point, the final age of one measurement can be calculated according to Equation (3.6):

$$t = \frac{1}{\lambda_{238}} \ln\left\{\left(\frac{^{206}\mathrm{Pb}}{^{238}\mathrm{U}}\right)_{sam,corr} + 1\right\} \tag{3.14}$$

This method has also been applied for the evaluation of the Plešovice ages of Figures 4.5 and 4.12.

3.1.2. La-Ba Calculations

For the evaluation of the ^{138}La decay, the calculations differ from the simple decay systems, as the parent isotope decays into two daughter isotopes with different decay rates:

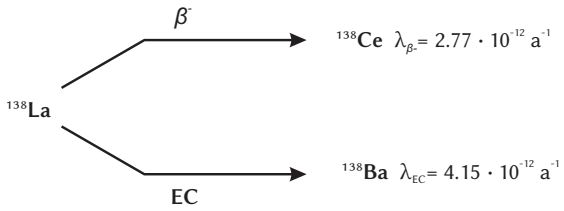

(3.15)

The modified equation for the relevant daughter isotope ^{138}Ba is the following

$$^{138}\mathrm{Ba}(t) = {}^{138}\mathrm{Ba}(0) + \frac{\lambda_{\mathrm{EC}}}{\lambda_{\mathrm{EC}} + \lambda_{\beta^-}} \cdot {}^{138}\mathrm{La}(t) \cdot \left(\mathrm{e}^{(\lambda_{\mathrm{EC}}+\lambda_{\beta^-})t} - 1\right) \tag{3.16}$$

The decay constants can be combined according to $\lambda_{\mathrm{La}} = \lambda_{\mathrm{EC}} + \lambda_{\beta^-} = 6.92 \cdot 10^{-12}\mathrm{a}^{-1}$ and the whole equation can be divided by the stable reference isotope ^{137}Ba:

$$\left(\frac{^{138}\mathrm{Ba}}{^{137}\mathrm{Ba}}\right)_t = \left(\frac{^{138}\mathrm{Ba}}{^{137}\mathrm{Ba}}\right)_{t=0} + \frac{\lambda_{\mathrm{EC}}}{\lambda_{\mathrm{La}}} \cdot \left(\frac{^{138}\mathrm{La}}{^{137}\mathrm{Ba}}\right)_t \cdot \left(\mathrm{e}^{\lambda_{\mathrm{La}}t} - 1\right) \tag{3.17}$$

As the initial isotope ratio $^{138}\mathrm{Ba}/^{137}\mathrm{Ba} = 6.39028$ can be assumed as constant,[9] it is possible to construct an isochron from multiple minerals or just a single point isochron as follows:

$$t = \frac{1}{\lambda_{\mathrm{La}}} \ln\left[\underbrace{\frac{\left(\frac{^{138}\mathrm{Ba}}{^{137}\mathrm{Ba}}\right)_t - \left(\frac{^{138}\mathrm{Ba}}{^{137}\mathrm{Ba}}\right)_{t=0}}{\left(\frac{^{138}\mathrm{La}}{^{137}\mathrm{Ba}}\right)_t}}_{m} \cdot \frac{\lambda_{\mathrm{La}}}{\lambda_{\mathrm{EC}}} + 1\right] \tag{3.18}$$

with m being the resulting slope in the $^{138}\mathrm{Ba}/^{137}\mathrm{Ba}$ vs. $^{138}\mathrm{La}/^{137}\mathrm{Ba}$ plot (cf. Figure 3.3).

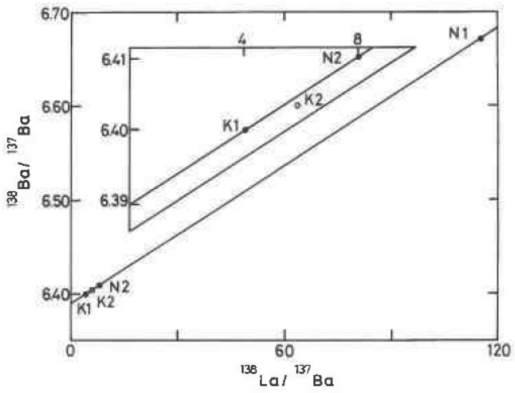

Figure 3.3.: An example for an La-Ba isochron reproduced from [11]

3.2. Inductively Coupled Plasma Mass Spectrometry

The ICP was first introduced as an excitation source for analytes in spectroscopic methods (inductively coupled plasma optical emission spectroscopy (ICP-OES)), and later was adopted as an ion source for mass spectrometric experiments of element ions by Houk *et al.* in 1980.[89] The development of the basic concepts have been described in several reliable textbooks,[90,91] which have been the base of the following sections.

3.2.1. Inductively Coupled Plasma for Ionisation

An inductively coupled plasma (ICP) is used as an ion source in ICPMS to generate gas-phase ions which can be separated by a mass analyzer and detected in the mass spectrometer. The basic principle of a torch to sustain an Ar plasma was developed by Reed[92] and was

later refined to a three flow torch for analytical purposes.[93,94]

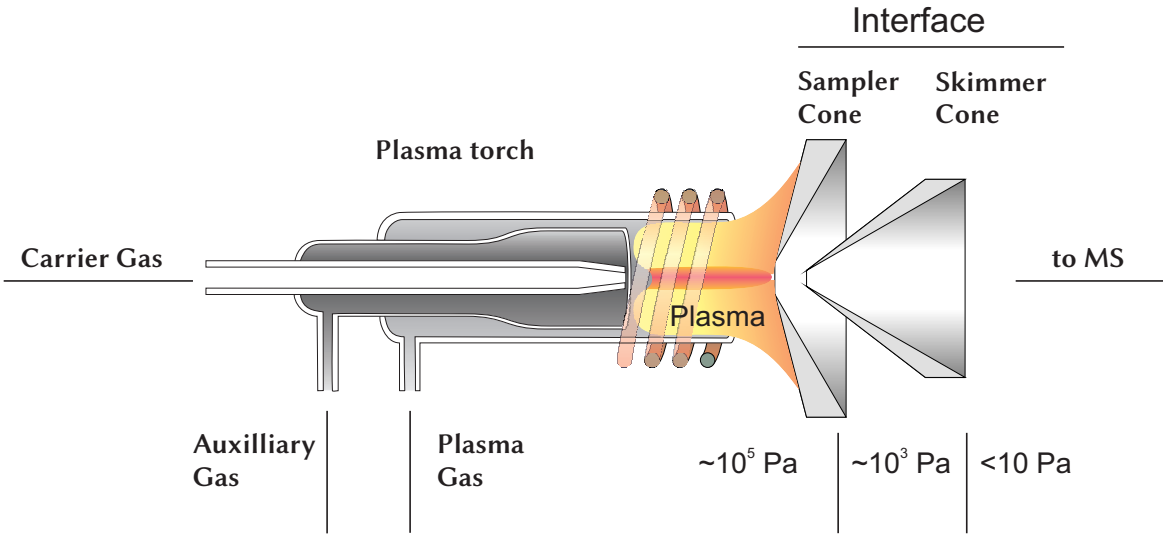

Figure 3.4.: Scheme and components of an ICP*

A schematic of a typical ICP torch is shown in Figure 3.4. For solution nebulisation (SN), all gas flows are typically Ar, but for LA the carrier gas can be a mixture of He and Ar due to a smaller resulting particle size distribution when ablation is performed under He.[29] A small size of particles for LA and droplets for SN is required for complete vaporisation, atomisation and ionisation in the plasma. Droplets exiting a spray chamber larger than 20 µm are only incompletely desolvated and ionised in the plasma[95] incomplete vaporisation was also reported for laser-generated aerosol larger than 1 µm.[96,97] A complete vaporisation and ionisation is very important, as otherwise elemental fractionation occurs.[63] More refractory and less volatile elements will stay solid and not contribute to the final signal.

* Modified after a drawing by Bodo Hattendorf

3.2.2. Quadrupole Mass Spectrometry

A quadrupole mass analyzer consists basically of four electrodes either in rod or hyperbolic shape (see Figure 3.5). An oscillating field is applied to the opposite rods and additionally a direct current (DC) offset. Ramping up the radiofrequency (RF) in a constant ratio with the DC offset produces stable trajectories through the quadrupole for a different mass to charge ratio (m/z).

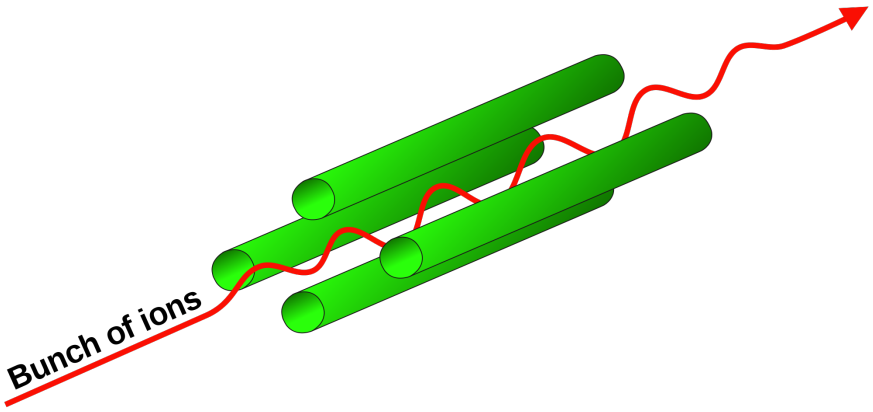

Figure 3.5.: Scheme of quadrupole mass analyzer with stable ion path†

This configuration results in a mass band filter that allows the separation of ions with a resolution up to 300 according to the following equation (3.19)

$$R = \frac{M}{\Delta M} \tag{3.19}$$

with R being the resolution, M the mass, or better m/z, and ΔM is the separation of peaks at 10 % height. The resolution of a quadrupole is sufficient for atomic mass spectrometry,

† by Angelus, CC-BY-SA 3.0, https://commons.wikimedia.org/wiki/File:Quadrupole_mass_analyzer.svg

but generally not to resolve between molecular ions and atomic ions at the same nominal m/z. An advantage of quadrupole system is the relatively fast switching time compared to higher resolving sector field mass analyzer, which is useful to scan the whole mass range of 250 amu with a scan speed up to 3000 amu/s for introduction systems as laser ablation, chromatographic systems or electrothermal vaporization (ETV).

As a quadrupole is an inherent serial mass analyzer, only a serial detection is possible. A secondary electron multiplier (SEM) is usually used as detector, often with the ability to work in counting or pulse mode, or in analog mode. Counting mode allows the detection of single ion impact events up to a rate of approximately $2{\cdot}10^6$ cps, analog mode for more signal up to $1{\cdot}10^9$ cps, effectively enabling a dynamic range of 9 orders of magnitude.

The quadrupole ICPMS used in this work was an Agilent 7500cs (Agilent Technologies, Waldbronn, Germany).

3.2.3. Sector Field Multicollector Mass Spectrometry

Because the quadrupole is limited to serial detection of ions, other mass analyzers allowing simultaneous detection have been developed. In general, sector field geometries have been developed, which consist either of an electrostatic sector producing a **E** field, which enables an separation on basis of the kinetic energies of the transmitted ion, or of a magnetic sector producing a **B** field, which separates according to the m/z of the ion, or both of them combined. Mattauch and Herzog developed a configuration with first a $\frac{\pi}{\sqrt{2}}$ angle electrostatic followed by a $\frac{\pi}{2}$ angle magnetic sector that allows a focusing of all ions simultaneously on the image plane and offers the ability to detect all ions in a certain range.[98] This approach has been developed recently into an commercial ICPMS by Spectro Analytical Instruments GmbH (Kleve, Germany), but it still has some

drawbacks. Indeed the problem of simultaneous detection and data read-out in this extent is not solved sufficiently for all analytical purposes yet.[99]

A different geometry of the two sectors has been developed by Nier and Johnson. Here, after an entrance slit a 90° angled electrostatic sector is placed. The ion beam enters a drift region before it is guided into a 60° angled magnetic sector. Finally an exit slit is inserted in the beam path in front of the detector.[100] With this configuration and different slit widths, a resolution up to $R = M/\Delta M = 10\ 000$ is possible in commercial instruments. Instruments with first the magnetic and then the electrostatic sector, representing the so called reverse Nier-Johnson geometry, have been constructed as well.

When the exit slit is left out in the Nier-Johnson geometry, a multiple detector array can be placed after the magnetic sector and different m/z signal from a certain adjacent range can be measured simultaneously. This is the principle of the NuPlasma (Nu Instruments Ltd., Wexham, UK) used in this work (see Figure 3.6).

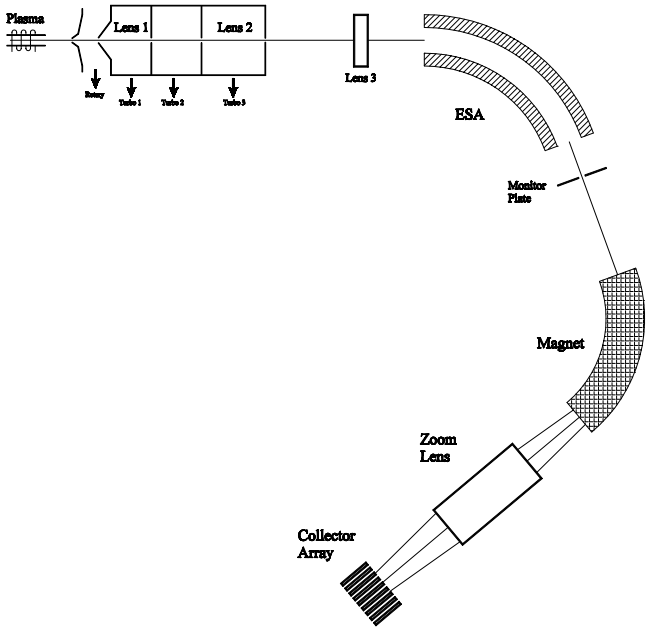

Figure 3.6.: Instrument schematic of the NuPlasma, taken from the instrument manual.

With additional beam focusing optics, also called zoom lenses, an optimal beam shape in different m/z ranges can be tuned to hit multiple Faraday- or SEM-detectors. In contrast to the Mattauch-Herzog geometry, more physical space is available for detectors and electronics, so that these kind of systems have been successfully operated for many years.

The main advantage of simultaneous detection is found in isotope ratio experiments, where very high precision is needed. As the ions of different m/z have all been excited in the ICP at the same time, the influence of plasma fluctuation is greatly reduced. To further improve the precision and accuracy, mass bias corrections and standard-sample-bracketing analysis protocols have been established.

3.3. ns- and fs-Laser Ablation Inductively Coupled Plasma Mass Spectrometry

Although solution nebulisation (SN) enables the analysis of a wide range of samples in combination with ICPMS with high sensitivity and low limits of detection (LODs), the need for sample preparation, wet bench chemistry and the inherent bad spatial resolution on the sample surface are considerable limitations. After LA was introduced in combination with ICPMS, a possibility was created to allow for high sensitivity, high sample throughput and spatially resolved analysis of solid samples. A common setup is visualised in Figure 3.7.

The setup used in this work included a GED (see Section 3.4) between the ablation cell and interface.

A set of parameters at the laser system is responsible for the ablation process and the impact on elemental fractionation and PSD of the produced particle: wavelength,[33,36,102] fluence on the sample surface,[103] focus of the laser onto the surface,[102] repetition rate of

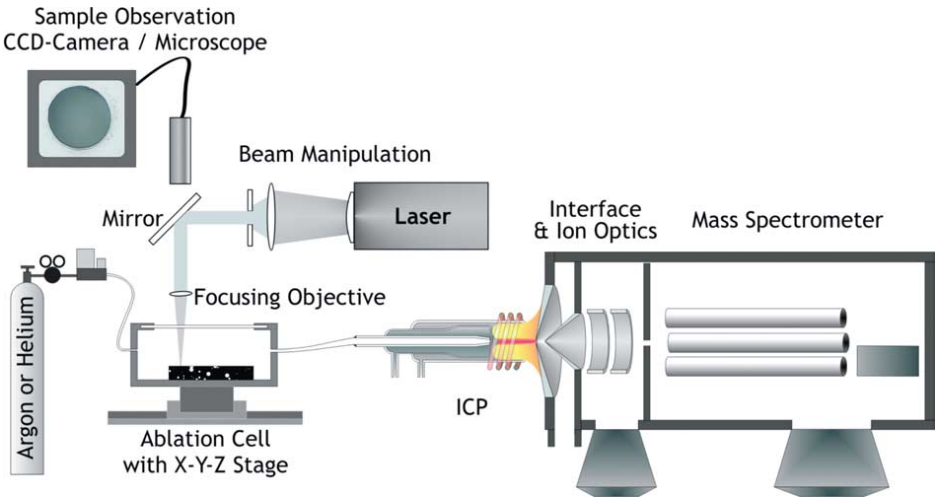

Figure 3.7.: Schematic of a typical LA-ICPMS setup, reproduced from [101]

the laser pulses,[104,105] pulse width,[106] beam profile[31,107] and gas environment.[29,31]

Of these parameters, the gas environment is further discussed in Section 3.5.2; wavelength and pulse width dependency will be discussed here briefly.

A broader range of suitable and stable lasers have been employed for ICPMS. Nd:YAG-lasers are solid state lasers that operate at a fundamental wavelength of 1064 nm but can be modified in their wavelengths by frequency doubling (532 nm),[102] quadrupling (266 nm)[102,108] or quintupling (213 nm).[33] Nd:YAG systems typically have a pulse width of 5 ns, a flat top beam profile for homogeneous ablation over the crater surface, are easy to handle and require little maintenance. Apart from solid state lasers, one gas laser, the ArF excimer laser system with a fundamental wavelength of 193 nm, has become popular. One initial drawback was the Gaussian beam profile, which was later solved by beam homogenising with a stack of optical lenses.[103] The pulse width is around 20 ns and the repetition rate can reach up to 100 Hz.

With laser systems, the principle ablation process is the coupling of photons to electrons,

which then scatter on phonons. In a follow up, when thermal relaxation is allowed, melting of the solid material occurs.[109] For pulse duration < 10 ps, the ablation does not involve melting but is rather a phase explosion (see Figure 3.8).[110] This enables a sampling that is near to the stoichiometric composition of the sample, especially for conducting material as metals or alloys.

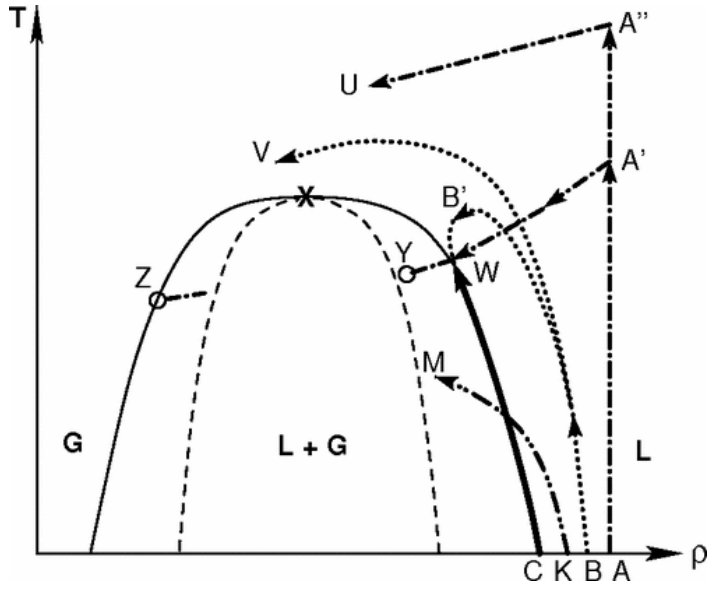

Figure 3.8.: Thermodynamic trajectories of a hypothetical semiconductor or metal under fs (dashed-dotted line), ps (dotted line), and ns (thick solid line) laser irradiation. Thin solid line: binodal; dashed line: spinodal; X: critical point. L: liquid; G: gas. Reproduced from [110]

For non-conducting material the penetration depth and absorptivity seems to be more important for a smaller PSD and improved quantification, as lasers with lower wavelengths deliver better results. Glaus *et al.* actually reported an enhanced fractionation for the matrix elements of zircon for UV-fs-laser in comparison to UV-ns-laser.[67] Ohata *et al.* compared 795 nm and 265 nm fs-laser with 193 nm ns-laser and found superior figures of merit for the utraviolet (UV) systems compared to the NIR system for conducting materials.[111]

As the beam profile of fs-laser systems is usually a Gaussian one, the ablation crater will

look very different. Even when starting at the same spot size, a Gaussian beam will lead within a few hundred pulses to a conical shape (see Figure 3.9). In this study, it was also reported that for the beginning of the ablation (20 s with 5 Hz), a similar fractionation index is achieved in comparison to ArF laser.[66] If examined in detail, the first 10 s show almost no fractionation, while fractionation is increasing even higher than for ns-LA after 30 s.

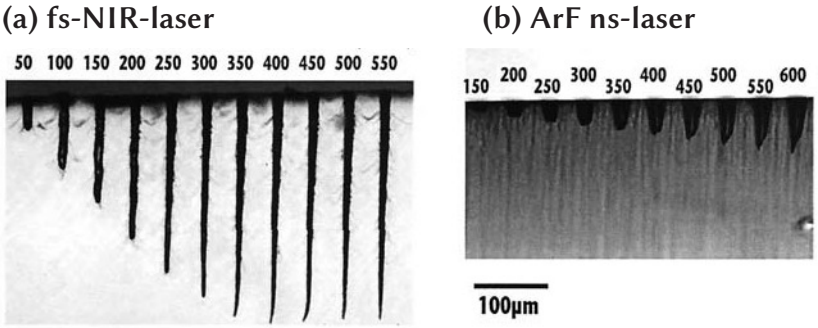

Figure 3.9.: Comparison of ablation crater produced on Pyrex glass by a (a) fs-NIR-laser with 100 µJ pulse energy and (b) ArF excimer ns-laser with 140 mJ, reproduced from ref. [66]. The numbers above the crater indicate the number of pulses applied.

For this study a GeoLas 193 nm ArF excimer (Coherent, Germany) system was used and compared to an Excite Pharos femtosecond Laser Ablation System (Teledyne CETAC Technologies, Bozeman, MT, USA), based on Yb:KGW as laser medium. The fundamental wavelength is 1028 nm, but it was used in the frequency quadrupled mode of 257 nm, with a pulse width of 190 fs.

3.4. Gas Exchange Device

The gas exchange device (GED) used in the experiments was produced by J-Science Lab Co., Ltd (Kyoto, Japan) and is identical with the GED III or Q-GED used and characterised by Tabersky *et al.*[112] The Q-GED is the current stage of development of a system to

exchange air or other gases with argon. This allows for a sampling of particles in air to an ICP and was initially used to analyse airborne particles in an ICPMS in real time.[113] In combination with LA-ICPMS, a GED with an exchange rate of air of 0.21 L/min was used to facilitate sampling outside of a conventional ablation cell. Direct atmospheric sampling was accomplished using a diaphragm pump to suck the laser-generated aerosol into the ICP with sensitivity decrease of approximately 20 %.[114] It was also shown that this setup is useful for isotope ratio measurements with a MC-ICPMS with comparable results for scanning mode under air.[115]

The direct sampling approach was further improved by an aerosol entrainment device to catch most of the aerosol formed during the ablation process.[112] If coupled to a Schwarzschild objective and in connection with a GED that enables gas exchange of 0.8 L/min, it was now possible to analyse long pieces of stalagmites with high spatial resolution.[112] This Q-GED consists of 4 parallel membrane tubes of 50 cm length each with a pore size of 70 nm.

The basic principle of the GED, i.e. diffusion through a porous silica membrane without additional pressure, is described by Graham's law:

$$J_{out} = J_{in} \cdot \sqrt{\frac{M_{in}}{M_{sweep}}} \tag{3.20}$$

with $J_{in/out}$ denoting the carrier gas flow rate *in* and *out* of the GED, M_{in} the molecular weight of the carrier gas which should be exchanged and M_{sweep} the gas to which to exchange, in this case Ar.

In connection with an ICPMS, zero pressure cannot be assumed, as the inner diameter

of the inner torch tube is between 0.8 and 2.5 mm (in this study 1.5 mm) and thus smaller than the inner diameter of the tubing (generally 4 mm). To prevent gas flow (in contrast to diffusion) out of the membranes and to stabilise the flight path of the particles, a small over pressure has to be applied. So for 10 L/min of Ar as sweep gas, 0.8 L/min of air could be efficiently exchanged to Ar without significant influence of N_2 in the plasma. A rough estimate (Equation (3.21)) for He as carrier gas reveals the possibility to increase the maximum gas flow up to 2.7 times.

$$\sqrt{\frac{M_{Air}}{M_{He}}} = \sqrt{\frac{29}{4}} = 2.7 \tag{3.21}$$

Typical flow rates of He in LA-ICPMS are around 1 - 1.5 L/min, which are well within this estimated range. In the experiments presented here, a flow rate of 1 L/min He was used, which also allowed the complete exchange of small amounts of additional gas. A summary of the parameters can be found in Table 3.2.

Table 3.2.: GED parameter settings for mixed carrier gas experiments in Chapter 4

Parameter	Setting value
GED model	GED III (Q-GED)
Ar sweep gas	10 L/min
Overpressure	400 Pa
Carrier gas flow (He +X) inflow	$\leq$ 1.01 L/min
Carrier gas Ar outflow	0.485 L/min

3.5. Mixed Gases

When discussing the effects of different gas mixtures from the state of the art in LA-ICPMS,[116] i.e. between 0.3 and 1.2 L/min of He in one or multiple gas inlets of the ablation chamber and between 0.6 and 0.9 L/min Ar to stabilise the plasma, it has to be differentiated between an addition before the ablation chamber and after the ablation chamber, as this can lead to different conclusions about the influence of the gas addition. Sometimes this is not easily distinguishable in previously reported studies, but these topics are addressed separately here.

During the evaluation of reports on mixed gas LA-ICPMS, it is important to recognise two different settings: 1. The gas was mixed with the carrier gas of the laser generated aerosol before the ablation chamber and 2. The gas was mixed with the carrier gas after the ablation chamber. The latter can be principally looked at as a gas addition to the ICP, but not to the laser ablation process. The difference to the studies mentioned above with liquid introduction is mainly the presence of a dry laser generated aerosol in the ICP instead of a wet aerosol generated by a nebulizer and spray chamber.

3.5.1. Mixed Gas Conditions in ICP

Gases mixed to an Ar ICP have been studied and reviewed since the beginning of the use of an ICP as an ion source in atomic emission spectroscopy (AES) and MS.[117–119] The introduction of additional elemental gases like He, H_2, N_2 and O_2 have been investigated in the outer gas stream, as well as in the intermediate and central channel. These additions affected the electron number density, the electron temperature and the gas temperature depending on which gas was introduced in which gas stream. H_2 and N_2 showed an increase

of gas and electron temperature and also increased the channel width of the central gas channel, if introduced this way. He on the other hand, did not change the temperatures or electron density much, but resulted in a higher ionisation, similar to H_2 and N_2.[119] O_2 was used specifically in applications with organic matrices to increase oxidation of carbon and thus avoid carbon deposition on parts of the system like sampler cone.[120] In general, the addition of molecular gases in low amounts increases the signal intensity which is attributed to the higher thermal conductivity in comparison to Ar-only plasmas,[121] but might also increase the signal-to-noise and signal-to-background ratios.[122] H_2 and N_2 can reduce the formation of oxide species like $^{40}Ar^{16}O^+$;[121,123] O_2 addition will enhance these.[123]

Other molecular gases like methane,[124] ethene,[125] or organic solvents like propan-2-ol[123] have been added to the central Ar flow and proven to be particularly useful to remove argon-based polyatomic interferences like $^{40}Ar^{35}Cl^+$ and $^{38}Ar^{38}Ar^+$ and also $^{40}Ar^{16}O^+$ and MO^+ for oxygen-free organic molecules.

The addition or presence of water in the ICP has been discussed in a variety of studies.[126–130] Although there are contradictions in some studies, in general, the formation of isobaric interferences based on oxides and hydroxide is reduced by at least an order of magnitude and the sensitivity is subsequently enhanced. Further discussion about wet and dry plasma conditions can be found in Section 3.6.

3.5.2. Mixed Gas Conditions during LA

Guillong and Heinrich[131] mixed He with extra gases (H_2, N_2 and CH_4) before the ablation chamber, but claimed that there is no visible difference in ablation behaviour at an addition of up to 2 % of He flow. H_2 led to an increase of sensitivity by a factor of 2-3 for

most elements, with positive exception of 6-7 for Be, P and As. The oxide formation was not altered by the addition, but the formation of doubly-charged ions and hydrides increased. N_2 and CH_4 addition could only offer an increase of sensitivity up to a factor of 1.6 and 3.2, respectively. Košler and associates[132] introduced O_2 before the ablation chamber and observed a change in fractionation for NIST SRM 610, 91500 zircon and a NiS sample. A set of chemical reactions in the laser-generated plasma plume was proposed as the dominant reason for this change. Frick and Günther[133] investigated the addition of oxygen during a broader study concerning the ablation behaviour of carbon containing matrices. Here, during the ablation of diamonds, a substantial amount of carbon was transported in the gas phase, when 20 mL/min O_2 were added to the ablation chamber, presumably converting solid carbon species into CO_2.

Some studies investigated the addition of water to the laser-generated aerosol in the context of calibration with liquid standard solutions and found more stable plasma conditions, a higher tolerance of mass load and more accurate results.[134,135] Following this phenomenon, Flamigni *et al.*[136] investigated the vaporisation point or aerosol penetration depth (APD) of different element species with respect to wet or dry plasma. The optimal water content for vaporisation at the same APD was found to be 20-30 % relative humidity. This should allow better accuracies for non-matrix-matched calibration protocols.

Finally, it has to be mentioned that various labs have had different results when adding non-argon gases. Especially for LA-ICPMS with various tubing and connections it is difficult to evaluate whether a certain background level of N_2 or O_2 originating from air is already present in the system and further addition shows no effect. These might be caused by small leakages or the diffusion of air through gas tubing. Diffusion of N_2 from the edge into the core of the ICP was reported as negligible.[137]

The experiments reported in Chapter 4 focus on the separation of the effect of extra gas introduced either to the ICP or to the laser ablation chamber exclusively, when applied to U-Pb dating with LA-ICPMS.

3.5.3. Setup of Mixed Gas Experiments

As mentioned above, to comprehensively investigate the effects of small amounts of extra gas in carrier gas on the ablation process, there has to be a removal of the additions after the ablation chamber. This allows for constant plasma conditions while changing the ablation conditions. In presented experiments, a GED (see Section 3.4) has been inserted in the tubing after the ablation chamber and before the ICP, which is shown schematically in Figure 3.10.

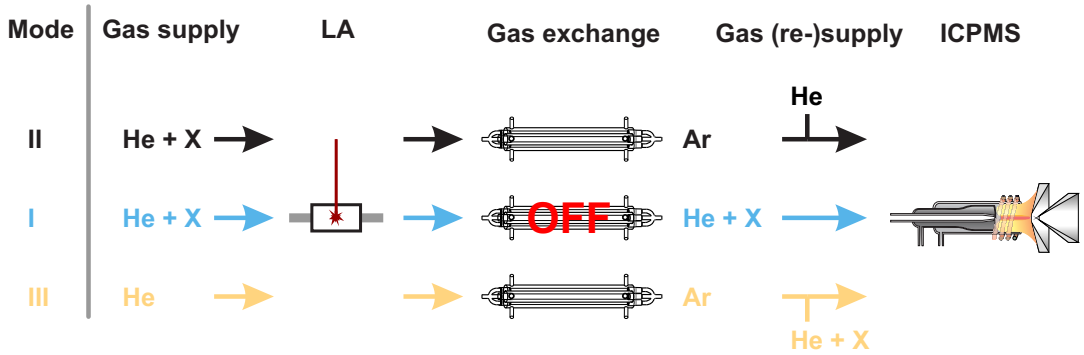

Figure 3.10.: Schematic of the three modes of operation used to study the over-all $^{206}Pb/^{238}U$ fractionation (mode I / blue), a LA-induced effects (mode II / black), and ICP-induced effects (mode III / yellow) separately. In mode II and III He and He + X (X = H_2, N_2, O_2, H_2O) are (re-)supplied in front of the ICP to keep gas conditions constant; in mode I Ar is supplied in front of the ICP (not shown).

The addition of H_2, N_2, O_2 and H_2O at different parts of the laser ablation system was investigated in this work. Diatomic gases were added at levels of 5 and 10 mL/min to a 1 L/min of He carrier gas flow by means of a mass flow controller (0-100 mL/min, ANALYT-

MTC, Müllheim, Germany). Humidification of He was achieved using a gas wash bottle. The level relative humidity (RH) was measured in-line by a capacitive-type sensor (RHT05, MaxDetect Technology Co. Ltd, Shenzhen, China) For 99 % RH, the bubbling through water was sufficient. To achieve a RH of approximately 25 %, two different approaches have been employed. The first setup, as used with the ns-LA-ICPMS experiments, consisted of a conventional cooling trap with approximately 5 cm diameter. It was filled so that the water did not reach the inlet of the gas. This specific setup facilitated a humidification of 1 L/min He to 25 % RH. A drawback was that it turned out to be difficult to maintain the same humidification level over a longer period of time. The water level decreased due to the removal of water and resulted in a reduction of effective water surface, which in turn decreased the effective humidification. In further experiments, i.e. with fs-LA-ICPMS, a gas wash bottle with cylindrical shape was used, so that, even with a reduced water level, a constant water surface and RH could be obtained (see Figure 3.11). The degree of RH could now be determined by using a split gas flow and a pinch cock to tune the amount of He gas getting humidified, and in consequence, the total RH level.

To separate LA and plasma effects, three different mixing conditions were applied:

I The standard way of operation, LA and plasma effect: He with extra gases is lead through the ablation cell and further through the switched-off GED to the ICP. Ar is mixed in before the plasma.

II GED on, LA effect: He with extra gases flows through the ablation cell and is later on exchanged in the GED to argon. Before the ICP, additional He (1 L/min) was added to obtain the same plasma conditions as under standard conditions.

III GED on, plasma effect: He without any extra gas flows through the ablation cell

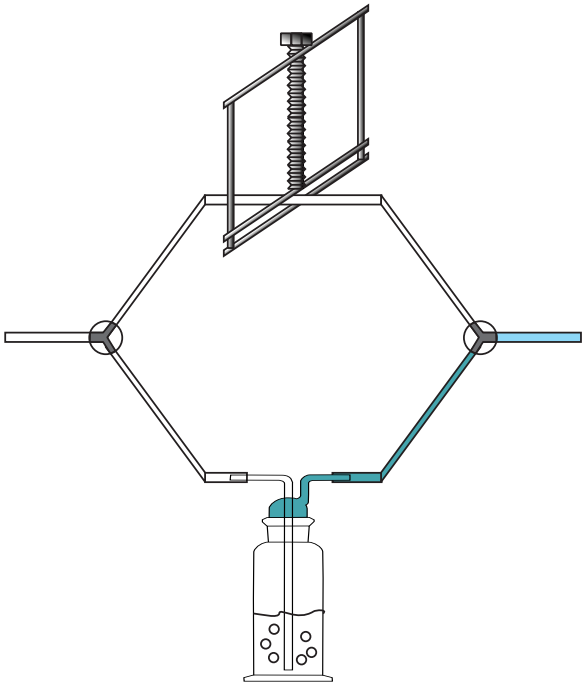

Figure 3.11.: Final setup for gas humidification with adjustable pinch cock. Blue indicating humidified gas. If the pinch cock is opened slightly, a fine tuning of RH after the remixing is possible.

and gets exchanged through the GED to argon, which is mixed with He and the additional gases to see only the influence of these gases on the ICP.

As a way to tune the instrument for similar conditions in the ICP, without the introduction of laser-generated aerosol, a metallic gas generator (MGG) (J-Science Lab Co., Ltd, Kyoto, Japan) was inserted before the plasma. This was useful, as otherwise the modified conditions in the ablation chamber could already influence the tuning result. The working principle can be seen in Figure 3.12, and consists of a reservoir of metal carbonyls, which sublimate out of a capillary and semi-permeable membrane. The emission rate of this device is mainly influenced by the temperature and gas flow rate through the upper part.[138]

The MGG was used before to tune ICPMS instruments for the analysis of airborne

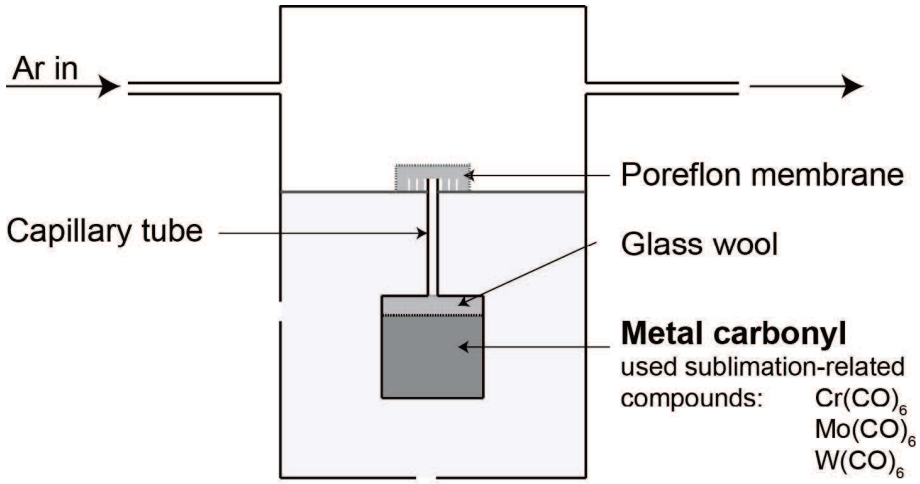

Figure 3.12.: Schematic of the metallic gas generator (MGG). Reproduced from ref. [138]

particles.[113] Further studies by Tabersky investigated the long term stability[138] and, therefore, its suitability as a general monitor for (stable) plasma conditions. As such, it has been used in this work to monitor sensitivity of $^{182}W^{+}$ and to keep it as constant as possible. This worked well in mode **II** as long as no extra gas was introduced to the ICP. For modes **I** and **III** the effects of the extra gases (most prominent for 10 mL/min of N_2 and O_2) made it necessary to reduce the total gas flow by approximately 0.14 L/min Ar record meaningful signal.

3.6. Desolvator System

Already in the very early days of ICPMS analytic systems, efforts have been made to reduce the water and subsequently the mass load in the plasma, as water promotes the formation of certain polyatomic species (e.g. MO^{+}, MOH^{+}). One first attempt was made by simply cooling the spray chamber to allow for more condensation and less total water content in the gas transported to the plasma.[139] Hutton and Eaton reported an increase in

sensitivity of 3-7 times for different elements and a reduction of MO^+ by a factor of 2 when cooling from 30 to 0 °C .[140] This concept has been further developed to include a heating device and a cooling device in series to allow first for a high degree of vaporisation, i.e. reducing the droplet size, and then for a condensation of the water vapour to the walls of a condenser.[13,141] Comprehensive studies concerning the optimal water load have been completed with these devices,[126,142] with the result that the highest sensitivity can be achieved with a combination of low, but not zero, water load, optimal distance of the torch to the sampler cone and the right nebulizer or carrier gas flow rate. Interestingly, for total sample consumption system, a heating of the aerosol produced by the nebulizer can also enhance the sensitivity.[143]

Changing the fundamental process from condensation to evaporation lead to the development of membrane desolvator systems,[144,145] which vaporise organic[146] or water[147] droplet and allow diffusion through a membrane out of the sample gas stream. A temperature gradient was applied over the membrane, which is more permeable for the solvent than for aerosol particles.

Desolvated aerosols do not only reduce the formation of isobaric interferences based on oxygen species but also species containing chlorine atoms (e.g. Cl_2^+ or $ArCl^+$) in case the solvent has a high HCl content as in *aqua regia* digestion protocols.[148] An intensive study confirming this effect and comparing different desolvation systems for specific analytical questions, like the influence on the $^{139}La^{16}O^+/^{139}La^+$ratio has been reported by Minnich and Houk.[127] It was found that the $^{139}La^{16}O^+/^{139}La^+$slightly decreased for condenser desolvation but more prominently for cryogenic and membrane desolvation systems. An important finding is also that the sensitivity peak of $^{139}La^{16}O^+$ and $^{139}La^+$ is different by an aerosol gas flow rate of 0.4 L/min for the ultrasonic nebulizer used in the study.

In addition to all the advantages, some loss of sensitivity for certain elements have been reported for membrane[149] as well as for condenser systems,[150] so for each application careful consideration has to be taken.

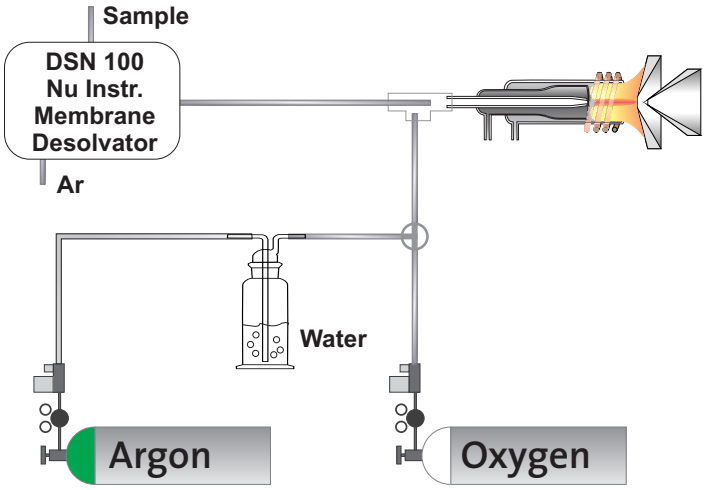

Figure 3.13.: Setup for selective oxidation studies; the humidification part was only used together with the quadrupole ICPMS.

In this thesis (see Chapter 5), a membrane desolvator DSN-100 (Nu Instruments Ltd., Wexham, UK) was not primarily used because of the reduction of isobaric interferences, but because the dry aerosol allows to mimic the sample and plasma conditions of laser-generated aerosols. With this setup (Figure 3.13), a continuous sample introduction of LA-like aerosol could be maintained, and the conditions of additional O_2 and lower plasma power were investigated. Furthermore, different concentrations — and, in principle, different isotopic compositions of samples — could be generated for dry aerosols, which would be complicated from solids. This effect has been used to employ desolvated aerosol as calibration for laser generated aerosols,[151] which was later improved by using He as carrier gas for the LA part.[149]

The DSN-100 was coupled to an Agilent 7500cs (Agilent Technologies, Waldbronn,

Germany) and to a Nu Plasma (Nu Instruments Ltd., Wexham, UK) ICPMS; typical operating conditions can be found in Table 3.3.

Table 3.3.: GED parameter settings for experiments with desolvated aerosols in Chapter 5

Parameter	Setting value
Desolvator	DSN-100
Nebulizer pressure	35-38 psi
Membrane gas	2.3 - 2.6 L/min
Hot gas	0.2 - 0.3 L/min
Spray chamber temp.	105 °C
Membrane temp.	110 °C

4. U-Pb Fractionation with Carrier Gas Mixtures on Zircons

Parts of this chapter and the corresponding materials section have been submitted for publication to the *Journal of Analytical Atomic Spectrometry*.

4.1. Separation of LA and ICP Effects

The evaluation of LA-ICPMS raw data was carried out using the in-house developed, python-based software Stalquant,[152] which allows us to perform an automated background correction and to integrate background-corrected sets of data. Results were further processed and plotted using the statistics software packages R (ver. 3.0.2)[153] and ggplot2.[154] Error bars shown in all graphs refer to the 95 % confidence interval according to the t-distribution. Element ratios were evaluated both point by point and from integrated signals. Point-by-point analysis enables the determination of progressive changes in the course of analysis due to down-hole fractionation, as mentioned above. For integrated-signal analysis, average element ratios were calculated by first integrating the signals of each isotope over the same acquisition time range and then dividing them; in other words,

this is the ROM. This data reduction approach may result in different element ratios from those calculated from the arithmetic mean of point-by-point ratios, *i.e.* the MOR.[73] This occurs if the slope of element ratios deviates from linearity.

To allow differentiation of over-all fractionation into system mass bias and down-hole fractionation, the processing scheme proposed by Sylvester and Ghaderi that rests upon a linear regression of the $^{206}Pb/^{238}U$ ratio vs. time was used.[155] This scheme assumes that over-all fractionation is given by averaged $^{206}Pb/^{238}U$ ratios and the *correct* or *mass-biased* $^{206}Pb/^{238}U$ to occur at the beginning of analysis, which is calculated as the intercept of linear regression curves with the vertical axis at the starting point of LA. The term *mass-biased* refers to the system (and material) dependent fractionation for crater aspect ratios close to zero. Furthermore, the slope of each regression curve serves as a quantitative indicator for the degree of down-hole fractionation. Mathematically, the processing scheme partitions the $^{206}Pb/^{238}U$ transient signal according to the following equations:

$$R_{206/238} = \frac{I_{^{206}\mathrm{Pb}}}{I_{^{238}\mathrm{U}}} \tag{4.1}$$

$$R_{206/238}(t) = a + b \cdot t = \underbrace{R_{206/238}\big|_{t=0}}_{a} + \underbrace{\frac{\mathrm{d}\,R_{206/238}(t)}{\mathrm{d}\,t}}_{b} \cdot t \tag{4.2}$$

with I and R denoting signal intensities and ratio measured for ^{206}Pb and ^{238}U and t the acquisition time. Parameters a and b refer to the intensity ratio at $t = 0$ (intercept) and the gradient of the intensity ratio increase in units of $[b]$ =1/ s (slope), respectively.

4.2. ns-LA-ICPMS with Mixed Gases

In this section, the most relevant findings regarding the effect of different carrier gas mixtures on the $^{206}Pb/^{238}U$ ratio with the ns-LA system are outlined and discussed. Further information on $^{29}Si/^{91}Zr$, $^{238}U/^{232}Th$, and $^{232}Th^{16}O/^{232}Th$ ratios, which are often used (i) to specify fractionation of zircon main constituents,[57,85] (ii) to indicate ICP-induced fractionation due to incomplete evaporation of particles,[27] and (iii) to monitor the oxide formation rate, are provided in Appendix A.2. Since this study comprises quite a large number of parameters including several samples, flow rates, levels of RH, etc., plotted data are colour-coded according to the respective mode of operation (see Figure 3.10). In addition, results are occasionally discussed in terms of mode of operation instead of category of fractionation for brevity.

The general settings of the experiments discussed in this section can be found in Table 4.1.

4.2.1. $^{206}Pb/^{238}U$ Over-All Fractionation

Changes of averaged $^{206}Pb/^{238}U$ intensity ratios used as indicator for over-all fractionation, as discussed in Section 4.1, were calculated from LA-ICPMS raw data of NIST 610, as well as from Plešovice and 91500 natural zircons using different carrier gas mixtures (Figure 4.1). Averaged intensity ratios were taken across the middle 53 s of a 60 s-long LA-ICPMS signal. As it can be seen in Figure 4.1, $^{206}Pb/^{238}U$ ratios followed similar trends for all samples when looking at patterns column-wise. This implies, that little material dependency occurred under each of the conditions. In addition, the colour-coding reveals that LA-induced effects are the least pronounced for all gas mixtures except that of H_2O (left column) and, to some extent, H_2 (middle left column). Here, overall changes of the $^{206}Pb/^{238}U$ ratio were in a range

Table 4.1.: General settings for fractionation study using ns-LA

Parameter	Setting value
Laser Ablation	
System	GeoLas excimer laser
Wavelength	193 nm (ArF)
Pulse duration	25 ns
Number of pulses	600
Repetition rate	10 Hz
Fluence	9 J/cm^2
Spot diameter	24 µm
LA mode	Single hole drilling
ICPMS	
Rf-power	1450 W
Over-all flow rate	1.0 L/min He + 0.7 L/min Ar
Q-GED	
Ar sweep gas flow rate	10 L/min
He + X carrier gas flow rate	$\leq$ 1.01 L/min

of 10 to 19 %, depending on the sample and mode of operation. $^{206}Pb/^{238}U$ ratios determined for modes II and III diverged, and more specifically, anti-correlated at increased levels of RH whereby the arithmetic means of ratios closely matched values found for mode I. The anti-correlation suggests that LA- and ICP-induced fractionation occurred simultaneously, and that the corresponding shifts of $^{206}Pb/^{238}U$ ratios are opposite in direction. It also proves that conditions can be accurately reproduced when switching between modes of operation and, thereby, supports the significance of the data.

In contrast, no such a strong correlation of $^{206}Pb/^{238}U$ ratios was found in cases of H_2, N_2, or O_2 admixtures, which indicates slight drifts of the ICP operating conditions in the course of analysis even though re-optimisation was systematically performed. Nevertheless, the patterns of respective data points turned out to be representative and allowed conclusions on

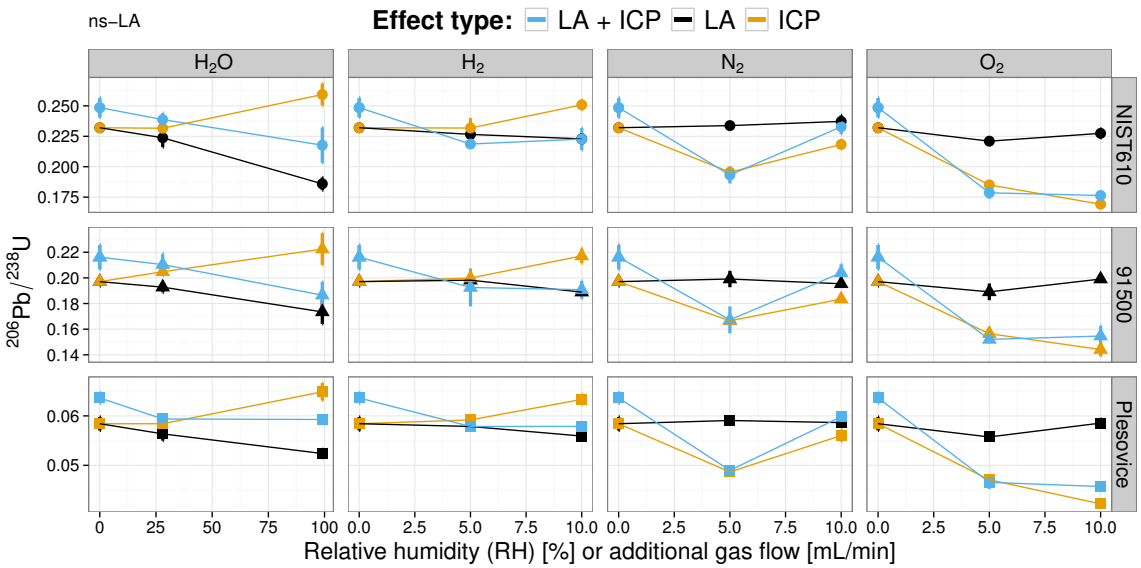

Figure 4.1.: $^{206}Pb/^{238}U$ ratios averaged over an acquisition timeframe of 53 s with ns-LA. Data points represent the mean of 3 to 12 measurements and error bars refer to the 95 % confidence interval of the mean.

whether LA- or ICP-induced effects prevailed. For instance, $^{206}Pb/^{238}U$ ratios recorded when applying modes I and III varied equally while mode II resulted in almost constant values, independent of sample material and concentration of gases. Assuming the aforementioned drifts in the ICPMS operating conditions to be negligible, this correlation can be understood as an evidence for the absence, or at least the unimportance, of LA-induced fractionation in the presence of H_2, N_2, or O_2 in the ablation chamber. Notably, $^{206}Pb/^{238}U$ ratios monitored during the admixture of N_2 dropped at a gas flow rates of 5 mL/min but almost returned to initial values when the flow rate was set to 10 mL/min. In addition, when either O_2 or N_2 was admixed at rates of 10 mL/min, the Ar flow rate needed to be reduced by 0.14 L/min to obtain sufficient ion yields and, thus, ICPMS signal intensities.

4.2.2. $^{206}Pb/^{238}U$ System Mass Bias and Down-Hole Fractionation

To interpret how changes in the $^{206}Pb/^{238}U$ ratios were correlated to system mass bias and down-hole fractionation, point-by-point data were plotted vs. acquisition time, and fitted to a line to determine both intercepts and slopes, as discussed above. In Figure 4.2, three such plots are shown for LA-ICPMS of natural zircon 91500 with the addition of H_2O at 99 % RH; results for each mode of operation are presented. Most striking, the slope turned negative when switching from mode III to modes I or II, which re-confirmed that LA- and ICP-induced down-hole fractionation coexist, but shift $^{206}Pb/^{238}U$ ratios with unlike signs. Yet, ICP-induced shifts were still lower so that the net $^{206}Pb/^{238}U$ ratio slightly decreased by approximately 0.001 per second (cf. mode I). Nevertheless, the absolute value of the slope was suppressed by a factor of 2 when compared to data obtained for zero to about 25 % RH, as can be seen in the left column of Figure 4.3. Similar trends were also observed for the slopes of $^{206}Pb/^{238}U$ ratios recorded during LA-ICPMS analysis of Plešovice and NIST 610 with suppression factors of 0.5 and 2, respectively.

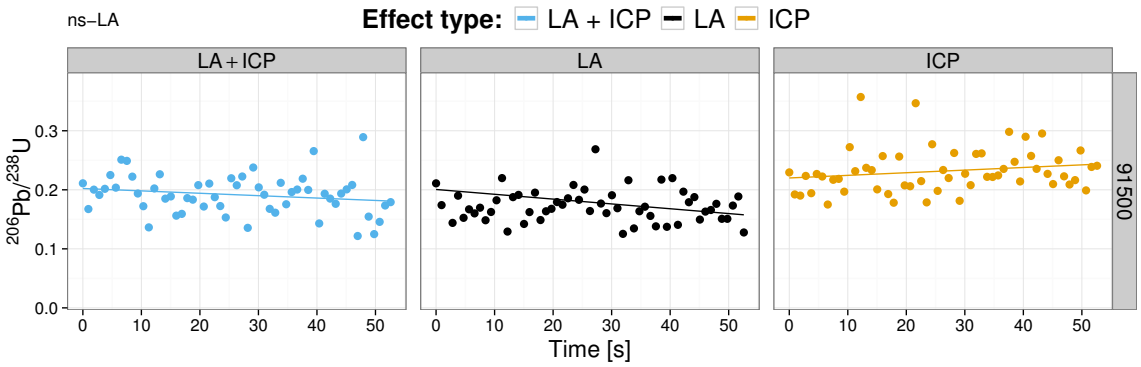

Figure 4.2.: Point-by-point $^{206}Pb/^{238}U$ plots indicating over-all as well as LA- and ICP-induced fractionation during the analysis of 91500 zircon with a carrier gas of He + 99 % RH. Solid lines are linear regression curves.

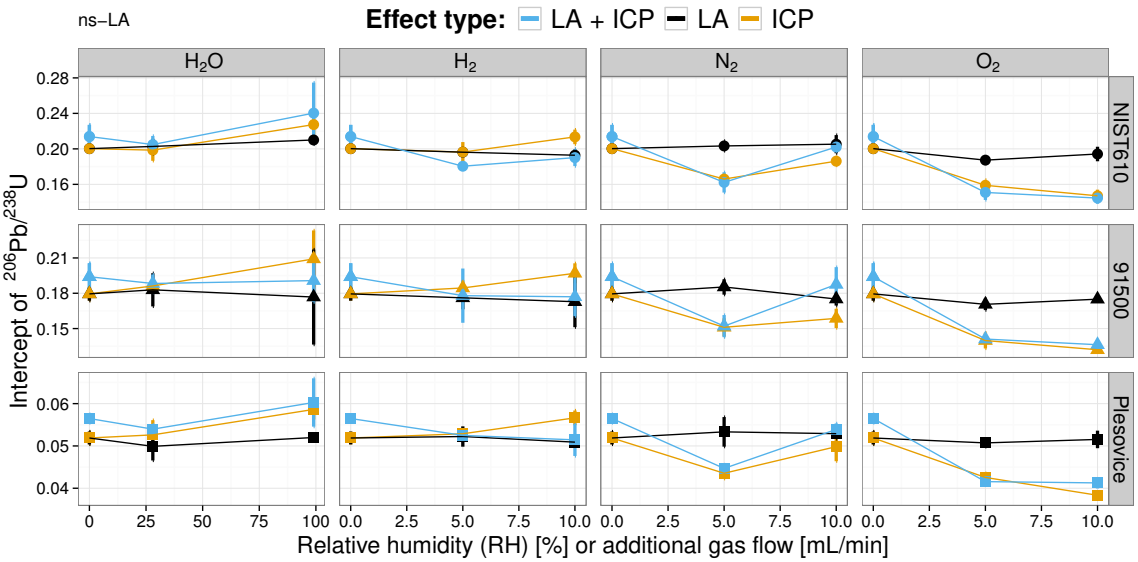

Figure 4.3.: Slopes of $^{206}Pb/^{238}U$ ratios calculated from regression curves of point-by-point plots, as shown in Figure 4.2. Data points represent the mean of 3 to 12 measurements and error bars refer to the 95 % confidence interval of the mean.

It has to be said that the conditions used here were *not* optimized to cancel out LA- and ICP-induced effects completely and, thus, to provide best performance in terms of down-hole fractionation suppression. In fact, suppression factors even higher than those reported here could be achieved when carefully adjusting levels of RH prior to analyses. As shown in Figure 4.3, optimum ranges of RH for the system used here are between 50 % and 99 %. For NIST 610, the slope reaches zero (*i.e.*, no down-hole fractionation) at a RH lower than that for zircons. The admixtures of H_2, N_2, and, in particular, O_2 did not alter the slopes of regression curves as markedly as H_2O. When taking into account the measurement uncertainty, the additions of H_2, N_2, and, O_2 show no trend in suppressed $^{206}Pb/^{238}U$ fractionation, which contradict the findings recently reported by Košler *et al.*[75]

Intercepts of regression curves which, by definition, represent correct or mass-biased

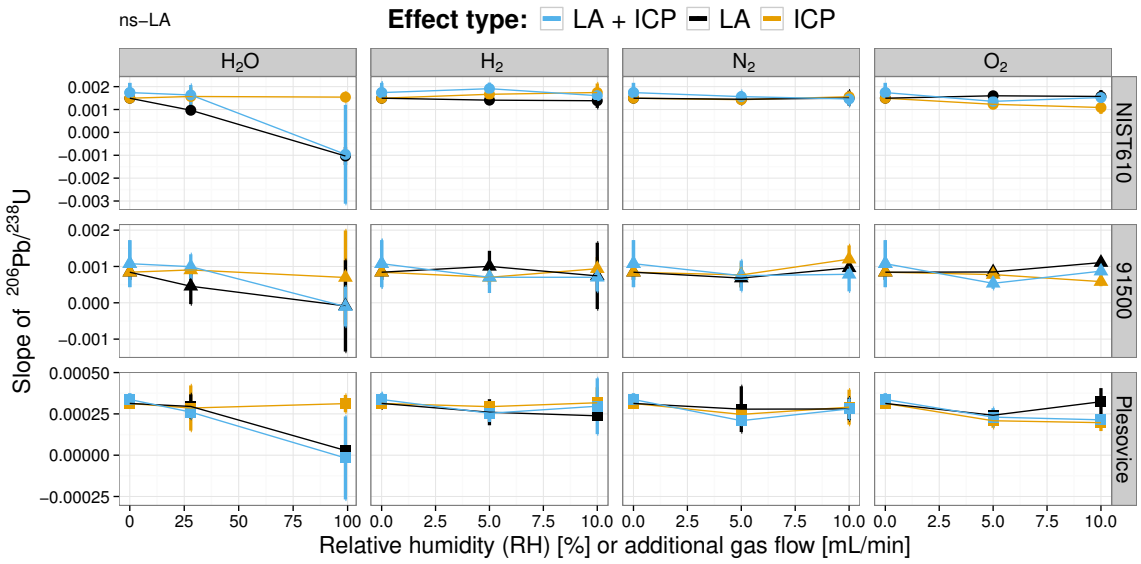

Figure 4.4.: Slopes of $^{206}Pb/^{238}U$ ratios calculated from regression curves of point-by-point plots, as shown in Figure 4.2. Data points represent the mean of 3 to 12 measurements and error bars refer to the 95 % confidence interval of the mean.

$^{206}Pb/^{238}U$ ratios, are shown in Figure 4.4 for completeness. According to Section 4.1 the intercept is the offset value of the $^{206}Pb/^{238}U$ isotope ratio given by the averaged isotope ratio minus the mean of temporal changes of the isotope ratio. Therefore, data points shown in Figure 4.4 allow the determination of the shift in the mean value of $^{206}Pb/^{238}U$ ratios due to down-hole fractionation. For example, the percentage change of the $^{206}Pb/^{238}U$ ratio due to down-hole fractionation for LA-ICPMS analysis of the Plešovice zircon with He + O_2 (5 mL/min) was + 2.8 %, whereas He + H_2O (99 % RH) caused no detectable change. Considering the results presented so far, the admixture of high amounts of H_2O, on one hand, helped suppress down-hole fractionation. On the other hand, it also increased the system mass bias significantly, with the $^{206}Pb/^{238}U$ ratio reduced by up to 20 %, depending on RH, sample material, and mode of operation, as can be seen in Figure 4.4.

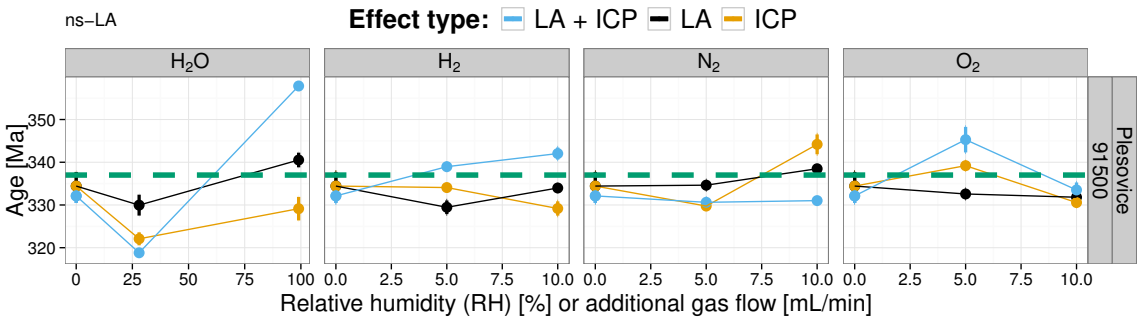

Figure 4.5.: $^{206}Pb/^{238}U$-based ages determined by ns-LA of Plešovice zircon using 91500 as external standard for calibration. Green dashed lines highlight the reference age. Data points represent the mean of 3 to 12 measurements and error bars refer to the 95 % confidence interval of the mean.

As a result, the accuracy of analyses worsened when using He + H_2O vs. He + H_2, N_2, or O_2 carrier gas mixtures for the age determination of zircons by LA-ICPMS. In Figure 4.5, the influence of each carrier gas mixture on the accuracy of U-Pb ages for Plešovice zircon using 91500 as external calibration standard is shown; deviations from the reference age of 337.1 Ma [79] are highlighted by dashed lines. The largest deviation from the reference age was + 6 % and came from case of He + H_2O (99 % RH / mode I); ages calculated for He + H_2, N_2, or O_2 gas mixtures did not alter as drastically for all modes of operation. In addition, no clear trend in the age determination accuracy, e.g., from the kind of gas mixture or gas flow rate, was noted, except for He + H_2O. This mixture showed a systematic drop of $^{206}Pb/^{238}U$-based ages up to levels of RH of approximately 25 % followed by a steep rise at a RH of 99 %.

4.2.3. Comments on the Effect of He + H_2O on the $^{206}Pb/^{238}U$ System Mass Bias and Down-Hole Fractionation

The above finding that humidified carrier gas mixtures do not allow for suppression of the $^{206}Pb/^{238}U$ over-all fractionation and even worsen the accuracy of analysis is somewhat contradictory to observations made by, e.g., O'Connor *et al.*[134] and Wälle *et al.*[135] Both groups reported improved accuracies and precisions for LA-ICPMS analysis when H_2O was admixed, at least for the majority of elements studied. Moreover, the mechanisms underlying these improvements were explored by Flamigni *et al.*,[136] who found that the admixture of H_2O better localises the spatial spread of aerosol penetration depth (APD). These APDs define the position along the ICP axis at which evaporation of particles is completed, which, for convenience, can be assumed to happen instantaneously. At the APD, atoms begin to diffuse away from the central channel and to ionise.

The occurrence of $^{206}Pb/^{238}U$ down-hole fractionation is commonly attributed to a decrease of the mean size of particles accompanied by a Pb-enrichment of aerosols with increasing aspect ratio of the crater. As pointed out in an earlier study by Flamigni *et al.*,[156] the decrease of particle sizes, and respective changes, in the composition of aerosols may cause shifts of APDs if carrier gases are not humidified before they enter the ICP. As a result, the relative number of, say, ^{206}Pb vs. ^{238}U ions extracted from the ICP to the MS, may vary over time because losses due to out-of-axis diffusion are dependent on the mass of ions; lighter ions (Pb) diffuse more than heavier ones (U). Therefore, the $^{206}Pb/^{238}U$ ratio monitored in the course of LA-ICPMS is supposed to decrease unless temporal changes in the aerosol composition are stronger.

In fact, data reported here indicate an increase of $^{206}Pb/^{238}U$ ratios in the majority of cases,

implying that the relative Pb-content of aerosols rises and, in this way, (over-)compensates diffusion losses of Pb. Still, since APDs are known to better localise when H_2O is admixed, the humidification of carrier gases should allow the suppression of down-hole fractionation. On the one hand, this was supported by the observations made. On the other hand, a closer look at data plotted in the left column of Figure 4.3 revealed the suppression to predominately arise from LA-induced effects and not from the localisation of APDs, i.e., ICP-induced effects. Slopes of $^{206}Pb/^{238}U$ ratios ranged from positive to negative when humidified carrier gases with increased levels of RH were fed into the ablation cell suggesting the presence of H_2O to promote the amount of U released during the LA process. In addition, the admixture of H_2O was found to enhance the system mass bias, when applied to LA-ICPMS of zircons due to strong decreases in the $^{206}Pb/^{238}U$ ratios. The origin for this enhancement is unclear yet, but might be related to a material-dependency of out-of-axis diffusion rates and/or a lower ICP temperature and, thus, a reduced ionization efficiency of Pb vs. U.

4.3. fs-LA-ICPMS with Mixed Gases

For comparison, the influence of the carrier gas composition on ICPMS fractionation processes was also studied using fs-LA. The general settings of those experiments are summarised in Table 4.2. In the following, the performance of the entire fs-LA-ICPMS setup is compared with the ns-LA-ICPMS in terms of signal stability, intensity and $^{206}Pb/^{238}U$ variation with mixed gases. Finally, the deviation of the age determination of Plešovice will be discussed.

Table 4.2.: General settings for fractionation study using fs-LA

Parameter	Setting value
Laser Ablation	
System	Pharos Excite solid state laser
Wavelength	257 nm (Yb:KGW)
Pulse duration	190 fs
Number of pulses	300
Repetition rate	5 Hz
Fluence	8.8 J/cm^2
Spot diameter	24 µm
LA mode	Single hole drilling
ICPMS	
Rf-power	1450 W
Over-all flow rate	1.0 L/min He + 0.7 L/min Ar
Q-GED	
Ar sweep gas flow rate	10 L/min
He + X carrier gas flow rate	$\leq$ 1.01 L/min

4.3.1. General Remarks on Comparing ns- and fs-LA Data

Comparing two processes scientifically usually means keeping most of the possible parameters fixed, or at least controlled, while varying the parameter of interest. The ablation process, however, is entwined with other features of the entire LA-ICPMS system, so that in the end for any given application only the comparison of ns-LA-ICPMS and fs-LA-ICPMS as whole is reasonable.

As the Pharos fs-LA system used in this work has a Gaussian beam profile, in contrast to the Geolas ns-LA system with a homogenised beam, the ablation behaviour is different. A homogenised beam offers a constant fluence over the entire beam cross-section (*i.e.* ablation spot). Therefore, energy is deposited on the sample material such that the ablation threshold is either reached for all points of the cross-section or for none. The area of the

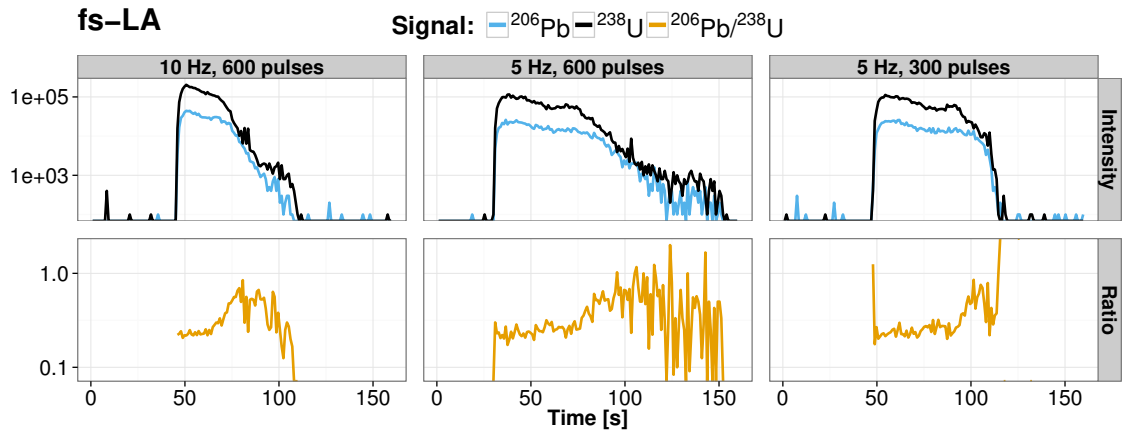

Figure 4.6.: Comparison of different repetition rates and number of pulses; ablation was done with the Pharos system and 50 % energy on a NIST 610 sample

laser spot and, thus the amount of ablated material is reduced over time due to defocusing. A Gaussian beam profile has its highest fluence in the centre of the beam, resulting in laterally varying energy deposited on the sample surface. With a higher number of shots, the ablation threshold might not be reached at all points of the initial surface area, but only in the centre. This leads to a higher aspect ratio of the crater and, together with a reduced particle transport efficiency from deeper crater, to a reduction of signal intensity (see also Figure 3.9).

As a consequence, when ablating with the same settings (10 Hz, 600 pulses) no stable signal was obtained for the entire time of 60 s (Figure 4.6, left column); after approximately 300 pulses the signals decayed very quickly to the background level. If 5 Hz is chosen as repetition rate, the signal is stable over a longer time but still only over 300 pulses (middle column). Consequently, 5 Hz and 300 pulses have been chosen as final settings to obtain a similar amount of stable signal for ns-LA and fs-LA (right column). This corresponds well to the findings by Hirata and Kon, that for NIR-fs-LA with pulse energies of 75-100 µJ a

limit in depth is reached for more than 300-350 shots on Pyrex glass.[66]

Changing the repetition rate and the number of shots applied produced a more stable signal, but it also challenges the quantitative one-to-one comparability of the slope of the linear regression for both types of lasers. Qualitatively and within each set of experiments, the slope of the linear regression should still be a good estimate of the alteration of the down-hole fractionation.

4.3.2. Gas Influence on Signal Intensities

In contrast to the ns-LA experiments, for fs-LA, almost no clear signal enhancement with extra gases was found for ^{206}Pb or ^{238}U signals. For the integrated intensities, in mode I and III, a general trend towards lower signals was observed. As an exception, the medium addition of N_2 (5 mL/min) and the addition of O_2 on both levels in mode I show a slight increase. This raises the question of whether the aerosol generated by fs-LA is so fundamentally different (*e.g.* smaller PSD etc.) in comparison to the ns-LA, that the increased heat conductivity to the central channel in the plasma is not effective. In the case of N_2, the signal enhancement was at most by a factor of 1.5, whereas for the ns-LA used in this work an enhancement up to a factor of 2 was found. This is in the order as the factors reported by Hu *et al.* of 1.7 and 1.9 for U and Pb, respectively.[121] For other conditions, like H_2 and O_2 and H_2O (25 % RH) addition, with ns-LA an enhancement by a factor of 2 could be reached, for fs-LA decreases for H_2 and H_2O, and only small increases to a factor of 1.5 with O_2.

One possible explanation could be the small PSD, which would already allow for a complete vaporisation and ionisation in the plasma and renders the effects of increased heat conduction via diatomic gases useless. The decrease could be the result of a shift of peak

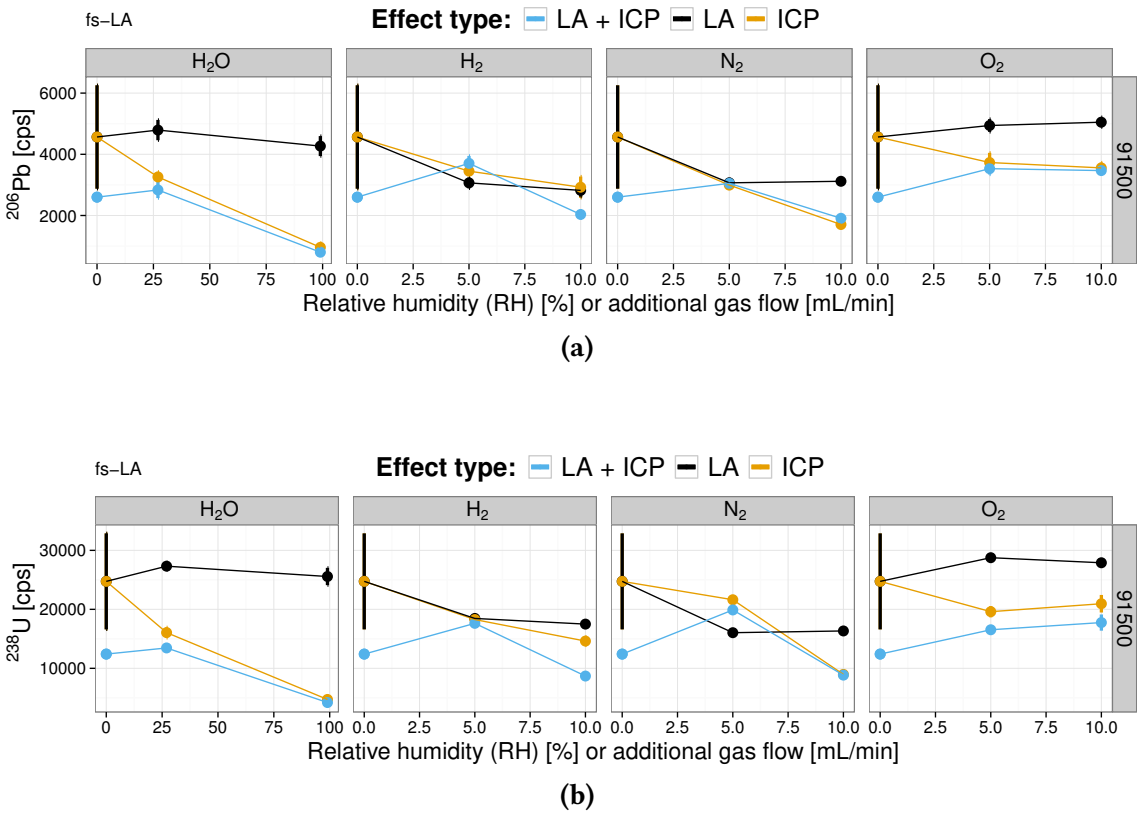

Figure 4.7.: Averaged intensity of ^{206}Pb (a) and ^{238}U (b) for 91500 fs-LA measurement. Data for all other samples and ns-LA can be found in Figures A.11 to A.14

sensitivity, which occurs for diatomic gas addition and can be tuned with the additional Ar gas.[121]

Another observation is that operating in mode II changes the signal intensities quite drastically, which was not the case with the ns-LA, where almost no influence was seen in mode II for H_2, N_2, and O_2.

The oxide ratio (^{232}Th^{16}O/^{232}Th) was more elevated with fs-LA for H_2O and O_2 addition than with ns-LA (see Figure A.8), which could be either the result of a higher interaction rate due to the small PSD or else due to the lower amount of sample material and more

oxygen species in the plasma as a result of lower ablation rate.

4.3.3. $^{206}Pb/^{238}U$ System Mass Bias and Down-Hole Fractionation

The overall fractionation with the fs-LA of the averaged signals can be seen in Figure 4.8. The $^{206}Pb/^{238}U$ ratio for He-only conditions were similar to the ns-LA data for the zircon samples, but were much higher for the NIST 610, *i.e.* 20 % higher when the GED was switched off and 15 % higher when switched on. This is further off the nominal value for NIST 610 of 0.224[57] than with ns-LA, which indicates a less stoichiometric result and a higher system mass bias for fs-LA.The ratio increased even further with the addition of H_2 and O_2 in mode I, as well as H_2 and H_2O in mode III. The phenomenon that the $^{206}Pb/^{238}U$ ratio of mode I lies in between mode II and mode III for H_2O addition is similar as with ns-LA, although a closer look reveals different reasons.

In Figure 4.9 the intercept for fs-LA measurements can be seen. It has to be noted, that the difference between mode I and III was more pronounced than with the ns-LA. Mode II did not affect the intercept with ns-LA much, but here for H_2 and O_2 addition with NIST 610 and N_2 addition with the zircons resulted in positive and negative effects. Surprisingly, the difference in system mass bias for H_2O addition at all levels was very similar for mode II and III, which indicated less influence of H_2O in the plasma.

The change of the slope (see Figure 4.10), indicating down-hole fractionation, is unexpected for the addition of H_2O even in mode II for all samples, when technically no change at the LA conditions should have occurred. For comparison, the complementary graph to Figure 4.2 can be seen in Figure 4.11.

This observation cannot easily be explained, and it shows the actual difficulty and a limit of the approach for separating different effects in LA-ICPMS, while changing the laser

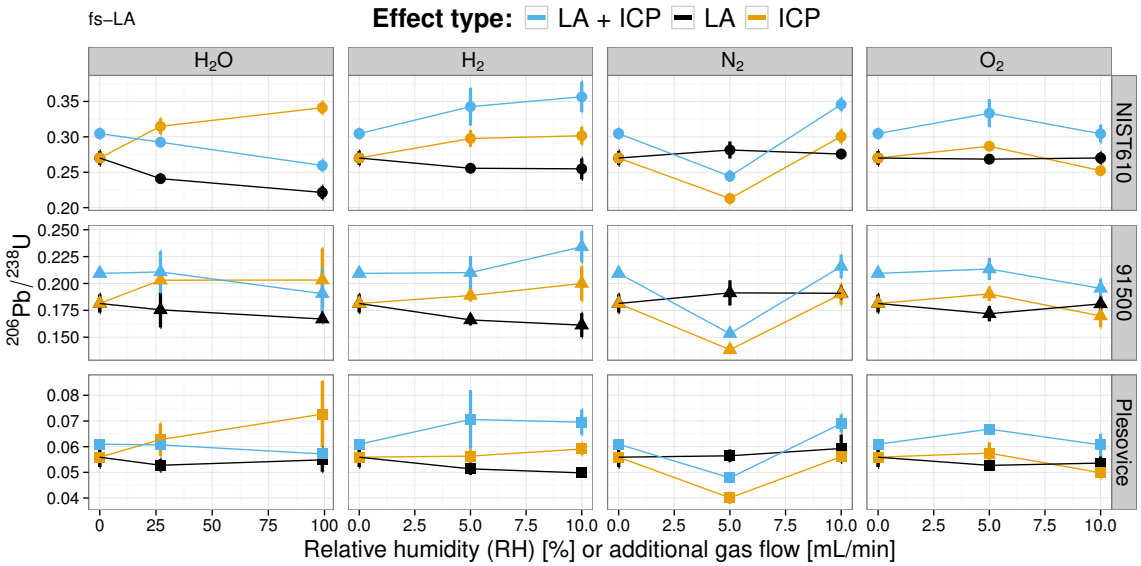

Figure 4.8.: $^{206}Pb/^{238}U$ averaged over an acquisition timeframe of 50 s with fs-LA. Data points represent the mean of 3 to 12 measurements and error bars refer to the 95 % confidence interval of the mean.

system. The change in wavelength and pulse width will result in different PSD, which unfortunately does not only affect the APD of the sample in the plasma, but also may affect the transport efficiency in the gas tubings. These entwined parameters render the design of experiments difficult, in which the influence of every single parameter can be quantitatively or even qualitatively explained. Therefore, it seems reasonable from the application point of view to compare two or more different complete systems in terms of the results.

In Figure 4.12 the final ages obtained by the same calculation as in Figure 4.5 are shown. It stands out that the general variability is very high and that the deviation from the accepted value is very large. Whereas for H_2, N_2 and O_2 in mode II and III a deviation in the range of -3.5 to +3.5 % has been found, the deviation in mode I was higher, *i.e.* +6.8 % for He + 10 mL/min N_2 and +11 % for He + 5 mL/min H_2. The deviation for 99 % RH and mode III

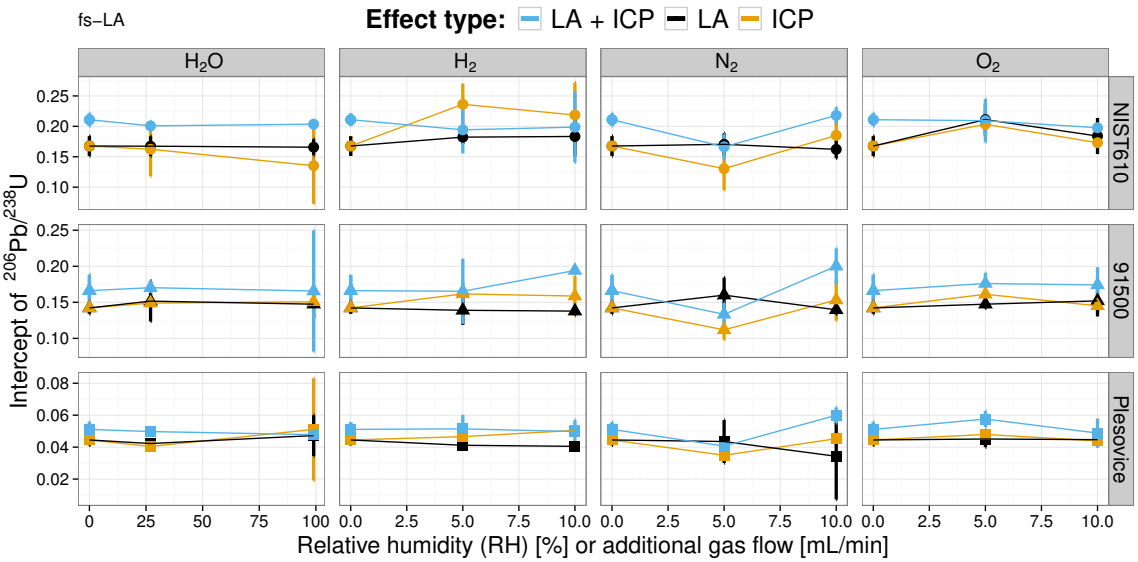

Figure 4.9.: Intercept of $^{206}Pb/^{238}U$ ratios with fs-LA calculated from regression curves of point-by-point plots, as shown in Figure 4.11. Data points represent the mean of 3 to 12 measurements and error bars refer to the 95 % confidence interval of the mean.

was the highest of all with +19 %, mode II resulted in +10 %, and mode I hit the accepted age while following the trend of mode II.

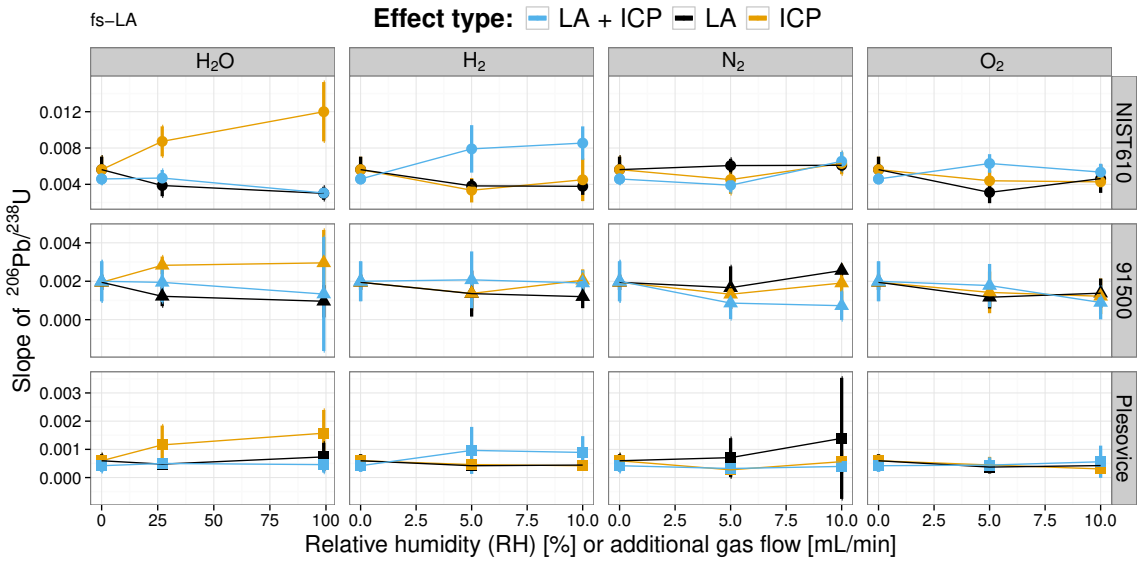

Figure 4.10.: Slopes of $^{206}Pb/^{238}U$ ratios with fs-LA calculated from regression curves of point-by-point plots, as shown in Figure 4.11. Data points represent the mean of 3 to 12 measurements and error bars refer to the 95 % confidence interval of the mean.

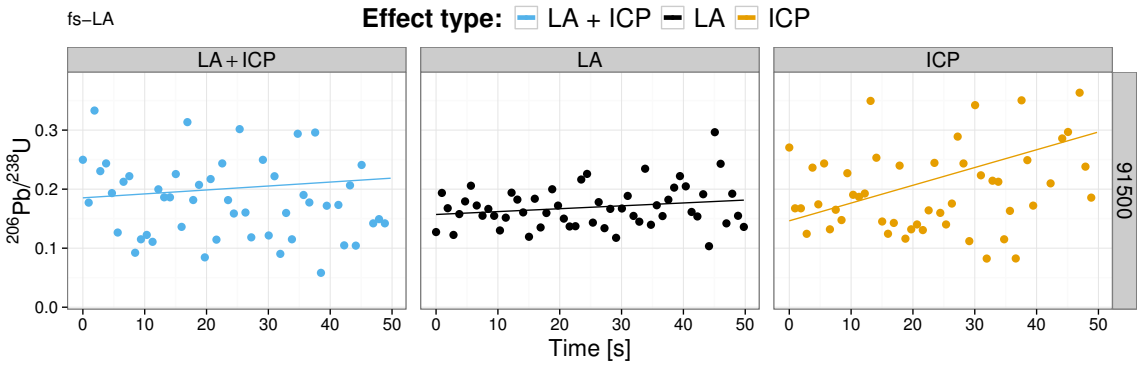

Figure 4.11.: Point-by-point $^{206}Pb/^{238}U$ plots for fs-LA corresponding to Figure 4.2

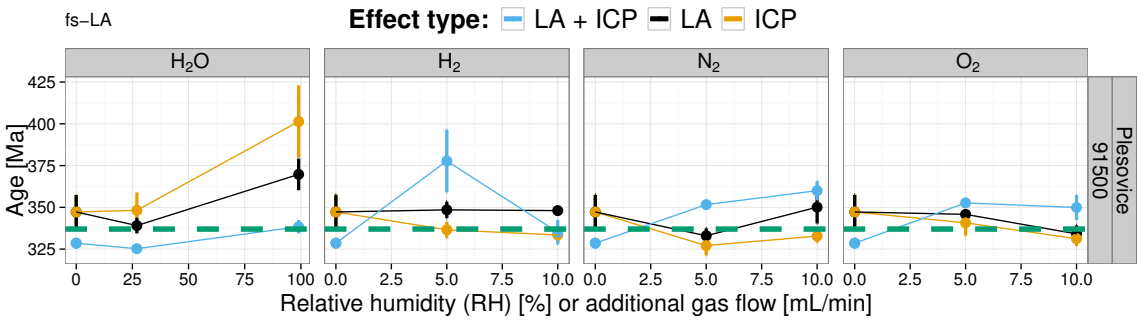

Figure 4.12.: $^{206}Pb/^{238}U$-based ages determined by fs-LA-ICPMS of Plešovice zircon using 91500 as external standard for calibration. Green dashed lines highlight the reference age. Data points represent the mean of 3 to 12 measurements and error bars refer to the 95 % confidence interval of the mean.

4.4. Conclusion

The results of the presented experiments are to a certain extend inconclusive. With ns-LA, no significant improvement of age determination accuracy could be reported with one specific set of operating conditions. Furthermore, the influence of diatomic gases seems to be mainly located at the ICP part of the analytical system, thus changing the system mass bias of the $^{206}Pb/^{238}U$ ratio. An exception is the addition of H_2O. In mode I, the effect in the ICP (system mass bias leading to an increased $^{206}Pb/^{238}U$ ratio) is superimposed by the effect of H_2O in the ablation process, already at 25 % RH but more prominently at 99 % RH.

For fs-LA, the typically reported sensitivity enhancement of extra gases could not be observed for ^{206}Pb and ^{238}U in most of the cases. Mode III behaved in most cases rather like mode II, and not like mode I, indicating that plasma effects of extra gases are not relevant here and that the variations are statistical than a result of an underlying physical process. A change in system mass bias was mainly observed for the addition of N_2 and O_2, whereas a change in down-hole fractionation could be extensively observed with H_2O in mode III

(actually an ICP-effect) and H_2 in mode I (while mode II and III would lower it). For all other conditions the change was reduced or stable. Addition of H_2O seems to reduce the laser-induced fractionation, although no negative slope could be observed.

Concerning the resulting ages, ns-LA was more precise and resulted in less deviation from the accepted value than fs-LA for Plešovice quantified with 91500 as reference. Although in most cases, the extra gas did not change the resulting age drastically, at some conditions (5 mL/min O_2 mode I, 10 mL/min N_2 mode III) deviations up to 11 % occurred. This indicates that with careful optimisation even at non-optimal conditions, reasonable results can be obtained. With the addition of H_2O, the situation is not as clear: As previously shown, the presence of H_2O during the ablation process actually changes the ablation behaviour resulting in relative ^{238}U gain. Consequently, an interpolation between 25 % and 99 % RH in mode I could lead to an improved result. With fs-LA 99 % RH mode I and 5 mL/min H_2 mode III, addition met the accepted age very well; however, the system mass bias and the down-hole fractionation were enlarged rather than reduced. This weakens the results insofar as the underlying physical processes are rather fragile and a robust age determination is not guaranteed. Non-matrix matched calibration seems to be even less promising, as the fractionation behaviour of NIST 610 is even more different.

The main feature of fs-LA, the production of smaller particles that are stoichiometrically close to the bulk material composition, has been reported mainly for conducting material.[157,158] For non-conducting material, Ohata *et al.* reported no significant improvement in accuracy of the quantified concentrations. The relative deviations from the accepted values are larger for NIR-fs-LA than UV-fs-LA, but generally similar to ns-LA, when Ca was used as internal standard.[111] Other studies found an increased fractionation of main elements in generated particle sizes for zircon with IR- and UV-fs-LA than for ns-LA,

probably as a result of the phase explosion during fs-LA.[67] In light of these reports, the findings of this work extends the range of experiments to isotopic analysis and U-Pb age determination in zircons. A fs-LA-system, as used here, with a Gaussian beam profile seems to have no better performance on non-conducting samples. The development of homogenised fs-LA beams could be step a to more stable ablation conditions. But from the experiments presented in this work, a 193 nm ns-LA system without any gas addition is recommended instead of any other combination.

5. Selective Oxide Formation in La-Ba Analysis with ICPMS

Initial work presented in this chapter has been done in collaboration with Oliver Frei, TU Bergakademie Freiberg, Germany, and Stefan Kradolfer during his semester project at ETH Zurich.

5.1. Mass Separation on m/z 138

To use the $^{138}La/^{138}Ba$ decay system for age determination geologists have to rely on cation exchange chromatography to separate Ba isotopes from lanthanide isotopes.[11] Afterwards both fractions have to be measured separately with the respective time and effort. An online-separation of those elements would ease the analysis procedure tremendously and also enable the use of transient sample introduction systems to the ICPMS.

As the aim of this part of the work was to find a way to separate ^{138}Ba from ^{138}La and ^{138}Ce in an on-line fashion, it is important to find means to quantify the separation. The various isotopic abundances only allow for some masses to be measured without any interferences (see Figure 5.1) and only those can be used for a simple estimation. Taking

into account the need for a sufficiently high signal to obtain a stable ratio, ^{137}Ba, ^{139}La and ^{140}Ce are the isotopes that could be used.

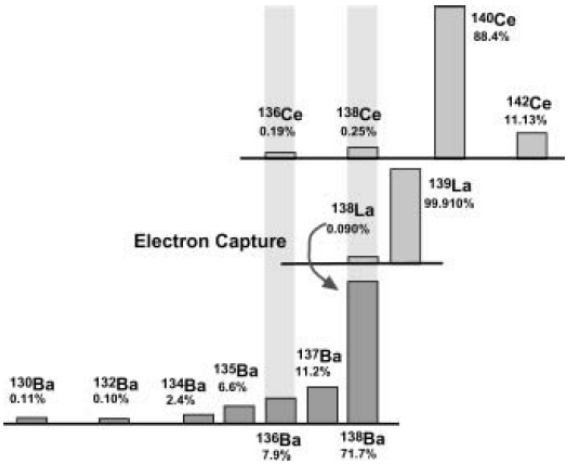

Figure 5.1.: Overview of various isotopic interferences on Ba by La and Ce, from [12]

5.1.1. Considerations on Separation

As presented by Hirata, O_2 addition to the ICP can be used to suppress the La signal while maintaining reasonably high Ba signal.[12]

The reason for this separation effect is the difference in bond dissociation energies (La–O 798 kJ/mol, Ce–O 790 kJ/mol vs. Ba–O 562 kJ/mol).[§] When the bond energy is higher the molecule will be formed to a higher degree. Given the temperature of the ICP to be approximately 10 000 K (equals to an energy of 83.14 kJ/mol) present O should be first forming the lanthanide oxides and later on also some BaO. But to draw this conclusion all other possible species scavenging the O have to be considered, in particular the O itself forming O_2 again (O–O 498 kJ/mol). This effect was already reported in studies

§ All bond dissociation energies in this section are taken from ref[159]

investigating pulsed laser depositin (PLD) under oxygen addition.[160] As we are looking at ionised species in ICPMS it is also useful to consider the dissociation energies of diatomic metal-oxygen species: La–O^+ 875 kJ/mol, Ce–O^+ 852 kJ/mol, O–O^+ 648 kJ/mol vs. Ba–O^+ 441 kJ/mol. From the perspective of diatomic cations, Ba–O^+ is the least preferred ion discussed here and in particular the bond energy is less than for oxygen. Consequently, the formation of BaO is thermodynamically unfavoured in the present conditions and an online-separation seems feasible.

As the bond energies with O for La and Ce are very close and also other thermodynamic properties are very similar, the following experiments were done with a mixture of Ba and La to reduce the complexity of the system.

5.1.2. Quantitative Estimation

To evaluate the separation between La and Ba, one could think of comparing the sensitivities of both elements. The sensitivity is formally defined as

$$S = \frac{I}{C} \tag{5.1}$$

with S being the sensitivity, I the intensity of the analyte and C the concentration of the analyte. As it is actually the aim to evaluate the influence of ^{138}La on ^{138}Ba, it is useful to look at the sensitivities of the isotopes:

$$S_{\mathrm{iso}} = \frac{I_{\mathrm{iso}}}{C_{\mathrm{iso}}} \tag{5.2}$$

When the isotope abundance x_{iso} and the total concentration C of the analyte element are known, S_{iso} and I_{iso} can be expressed as follows:

$$S_{iso} = \frac{I_{iso}}{x_{iso} \cdot C} \tag{5.3}$$

$$I_{iso} = S_{iso} \cdot x_{iso} \cdot C \tag{5.4}$$

As it is not possible to distinguish between ^{138}Ba and ^{138}La with a mass resolution below 73630, the intensity ratio can be estimated with the help of isotopic abundances of the respective isotopes and the signal intensities of the isotopes without interferences (^{139}La and ^{137}Ba):

$$\frac{I_{La}^{138}}{I_{Ba}^{138}} = \underbrace{\frac{x_{Ba}^{137}}{x_{Ba}^{138}} \cdot \frac{x_{La}^{138}}{x_{La}^{139}}}_{\text{conversion factor}} \cdot \frac{I_{La}^{139}}{I_{Ba}^{137}} \tag{5.5}$$

This intensity ratio is useful for evaluation of one solution with a fixed concentration ratio of La and Ba. To generalise this idea to different element concentration ratios (C_{Ba}/C_{La}), isotopic sensitivity ratios can be used:

$$\frac{S_{La}^{138}}{S_{Ba}^{138}} = \underbrace{\frac{x_{Ba}^{137}}{x_{Ba}^{138}} \cdot \frac{x_{La}^{138}}{x_{La}^{139}} \cdot \frac{I_{La}^{139}}{I_{Ba}^{137}}}_{eq.\ (5.5)} \cdot \frac{x_{Ba}^{138}}{x_{La}^{138}} \cdot \frac{C_{Ba}}{C_{La}} \tag{5.6}$$

With Equation (5.6) it is possible to compare different methods on samples with different concentrations, basically a criterion for performance. With Equation (5.5), however, the actual influence or error from ^{138}La on ^{138}Ba is estimated. With this value, the maximum bias on the age determination can be assessed for a specific sample.

5.2. Results on ICP-Q-MS

As a proof of concept, measurements with single-element solutions (SESs) and multi-element solutions (MESs) have been conducted on an Agilent 7500cs, as this system allows for an easy way to investigate the relevant parameters: (i) it is possible to record signals with a broad dynamic range; (ii) during optimisation of the instrument, ratios can be monitored directly on-line; and (iii) the determination of oxide ratios can be done within one measurement cycle. The relevant settings for operation can be found in Table 5.1.

Table 5.1.: General settings for La-Ba studies using quadrupole ICPMS

Parameter	Setting value
	ICPMS
Instrument	Agilent 7500 cs, quadrupole ICPMS
RF-power range	600 - 1400 W
	Additional instruments
Solution introduction	1. Scott spray chamber (Agilent) MicroFlow nebulizer (100 µL/min) (“wet conditions”) 2. DSN 100, Nu Instruments (“dry conditions”)
O_2 flow control	0-100 mL/min ANALYT-MTC
	Data acquisition
Monitored signals	^{136}(Ba,Ce), ^{137}Ba, ^{138}(Ba,La,Ce), ^{139}La, ^{140}Ce ^{152}(BaO,CeO), ^{153}BaO, ^{154}(BaO,LaO,CeO), ^{155}LaO, ^{156}CeO
	Gas flows
Desolvator	approximately 1.3 L/min
Humidified Ar	0.1 L/min
O_2	up to 2 mL/min

5.2.1. Observation for Single Elements

In order to test the selective oxidation of La over Ba for cool plasma conditions, similar experiments as reported by Hirata[12] have been conducted (see Figure 5.2). His results

could be reproduced qualitatively for both elements. The oxide ratios of La and Ba increased with cool plasma, and $^{139}La^{16}O^+/^{139}La^+$ increased disproportionately to $^{138}Ba^{16}O^+/^{138}Ba^+$. Looking at the obtained values, though, at an RF-power of 600 W, the $^{139}La^{16}O^+/^{139}La^+$ was almost 10 times lower and $^{138}Ba^{16}O^+/^{138}Ba^+$ was about 100 times higher than reported here. Hirata indicated that the operating conditions of the system were modified for low-power operation (reduced nebulizer gas flow and solution uptake rate and higher spray chamber temperature), and that the optimisation was based on maximum signal intensity for ^{138}Ba. Under these conditions, the results are even less congruent. As can be seen in Figure 5.3, when tuning on maximum intensity for ^{138}Ba, almost no change in oxide rates was measured for 600 - 900 W RF-power, and low oxide rates was obtained. Although the oxide rate did not seem the same for all Ba isotopes at 1400 W, at lower power and with the addition of O_2 under dry conditions the ratios converge.

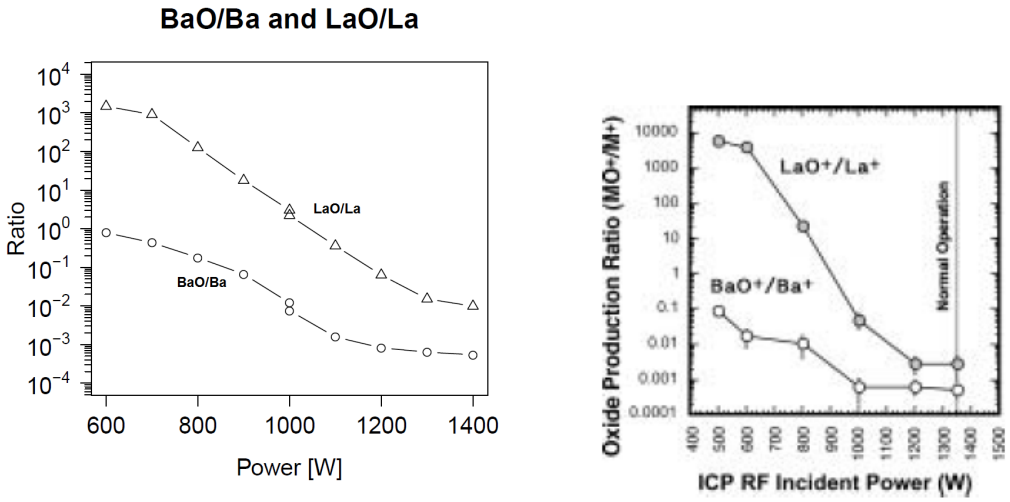

(a) (b)

Figure 5.2.: Comparison of the results of this work with the values of Hirata.[12] The system was tuned at 1400 W and the power successively reduced. $^{138}Ba^{16}O^+/^{138}Ba^+$ and $^{139}La^{16}O^+/^{139}La^+$ ratios are shown.

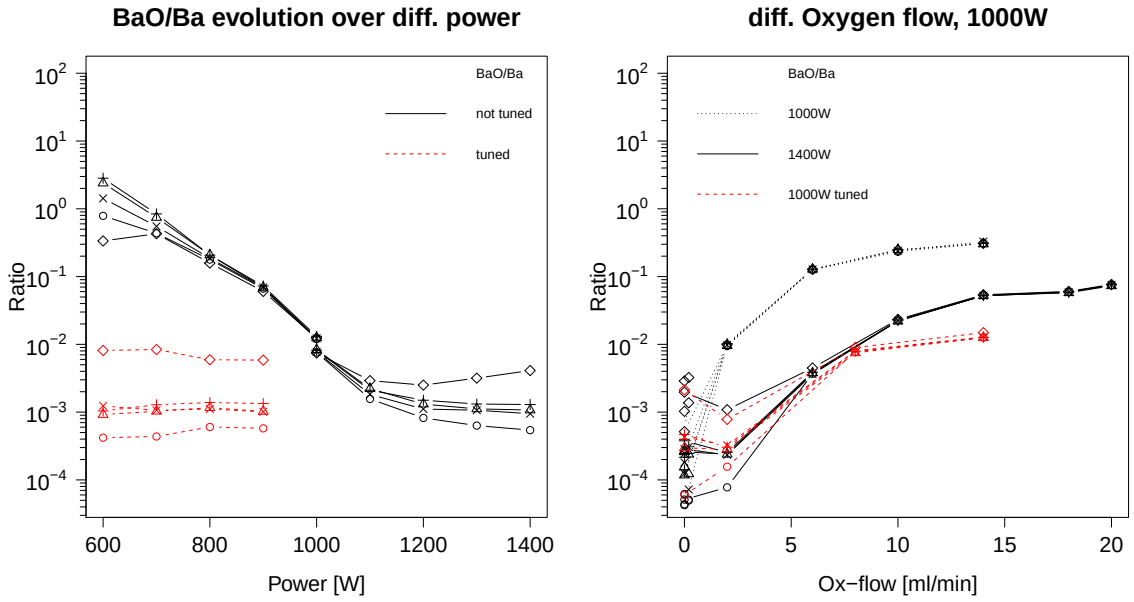

Figure 5.3.: Evolution of $^{M}Ba^{16}O^{+}/^{M}Ba^{+}$ ratios. Left: changing RF-power with wet conditions; right: changing O_2 addition to dry conditions at 1000 or 1400 W. Not tuned: tuning on maximum ^{138}Ba was done at 1400 W and power later decreased; tuned: tuning on maximum ^{138}Ba at each power level.

Under dry conditions, the oxide ratio for Ba increased up to 3 and 4 orders of magnitude for 1400 and 1000 W, respectively. This indicates with low plasma power and O_2 addition, the oxide rate could be increased even more than with low plasma power and wet conditions. With the addition 12 mL/min O_2 in dry mode, an oxide rate similar to a 100 W cooler plasma in wet mode could be achieved. This is beneficial, as higher plasma power results in a more robust ICP. For even higher additions only small increases were measured, and the oxide rate seemed to converge to a limit.

La showed a similar trend as Ba, when the RF-power was decreased (Figure 5.4). Unlike Ba the difference between the oxide ratios of the two La isotopes was growing for RF-powers below 1100 W with a 50 µg/kg solution. The reason for this phenomenon can be

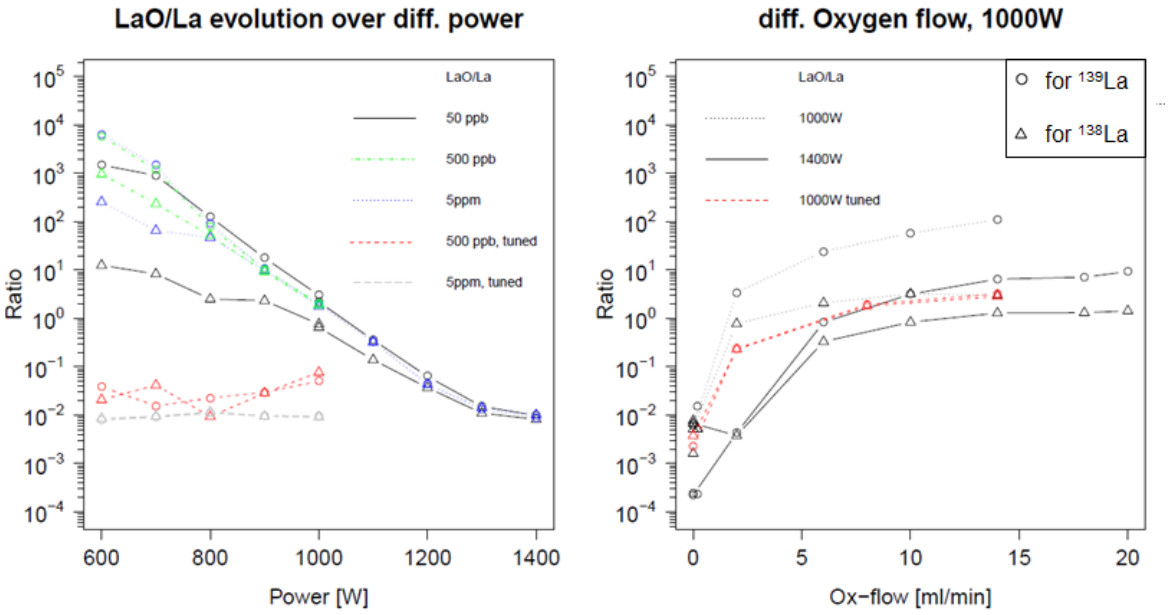

Figure 5.4.: Evolution of $^{M}La^{16}O^{+}/^{M}La^{+}$ ratios. Left: changing RF-power with wet conditions; right: changing O_2 addition to dry conditions at 1000 or 1400 W. Not tuned: tuning on maximum ^{138}Ba was done at 1400 W and power later decreased; tuned: tuning on maximum ^{138}Ba at each power level.

found in the low signal intensity for ^{138}La, which was already at background level in those measurements and, therefore, remained constant while ^{154}LaO increased. For solutions with higher concentrations of 500 and 5000 µg/kg this effect was reduced to a factor of 10.

This background or *low signal effect* was again visible with an O_2 addition larger than 2 mL/min. In total, the oxide rate of La at 1000 W and 14 mL/min O_2 is over 100 times higher than for Ba without re-tuning at this condition.

When humidified Ar is mixed with the carrier gas from the desolvator to increase the RH, an increase of 3 orders of magnitude was visible (see Figure 5.5). With the addition of O_2 there is no difference between humidified and dry carrier gas anymore. O_2 is in this respect more effective than H_2O vapour.

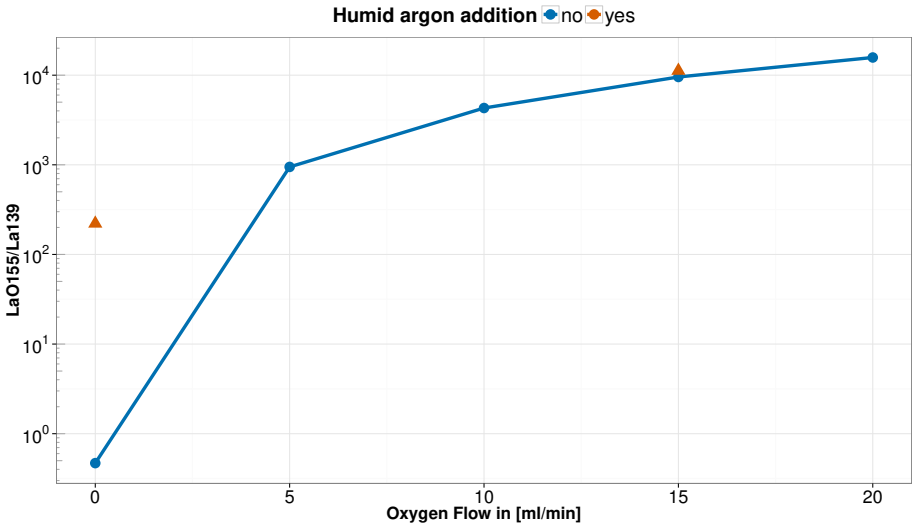

Figure 5.5.: $^{139}La^{16}O^+/^{139}La^+$ at 600 W at different oxygen levels and re-humidified carrier gas

5.2.2. Observation for Mixtures

As a consequence of these findings the way of tuning was changed from *maximum* ^{138}Ba *intensity* to *minimum* $^{139}La/^{137}Ba$ *while still maintaining reasonable* ^{137}Ba *intensity* using a mixed solution of La and Ba with 50 µg/kg of each.

To finally estimate the influence of ^{138}La on ^{138}Ba according to Equation (5.4) MESs with total Ba:La concentration ratios of 1:1, 1:100, and 1:1000 have been measured. The results are shown in Figure 5.6. It can be seen that influence calculated from the measured ^{139}La/^{137}Ba ratio of MESs (left column) matches very well with the calculated one for SESs (right column). This means that the approximation of the SES could be taken as valid.

The middle column shows the actual $I_{\mathrm{La}}^{138}/I_{\mathrm{Ba}}^{138}$ from separate measurements of a Ba and La SES. For contributions higher than 0.1 % the curves matched well with the two other columns; for lower contributions this was not the case. It turned out that these

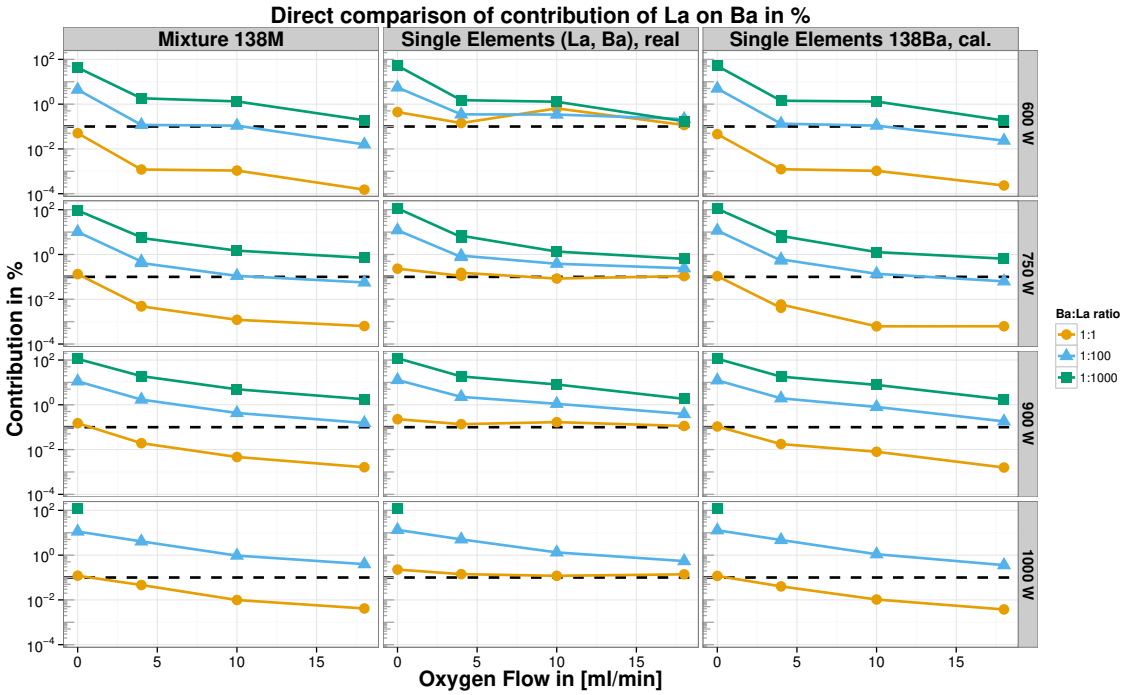

Figure 5.6.: Influence matrix of in % of ^{138}La on ^{138}Ba.

measurements also exhibit the *low signal effect*, *i.e.* a ^{138}La signal on background level. In total, the calculated contributions are valid and can be taken as a good estimate to evaluate a method for specific minerals and ages. To overcome the *low signal effect*, higher concentrations of Ba (more than 50 µg/kg) have to be used, while maintaining the desired Ba:La concentration ratio.

5.3. Results on ICP-MC-MS

Although quadrupole ICPMS allowed proof of concept experiments, it was not possible to achieve the required precision on isotope ratios (0.1 % to 0.005 %) with it. A NuPlasma MC-ICPMS can be used to obtain this high precision ratios and, therefore, the findings of

Section 5.2 (*i.e.* O_2 addition to dry aerosol and optimisation strategy based on $^{139}La/^{137}Ba$ ratio) have been transferred to a multicollector system (see Table A.1). As the multiple faraday cup and SEM detectors are in a fixed position for the standard detector block, two possible configurations for the relevant m/z can be found in Table 5.2. In configuration **A**, all interesting m/z masses are focused on faraday cups and, therefore, allow a simple measurement cycle without any cross detector calibration. It is also advantageous to have all m/z of the system (cf. Figure 5.1) monitored in one cycle.

Table 5.2.: Overview of two reasonable possible detector configurations for MC-ICPMS. The numbers represent the nominal m/z of the isotopes. H, L: faraday cups, IC: SEM detectors

Conf.	H6	H5	H4	H3	H2	H1	Ax	L1	L2	IC0	L3	IC1	L4	IC2	L5
A	–	142	140	139	138	137	136	135	134	–	132	–	130	–	–
B	–	–	–	–	–	–	142	–	140	139	138	137	136	135	–

All experiments on the NuPlasma have been conducted under dry conditions with DSN-100 as desolvator. MESs have been prepared with 50 µg/kg Ba and 50 to 50 000 µg/kg La. The calculated contribution on m/z 138 obtained can be found in Figures 5.7 and 5.8. The tuning has been done without any O_2 addition either on ^{137}Ba maximum sensitivity (series 1) or to a low $^{139}La/^{137}Ba$ ratio (series 2 and 3). One disadvantage of the NuPlasma software is the missing option to observe an ratio directly, so this could not be done with a numerical minimum target as with the Agilent software.

In comparison with the results shown in Figure 5.6, the contribution of ^{138}La on ^{138}Ba is generally lower than with the Agilent. For 1000 W and 10 mL/min O_2 addition (1:100 Ba:La ratio), the contribution was 1 % for the Agilent, and 0.06 % for the NuPlasma at higher power level of 1300 W for 10 mL/min O_2 (1:100 Ba:La).

Some points on the graphs are not present because of negative ratios (700 W for 1:1

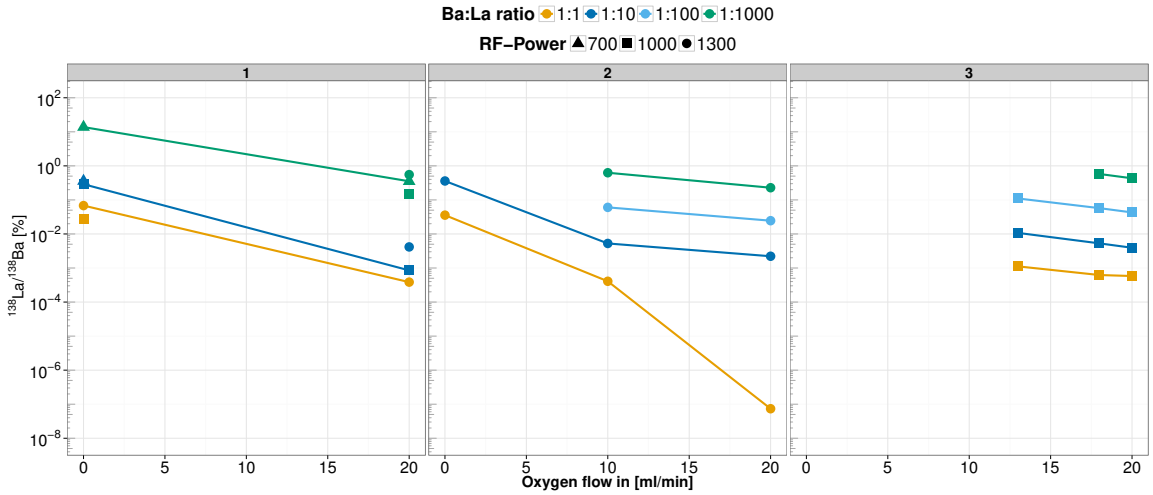

Figure 5.7.: Contribution of ^{138}La on ^{138}Ba with two different optimisation strategies, and detector configuration. Series 1: **A**, tuned on maximum ^{137}Ba at 0 mL/min O_2; series 2: **A**, tuned on minimum ^{139}La/^{137}Ba ratio; series 3: **B**, tune on minimum ^{139}La/^{137}Ba ratio

and 1:10 at 10 mL/min O_2, and 1000 W, 1:1, 20 mL/min O_2), which is due to background level signal for ^{139}La that is needed for the estimation of contribution. This illustrates that the lower dynamic range hinders the estimation of performance for certain data points, although the reduction is quite effective for others, even at normal, *hot* plasma conditions. The extreme low contribution at series 2, 20 mL/min O_2, is also due to low ^{139}La ($< 5 \cdot 10^{-6}$V). At the other side of the dynamic range, solutions with high La concentration and without O_2 addition could not be measured, as the upper limit of the detector is at 10 V, which was exceeded at 5000 µg/kg under normal conditions.

Although this problems with low signal existed, Figure 5.8 shows clearly that the influence is linear in a loglog plot, and, therefore, sensitivities ratios (Equation (5.6)) determined with one solution can be transferred to solutions with higher or lower concentrations. The dynamic range in terms of simultaneously measurable La:Ba concentration ratios of this method is thus 4 orders of magnitude, when the right as long as the sample introduction is

adapted to avoid a ^{139}La signal that is too high or too low.

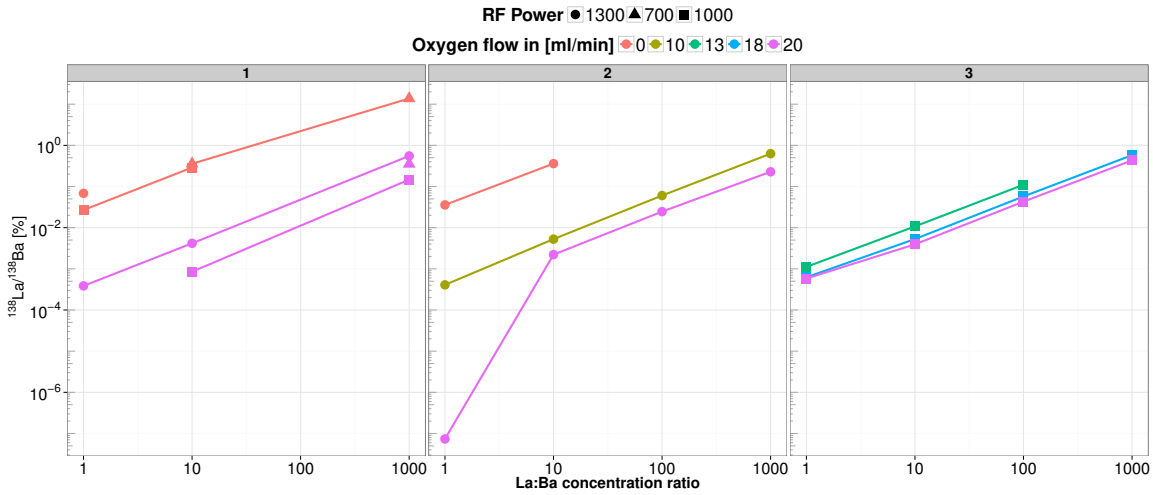

Figure 5.8.: Contribution of ^{138}La on ^{138}Ba with same data as in Figure 5.7, but with La:Ba ratio on x-axis.

To check whether it is possible to use the ion counter (IC) SEM detectors to cope with the low signal, configuration **B** was used (series 3‡ in Figure 5.7). ^{139}La was focused on an SEM no measurement without O_2 addition was conducted, as there would be an immediate overload of the detectors. The general performance on reduction of contribution is in the same order of magnitude as with 1300 W in **A**. This leads to the conclusion that the influence of plasma power is not that important with NuPlasma as compared to the Agilent at high O_2 load.

‡ Series 3 is marked as 1000 W power for visibility reason in the plot, but the experiments have been conducted at 1025 W as sensitivity was tuned to avoid saturation.

5.4. Capabilities of the Method

The results for the oxidation-based separation of La and Ba can be applied to *real world* samples to assess its potential applicability for age determination. Concentrations and determined ages for concrete samples have been taken from Nakai *et al.*[11] Both bastnaesite minerals contain approximately the same amount of La (180 g/kg), while the Ba content is different (K1: 351.1 and N1: 12.95 mg/kg). This results in a Ba:La total concentration ratio of 1:511 and 1:14200, respectively. The sensitivity from the ICP-Q-MS experiments for a Ba:La ratio of 1:1000 was used, which is the highest one measured in the solution experiments, but only resembles K1 and not N1. RF-Powers of 600, 750 and 900 W and an addition of 18 mL/min O_2 have been the basis for the calculations in Table 5.3.

Table 5.3.: Error of ^{138}La on ^{138}Ba for two different minerals. The concentrations and ages of the minerals are taken from Nakai *et al.*[11]. The calculated error is just the contribution because of mass interference of ^{138}La. No further error sources have been considered.

	First mineral, K1 La: 17.94 %, Ba: 351.1 ppm 583.3±49.9 Ma (8.6 %)		Second mineral, N1 La: 18.41 %, Ba: 12.95 ppm 586.4±4 Ma (0.7 %)	
18 mL/min O_2				
900 W	52.5 Ma	9.0 %	1496.3 Ma	250 %
750 W	20.9 Ma	3.6 %	584.9 Ma	100 %
600 W	0.6 Ma	0.1 %	16 Ma	2.7 %

For K1 , it was possible to obtain results that were similar to the uncertainty (8.6 %) of the given value (9.0 % 900 W) or even below (down to 0.1% for 600 W). So the contribution of ^{138}La would only account for 1.2 % of the total uncertainty.

For N1, the resulting biases on the age because of ^{138}La interference is much higher than for K1 (2.7 % to 250 %), while the reported uncertainty is only 0.7 %.

5.5. Conclusion

The experiments with wet sample introduction on the Agilent qualitatively reproduced the results by Hirata[12] in terms of selective oxidation of La over Ba. Differences in the result could be explained by the impossibility of matching the tuning parameters exactly. The introduction of desolvated aerosol with additional O_2 proved to be even more efficient for the separation, as similar low contribution from ^{138}La on ^{138}Ba could be measured at higher plasma powers. The addition of 12 mL/min O_2 allowed for the use of 100 W more in comparison to wet conditions, which facilitates a higher plasma stability.

The power reduction was not as important with the NuPlasma because there was already at 1300 W a reduction comparable to 900 W with the Agilent when O_2 was added. This is advantageous, as plasma stability is still an important factor for the measured ratios, even though simultaneous detection takes place.

A rough estimate on report values of bastnaesite samples showed that the developed method would not raise the uncertainty on the determined age much when the La:Ba ratio does not exceed 1000:1. For higher ratios, the analytical error on Ba is lower if a separation is done with chromatography beforehand.

In further studies, the method should be tested with a LA system and solid samples. These should be compared to the digested and chromatographically separated solutions of the same minerals.

6. Conclusion

In this presented work three objectives were realised:

- An experimental setup was assembled to investigate the effects of extra gas addition to the carrier gas on the signals in LA-ICPMS independent of the mixing point before or after the ablation chamber.
- This setup was used to study laser-induced and plasma-induced fractionation under the influence of H_2, N_2, O_2 and H_2O for a ns-LA and a fs-LA system.
- A method enabling the selective oxidation of La versus Ba in the ICP for dry aerosol was developed, which is based on the addition of O_2 to the carrier gas.

A GED was inserted between the ablation chamber and the ICPMS in a conventional LA-ICPMS setup. With this combination, the gas mixture present during the ablation process could be exchanged to Ar. During this exchange procedure, the laser generated particles were preserved in the gas stream and transported into the ICP. To monitor the plasma conditions and to tune the instruments independently of the LA conditions, metallic gas was additionally mixed to the carrier gas using the MGG. The influence of gas mixtures could be investigated in three different modes, namely on the LA, on the ICP or combined on the over-all fractionation.

The ICP was found to be the primary point of influence for gas addition (H_2, N_2, O_2 and H_2O) while using ns-LA. Moderate addition (5 mL/min) enhanced the signal intensity up to a factor of 2 for Pb or U. The system mass bias – the effective fractionation in the ICPMS – was shifted to higher $^{206}Pb/^{238}U$ ratios for H_2O and H_2 and lower values for N_2 and O_2. H_2, N_2 and O_2 showed no significant effect on the laser-induced down-hole fractionation. The slope of the linear regression of the $^{206}Pb/^{238}U$ over ablation time – and indicator of fractionation – did not change significantly. However, with the addition of H_2O instead the positive slope decreased and turned negative. Humidity in the carrier gas influenced the ablation and the vaporisation in the plasma in a way, that these two effects could cancel each other out. Aerosol generated by fs-LA is less influenced in the ICP by extra gases and only for H_2O and O_2 a signal enhancement up to a factor of 1.3 and 1.6 for ^{206}Pb and ^{238}U, respectively, could be observed. $^{206}Pb/^{238}U$ ratios were shifted to lower values for N_2 but increased for H_2 and H_2O. Down-hole fractionation was similar to teh results obtained with ns-LA, which were not influenced by extra gas with the exception H_2O. Here, the slope was reduced when H_2O was added to the ablation chamber, and increased when added only to the ICP. Determined ages of Plešovice zircon with 91500 as reference material exhibit a variation of ±2.5 % deviation from the accepted age. Fs-LA produced generally higher deviations of ±3.5 %, which might originate from the lower signal intensities. From the presented results, ns-LA without any extra gases still remains the recommended system to use for U-Pb age determination, although the problem of down-hole fractionation is not yet solved. Fs-LA was not able to produce a $^{206}Pb/^{238}U$ ratio in the ICP which closer resembles the bulk ratio in glass or zircon than for ns-LA. Improvements in stoichiometric sampling with fs-LA seem to be limited to conducting material.

A selective oxidation of La over Ba could be realised with low plasma power with SN, but

not with dry aerosol. However, this is necessary for the application of LA-ICPMS for La-Ba age determination, as ^{138}La has to be separated from ^{138}Ba on mass ^{138}M. Laser-generated aerosol was simulated by desolvation of single- and multi-element solutions of La and Ba. O_2 addition to this aerosol was first investigated on a quadrupole ICPMS as proof of concept. The highest suppression factor could be reached with 600 W RF-power and 18 % O_2 addition. Consequently the contribution of ^{138}La on ^{138}M was reduced by a factor of 1000, resulting in 0.1 % for a La:Ba concentration ratio of 1000:1. This method was transferred to MC-ICPMS and similar suppression factors were already reached at normal RF-power settings of 1300 W. The choice of two detector configurations ^{139}La focused either on a faraday cup or on an ion counter allows us to determine age with high or low La signal, respectively. Further research to adapt this findings for LA-ICPMS is required to enable an easy use of La-Ba age dating in geochronology.

7. Bibliography

[1] Boltwood, B. B. *Am J Sci* **1907**, *s4-23*, 78–88.

[2] Thompson, W. *Phil. Mag* **1899**, *47*, 66–90.

[3] Nier, A. O. *Phys. Rev.* **1939**, *55*, 150–153.

[4] Larsen, E. S.; Keevil, N. B.; Harrison, H. C. *Geological Society of America Bulletin* **1952**, *63*, 1045–1052.

[5] Krogh, T. E. *Geochimica et Cosmochimica Acta* **1982**, *46*, 637–649.

[6] Compston, W.; Williams, I. S.; Meyer, C. *J. Geophys. Res.* **1984**, *89*, B525–B534.

[7] Andersen, C. A.; Hinthorne, J. R. *Earth and Planetary Science Letters* **1972**, *14*, 195–200.

[8] Gray, A. L. *Analyst* **1985**, *110*, 551–556.

[9] Nakai, S.; Masuda, A.; Shimizu, H.; Lu, Q. *Economic Geology* **1989**, *84*, 2296–2299.

[10] Nakai, S.; Shimizu, H.; Masuda, A. *Nature* **1986**, *320*, 433–435.

[11] Nakai, S.; Masuda, A.; Lehmann, B. *Am. Miner.* **1988**, *73*, 1111–1113, WOS:A1988Q602900014.

[12] Hirata, T. *Journal of the Mass Spectrometry Society of Japan* **2004**, *52*, 171–176.

[13] Tsukahara, R.; Kubota, M. *Spectrochimica Acta Part B: Atomic Spectroscopy* **1990**, *45*, 581–589.

[14] Patterson, C.; Tilton, G.; Inghram, M. *Science* **1955**, *121*, 69–75.

[15] Kinny, P. D.; Compston, W.; Williams, I. S. *Geochimica et Cosmochimica Acta* **1991**, *55*, 849–859.

[16] Elburg, M. A. In *Isotopic Analysis*; Vanhaecke, F., Degryse, P., Eds.; Wiley-VCH Verlag GmbH & Co. KGaA, 2012; pp 235–274.

[17] Aldrich, L. T.; Nier, A. O. *Phys. Rev.* **1948**, *74*, 1590–1594.

[18] Steiger, R. H.; Jäger, E. *Earth and Planetary Science Letters* **1977**, *36*, 359–362.

[19] Bouvier, A.; Vervoort, J. D.; Patchett, P. J. *Earth and Planetary Science Letters* **2008**, *273*, 48–57.

[20] Selby, D.; Creaser, R. A.; Stein, H. J.; Markey, R. J.; Hannah, J. L. *Geochimica et Cosmochimica Acta* **2007**, *71*, 1999–2013.

[21] Allegre, C. J.; Sutcliffe, C. *Isotope Geology*; Cambridge University Press: Cambridge, 2008.

[22] Fryer, B. J.; Jackson, S. E.; Longerich, H. P. *Can Mineral* **1995**, *33*, 303–312.

[23] Košler, J. *Proceedings of the Geologists' Association* **2007**, *118*, 19–24.

[24] Sylvester, P., Ed. *Laser Ablation-ICPMS in the Earth SciencesPrinciples and Applications*; MAC Short Course 29; Mineralogical Association of Canada, 2001.

[25] Sylvester, P. *Laser Ablation–ICP–MS in the Earth Sciences CURRENT PRACTICES AND OUTSTANDING ISSUES*; MAC Short Course 40; Mineralogical Association of Canada, 2008.

[26] Outridge, P. M.; Doherty, W.; Gregoire, D. C. *Spectrochimica Acta Part B: Atomic Spectroscopy* **1997**, *52*, 2093–2102.

[27] Kuhn, H.-R.; Guillong, M.; Günther, D. *Anal Bioanal Chem* **2003**, *378*, 1069–1074.

[28] Horn, I.; Günther, D. *Applied Surface Science* **2003**, *207*, 144–157.

[29] Günther, D.; Heinrich, C. A. *J. Anal. At. Spectrom.* **1999**, *14*, 1363–1368.

[30] Košler, J.; Fonneland, H.; Sylvester, P.; Tubrett, M.; Pedersen, R.-B. *Chemical Geology* **2002**, *182*, 605–618.

[31] Eggins, S. M.; Kinsley, L. P. J.; Shelley, J. M. G. *Applied Surface Science* **1998**, *127-129*, 278–286.

[32] Mank, A. J. G.; Mason, P. R. D. *J. Anal. At. Spectrom.* **1999**, *14*, 1143–1153.

[33] Jeffries, T. E.; Jackson, S. E.; Longerich, H. P. *J. Anal. At. Spectrom.* **1998**, *13*, 935–940.

[34] Guillong, M.; Horn, I.; Günther, D. *J. Anal. At. Spectrom.* **2003**, *18*, 1224–1230.

[35] Jeong, S. H.; Borisov, O. V.; Yoo, J. H.; Mao, X. L.; Russo, R. E. *Anal. Chem.* **1999**, *71*, 5123–5130.

[36] Horn, I.; Guillong, M.; Günther, D. *Applied Surface Science* **2001**, *182*, 91–102.

[37] Russo, R. E.; Mao, X.; Gonzalez, J. J.; Mao, S. S. *J. Anal. At. Spectrom.* **2002**, *17*, 1072–1075.

[38] Koch, J.; Bohlen, A. v.; Hergenröder, R.; Niemax, K. *J. Anal. At. Spectrom.* **2004**, *19*, 267–272.

[39] Chichkov, B. N.; Momma, C.; Nolte, S.; Alvensleben, F. v.; Tünnermann, A. *Appl. Phys. A* **1996**, *63*, 109–115.

[40] Storey, C. D.; Smith, M. P.; Jeffries, T. E. *Chemical Geology* **2007**, *240*, 163–181.

[41] Thomson, S. N.; Gehrels, G. E.; Ruiz, J.; Buchwaldt, R. *Geochem. Geophys. Geosyst.* **2012**, *13*, Q0AA21.

[42] Chew, D. M.; Sylvester, P. J.; Tubrett, M. N. *Chemical Geology* **2011**, *280*, 200–216.

[43] Willigers, B. J. A.; Baker, J. A.; Krogstad, E. J.; Peate, D. W. *Geochimica et Cosmochimica Acta* **2002**, *66*, 1051–1066.

[44] Kohn, M. J.; Corrie, S. L. *Earth and Planetary Science Letters* **2011**, *311*, 136–143.

[45] Simonetti, A.; Heaman, L. M.; Chacko, T.; Banerjee, N. R. *International Journal of Mass Spectrometry* **2006**, *253*, 87–97.

[46] Sun, J.; Yang, J.; Wu, F.; Xie, L.; Yang, Y.; Liu, Z.; Li, X. *Chin. Sci. Bull.* **2012**, *57*, 2506–2516.

[47] Spencer, K. J.; Hacker, B. R.; Kylander-Clark, A. R. C.; Andersen, T. B.; Cottle, J. M.; Stearns, M. A.; Poletti, J. E.; Seward, G. G. E. *Chemical Geology* **2013**, *341*, 84–101.

[48] Gregory, C. J.; Rubatto, D.; Allen, C. M.; Williams, I. S.; Hermann, J.; Ireland, T. *Chemical Geology* **2007**, *245*, 162–182.

[49] Smith, S. R.; Foster, G. L.; Romer, R. L.; Tindle, A. G.; Kelley, S. P.; Noble, S. R.; Horstwood, M.; Breaks, F. W. *Contrib Mineral Petrol* **2004**, *147*, 549–564.

[50] Zack, T.; Stockli, D. F.; Luvizotto, G. L.; Barth, M. G.; Belousova, E.; Wolfe, M. R.; Hinton, R. W. *Contrib Mineral Petrol* **2011**, *162*, 515–530.

[51] Andersen, T. *Chemical Geology* **2002**, *192*, 59–79.

[52] Chipley, D.; Polito, P. A.; Kyser, T. K. *American Mineralogist* **2007**, *92*, 1925–1935.

[53] Zong, K.; Chen, J.; Hu, Z.; Liu, Y.; Li, M.; Fan, H.; Meng, Y. *Sci. China Earth Sci.* **2015**, *58*, 1731–1740.

[54] Souders, A. K.; Sylvester, P. J. *J. Anal. At. Spectrom.* **2010**, *25*, 975–988.

[55] Jochum, K. P.; Stoll, B.; Weis, U.; Jacob, D. E.; Mertz-Kraus, R.; Andreae, M. O. *Geostand Geoanal Res* **2014**, *38*, 265–292.

[56] Allen, C. M.; Campbell, I. H. *Chemical Geology* **2012**, *332–333*, 157–165.

[57] Kuhn, B. K.; Birbaum, K.; Luo, Y.; Günther, D. *J. Anal. At. Spectrom.* **2010**, *25*, 21–27.

[58] Košler, J.; Wiedenbeck, M.; Wirth, R.; Hovorka, J.; Sylvester, P.; Míková, J. *J. Anal. At. Spectrom.* **2005**, *20*, 402–409.

[59] Hoskin, P. W. O.; Schaltegger, U. In *Zircon*; Hanchar, J. M., Hoskin, P. W. O., Eds.; Mineralogical Soc America: Washington, 2003; Vol. 53; pp 27–62, WOS:000189199900002.

[60] Wetherill, G. W. *Eos Trans. AGU* **1956**, *37*, 320–326.

[61] Black, L. P.; Williams, I. S.; Compston, W. *Contr. Mineral. and Petrol.* **1986**, *94*, 427–437.

[62] Kaiser, A.; Lobert, M.; Telle, R. *Journal of the European Ceramic Society* **2008**, *28*, 2199–2211.

[63] Fryer, B. J.; Jackson, S. E.; Longerich, H. P. *Chemical Geology* **1993**, *109*, 1–8.

[64] Solari, L. A.; Gómez-Tuena, A.; Bernal, J. P.; Pérez-Arvizu, O.; Tanner, M. *Geostandards and Geoanalytical Research* **2010**, *34*, 5–18.

[65] Kooijman, E.; Berndt, J.; Mezger, K. *European Journal of Mineralogy* **2012**, *24*, 5–21.

[66] Hirata, T.; Kon, Y. *Analytical Sciences* **2008**, *24*, 345–353.

[67] Glaus, R.; Kaegi, R.; Krumeich, F.; Günther, D. *Spectrochimica Acta Part B: Atomic Spectroscopy* **2010**, *65*, 812–822.

[68] Bleiner, D.; Günther, D. *J. Anal. At. Spectrom.* **2001**, *16*, 449–456.

[69] Frei, D.; Gerdes, A. *Chemical Geology* **2009**, *261*, 261–270.

[70] Pullen, A.; Ibáñez-Mejía, M.; Gehrels, G. E.; Ibáñez-Mejía, J. C.; Pecha, M. *J. Anal. At. Spectrom.* **2014**, *29*, 971–980.

[71] Košler, J.; Sláma, J.; Belousova, E.; Corfu, F.; Gehrels, G. E.; Gerdes, A.; Horstwood, M. S. A.; Sircombe, K. N.; Sylvester, P. J.; Tiepolo, M.; Whitehouse, M. J.; Woodhead, J. D. *Geostandards and Geoanalytical Research* **2013**, *37*, 243–259.

[72] Horn, I.; Rudnick, R. L.; McDonough, W. F. *Chemical Geology* **2000**, *164*, 281–301.

[73] Fisher, C. M.; Longerich, H. P.; Jackson, S. E.; Hanchar, J. M. *J. Anal. At. Spectrom.* **2010**, *25*, 1905–1920.

[74] Paton, C.; Woodhead, J. D.; Hellstrom, J. C.; Hergt, J. M.; Greig, A.; Maas, R. *Geochem. Geophys. Geosyst.* **2010**, *11*, Q0AA06.

[75] Košler, J.; Jackson, S. E.; Yang, Z.; Wirth, R. *J. Anal. At. Spectrom.* **2014**, *29*, 832–840.

[76] Tera, F.; Wasserburg, G. J. *Earth and Planetary Science Letters* **1972**, *14*, 281–304.

[77] Gehrels, G. *Annual Review of Earth and Planetary Sciences* **2014**, *42*, 127–149.

[78] Gehrels, G. E.; Valencia, V. A.; Ruiz, J. *Geochem. Geophys. Geosyst.* **2008**, *9*, Q03017.

[79] Sláma, J.; Košler, J.; Condon, D. J.; Crowley, J. L.; Gerdes, A.; Hanchar, J. M.; Horstwood, M. S. A.; Morris, G. A.; Nasdala, L.; Norberg, N.; Schaltegger, U.; Schoene, B.; Tubrett, M. N.; Whitehouse, M. J. *Chemical Geology* **2008**, *249*, 1–35.

[80] GeoRem Database, Version 12, 03.01.2011. http://georem.mpch-mainz.gwdg.de.

[81] Black, L. P.; Kamo, S. L.; Williams, I. S.; Mundil, R.; Davis, D. W.; Korsch, R. J.; Foudoulis, C. *Chemical Geology* **2003**, *200*, 171–188.

[82] Paces, J. B.; Jr, J. D. M. *Journal of Geophysical Research* **1993**, *98*, PP. 13,997–14,013.

[83] Wiedenbeck, M.; Allé, P.; Corfu, F.; Griffin, W. L.; Meier, M.; Oberli, F.; Quadt, A. v.; Roddick, J. C.; Spiegel, W. *Geostandards Newsletter* **1995**, *19*, 1–23.

[84] Black, L. P.; Gulson, B. L. *BMR Journal of Australien Geology & Geophysics* **1978**, 227–232.

[85] Jackson, S. E.; Pearson, N. J.; Griffin, W. L.; Belousova, E. A. *Chemical Geology* **2004**, *211*, 47–69.

[86] Stern, R. A. *Radiogenic Age and Isotopic Studies: Report 14*; Geological Survey of Canada, 2001.

[87] Black, L. P.; Kamo, S. L.; Allen, C. M.; Davis, D. W.; Aleinikoff, J. N.; Valley, J. W.; Mundil, R.; Campbell, I. H.; Korsch, R. J.; Williams, I. S.; Foudoulis, C. *Chemical Geology* **2004**, *205*, 115–140.

[88] Black, L. P.; Kamo, S. L.; Allen, C. M.; Aleinikoff, J. N.; Davis, D. W.; Korsch, R. J.; Foudoulis, C. *Chemical Geology* **2003**, *200*, 155–170.

[89] Houk, R. S.; Fassel, V. A.; Flesch, G. D.; Svec, H. J.; Gray, A. L.; Taylor, C. E. *Anal. Chem.* **1980**, *52*, 2283–2289.

[90] Montaser, A. *Inductively coupled plasmas in analytical atomic spectrometry*, second ed. ed.; VCH Publishers etc: New York, New York, 1992.

[91] Montaser, A. *Inductively coupled plasma mass spectrometry*; Wiley-VCH: New York etc, 1998.

[92] Reed, T. B. *Journal of Applied Physics* **1961**, *32*, 821–824.

[93] Greenfield, S.; Jones, I. L.; Berry, C. T. *Analyst* **1964**, *89*, 713–720.

[94] Wendt, R. H.; Fassel, V. A. *Anal. Chem.* **1965**, *37*, 920–922.

[95] Olesik, J. W.; Fister, J. C. *Spectrochimica Acta Part B: Atomic Spectroscopy* **1991**, *46*, 851–868.

[96] Guillong, M.; Günther, D. *J. Anal. At. Spectrom.* **2002**, *17*, 831–837.

[97] Aeschliman, D. B.; Bajic, S. J.; Baldwin, D. P.; Houk, R. S. *J. Anal. At. Spectrom.* **2003**, *18*, 1008–1014.

[98] Mattauch, J.; Herzog, R. *Z. Physik* **1934**, *89*, 786–795.

[99] Frick, D. A. *Fundamental studies on laser ablation inductively coupled plasma mass spectrometry for improved quantitative imaging of biomaterials*; ETH-Zürich: Zürich, 2014.

[100] Johnson, E. G.; Nier, A. O. *Phys. Rev.* **1953**, *91*, 10–17.

[101] Günther, D.; Hattendorf, B. *TrAC Trends in Analytical Chemistry* **2005**, *24*, 255–265.

[102] Figg, D.; Kahr, M. S. *Applied Spectroscopy* **1997**, *51*, 1185–1192.

[103] Günther, D.; Frischknecht, R.; Heinrich, C. A.; Kahlert, H.-J. *J. Anal. At. Spectrom.* **1997**, *12*, 939–944.

[104] Pécheyran, C.; Cany, S.; Chabassier, P.; Mottay, E.; Donard, O. F. X. *J. Phys.: Conf. Ser.* **2007**, *59*, 112.

[105] Yokoyama, T. D.; Suzuki, T.; Kon, Y.; Hirata, T. *Anal. Chem.* **2011**, *83*, 8892–8899.

[106] Wälle, M.; Koch, J.; Tabersky, D.; Hametner, K.; Zhigadlo, N. D.; Katrych, S.; Karpinski, J.; Günther, D. *J. Anal. At. Spectrom.* **2010**, *25*, 193–195.

[107] Pisonero, J.; Koch, J.; Wälle, M.; Hartung, W.; Spencer, N. D.; Günther, D. *Anal. Chem.* **2007**, *79*, 2325–2333.

[108] Jenner, G. A.; Foley, S. F.; Jackson, S. E.; Green, T. H.; Fryer, B. J.; Longerich, H. P. *Geochimica et Cosmochimica Acta* **1993**, *57*, 5099–5103.

[109] Stuart, B. C.; Feit, M. D.; Herman, S.; Rubenchik, A. M.; Shore, B. W.; Perry, M. D. *Phys. Rev. B* **1996**, *53*, 1749–1761.

[110] Lorazo, P.; Lewis, L. J.; Meunier, M. *Phys. Rev. Lett.* **2003**, *91*, 225502.

[111] Ohata, M.; Tabersky, D.; Glaus, R.; Koch, J.; Hattendorf, B.; Günther, D. *J. Anal. At. Spectrom.* **2014**, *29*, 1345–1353.

[112] Tabersky, D.; Nishiguchi, K.; Utani, K.; Ohata, M.; Dietiker, R.; Fricker, M. B.; Maddalena, I. M. d.; Koch, J.; Günther, D. *J. Anal. At. Spectrom.* **2013**, *28*, 831–842.

[113] Nishiguchi, K.; Utani, K.; Fujimori, E. *J. Anal. At. Spectrom.* **2008**, *23*, 1125–1129.

[114] Kovacs, R.; Nishiguchi, K.; Utani, K.; Günther, D. *J. Anal. At. Spectrom.* **2010**, *25*, 142–147.

[115] Dorta, L.; Kovacs, R.; Koch, J.; Nishiguchi, K.; Utani, K.; Günther, D. *J. Anal. At. Spectrom.* **2013**, *28*, 1513–1521.

[116] Hattendorf, B.; Günther, D. In *Handbook of Spectroscopy*; Gauglitz, G., Moore, D. S., Eds.; Wiley-VCH Verlag GmbH & Co. KGaA, 2014; pp 647–698.

[117] Durrant, S. F. *Fresenius J Anal Chem* **1993**, *347*, 389–392.

[118] Montaser, A.; Hoven, R. L. V.; Barnes, R. M. *C R C Critical Reviews in Analytical Chemistry* **1987**, *18*, 45–103.

[119] Sesi, N. N.; Mackenzie, A.; Shanks, K. E.; Yang, P.; Hieftje, G. M. *Spectrochimica Acta Part B: Atomic Spectroscopy* **1994**, *49*, 1259–1282.

[120] Hutton, R. C. *J. Anal. At. Spectrom.* **1986**, *1*, 259–263.

[121] Hu, Z.; Gao, S.; Liu, Y.; Hu, S.; Chen, H.; Yuan, H. *J. Anal. At. Spectrom.* **2008**, *23*, 1093–1101.

[122] Craig, J. M.; Beauchemin, D. *J. Anal. At. Spectrom.* **1992**, *7*, 937–942.

[123] Evans, E. H.; Ebdon, L. *J. Anal. At. Spectrom.* **1990**, *5*, 425–430.

[124] Hill, S. J.; Ford, M. J.; Ebdon, L. *J. Anal. At. Spectrom.* **1992**, *7*, 1157–1165.

[125] Ebdon, L.; Ford, M.; Hutton, R.; Hill, S. *Appl. Spectrosc.* **1994**, *48*, 507–516, WOS:A1994NK68700014.

[126] Jakubowski, N.; Feldmann, I.; Stuewer, D. *J. Anal. At. Spectrom.* **1993**, *8*, 969–977.

[127] Minnich, M. G.; Houk, R. S. *J. Anal. At. Spectrom.* **1998**, *13*, 167–174.

[128] Witte, T. M.; Houk, R. *Spectrochimica Acta Part B: Atomic Spectroscopy* **2012**, *69*, 9–19.

[129] Vaughan, M. A.; Horlick, G. *Appl. Spectrosc., AS* **1986**, *40*, 434–445.

[130] Vaughan, M.-A.; Horlick, G.; Tan, S. H. *J. Anal. At. Spectrom.* **1987**, *2*, 765–772.

[131] Guillong, M.; Heinrich, C. A. *J. Anal. At. Spectrom.* **2007**, *22*, 1488–1494.

[132] Košler, J.; Longerich, H. P.; Tubrett, M. N. *Anal Bioanal Chem* **2002**, *374*, 251–254.

[133] Frick, D. A.; Günther, D. *J. Anal. At. Spectrom.* **2012**, *27*, 1294–1303.

[134] Connor, C. O.; Sharp, B. L.; Evans, P. *J. Anal. At. Spectrom.* **2006**, *21*, 556–565.

[135] Wälle, M.; Koch, J.; Günther, D. *J. Anal. At. Spectrom.* **2008**, *23*, 1285–1289.

[136] Flamigni, L.; Koch, J.; Günther, D. *J. Anal. At. Spectrom.* **2014**, *29*, 280–286.

[137] van de Sande, M. J.; van Eck, P.; Sola, A.; Gamero, A.; van der Mullen, J. J. A. M. *Spectrochimica Acta Part B: Atomic Spectroscopy* **2003**, *58*, 457–467.

[138] Tabersky, D. Fundamental and applied studies on large and heterogeneous samples using LA-ICP-MS under atmospheric pressure air. Ph.D. thesis, ETH-Zürich, Zürich, 2014.

[139] Schramel, P. *Z. Anal. Chem.* **1985**, *320*, 233–236.

[140] Hutton, R. C.; Eaton, A. N. *J. Anal. At. Spectrom.* **1987**, *2*, 595–598.

[141] Lam, J.; Horlick, G. *Spectrochimica Acta Part B: Atomic Spectroscopy* **1990**, *45*, 1313–1325.

[142] Jakubowski, N.; Feldmann, I.; Stuewer, D. *Spectrochimica Acta Part B: Atomic Spectroscopy* **1992**, *47*, 107–118.

[143] Ross, B. S.; Hieftje, G. M. *Journal of the American Society for Mass Spectrometry* **1992**, *3*, 128–138.

[144] Gustavsson, A. *Spectrochimica Acta Part B: Atomic Spectroscopy* **1987**, *42*, 111–118.

[145] Gustavsson, A. *Spectrochimica Acta Part B: Atomic Spectroscopy* **1988**, *43*, 917–922.

[146] Lam, J. W.; McLaren, J. W. *J. Anal. At. Spectrom.* **1990**, *5*, 419–424.

[147] McLaren, J. W.; Lam, J. W.; Gustavsson, A. *Spectrochimica Acta Part B: Atomic Spectroscopy* **1990**, *45*, 1091–1094.

[148] Tittes, W.; Jakubowski, N.; Stüwer, D.; Tölg, G.; Broekaert, J. A. C. *J. Anal. At. Spectrom.* **1994**, *9*, 1015–1020.

[149] Halicz, L.; Günther, D. *J. Anal. At. Spectrom.* **2004**, *19*, 1539–1545.

[150] Luong, E. T.; Houk, R. S.; Serfass, R. E. *J. Anal. At. Spectrom.* **1997**, *12*, 703–708.

[151] Günther, D.; Cousin, H.; Magyar, B.; Leopold, I. *J. Anal. At. Spectrom.* **1997**, *12*, 165–170.

[152] Fricker, M. B. Design of ablation cells for LA-ICP-MS: from modeling to high spatial resolution analysis applications. Ph.D. thesis, ETH, Zürich, 2012.

[153] R Core Team, *R: A Language and Environment for Statistical Computing*; R Foundation for Statistical Computing: Vienna, Austria, 2013.

[154] Wickham, H. *ggplot2: elegant graphics for data analysis*; Springer New York, 2009.

[155] Sylvester, P. J.; Ghaderi, M. *Chemical Geology* **1997**, *141*, 49–65.

[156] Flamigni, L.; Koch, J.; Günther, D. *Spectrochimica Acta Part B: Atomic Spectroscopy* **2012**, *76*, 70–76.

[157] Liu, C.; Mao, X. L.; Mao, S. S.; Zeng, X.; Greif, R.; Russo, R. E. *Anal. Chem.* **2004**, *76*, 379–383.

[158] Liu, C.; Mao, X.; Mao, S. S.; Greif, R.; Russo, R. E. *Anal. Chem.* **2005**, *77*, 6687–6691.

[159] Haynes, W. M., Ed. *CRC Handbook of Chemistry and Physics, 96th Edition*, 96th ed.; CRC Press, 2015.

[160] Chen, J.; Döbeli, M.; Stender, D.; Lee, M. M.; Conder, K.; Schneider, C. W.; Wokaun, A.; Lippert, T. *J. Phys. D: Appl. Phys.* **2016**, *49*, 045201.

A. Appendix

A.1. Analysis Settings

Table A.1.: General settings for La-Ba studies using MC-ICPMS

Parameter	Setting value
	ICPMS
Instrument	NuPlasma, MC-ICPMS
RF-power range	700 - 1300 W
	Additional instruments
Solution introduction	DSN 100, Nu Instruments (“dry conditions”)
O_2 flow control	0-100 mL/min ANALYT-MTC
	Data acquisition
Monitored signals	see Table 5.2
	Gas flows
Desolvator	approximately 1.3 L/min
O_2	up to 2 mL/min

A.2. Additional Graphs

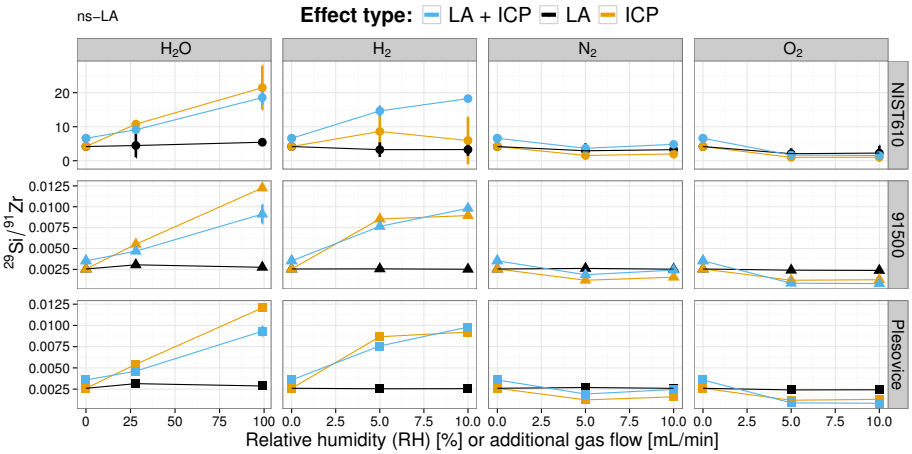

Figure A.1.: $^{29}Si/^{91}Zr$ ratios averaged over an acquisition timeframe of 53 s with ns-LA. Data points represent the mean of 3 to 12 measurements and error bars refer to the 95 % confidence interval of the mean.

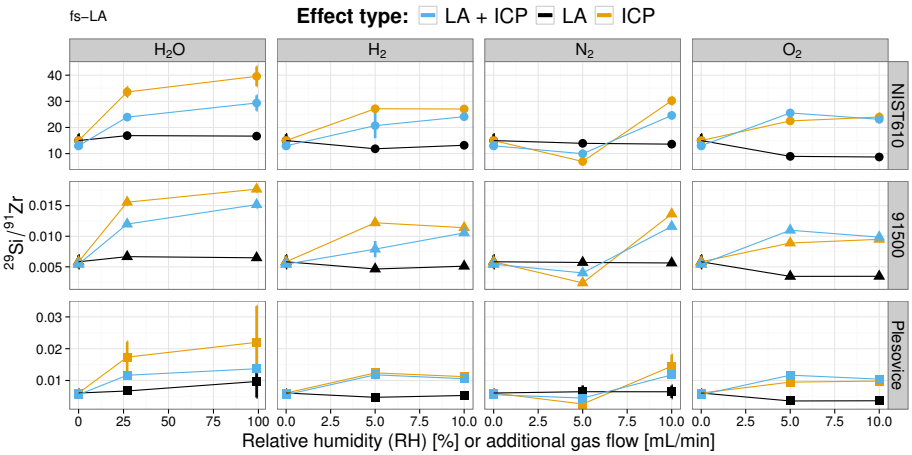

Figure A.2.: $^{29}Si/^{91}Zr$ ratios averaged over an acquisition timeframe of 50 s with fs-LA. Data points represent the mean of 3 to 12 measurements and error bars refer to the 95 % confidence interval of the mean.

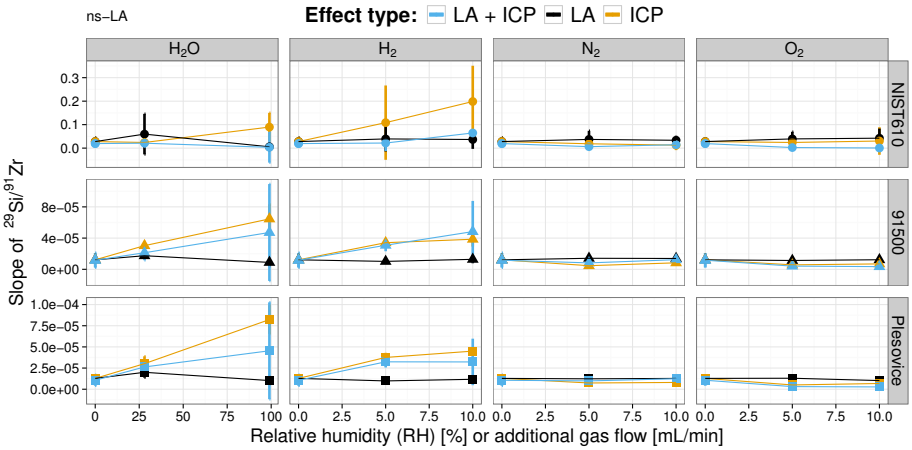

Figure A.3.: ns-LA: Slopes of $^{29}Si/^{91}Zr$ ratios calculated from regression curves of point-by-point plots, as shown in Figure 4.2. Data points represent the mean of 3 to 12 measurements and error bars refer to the 95 % confidence interval of the mean.

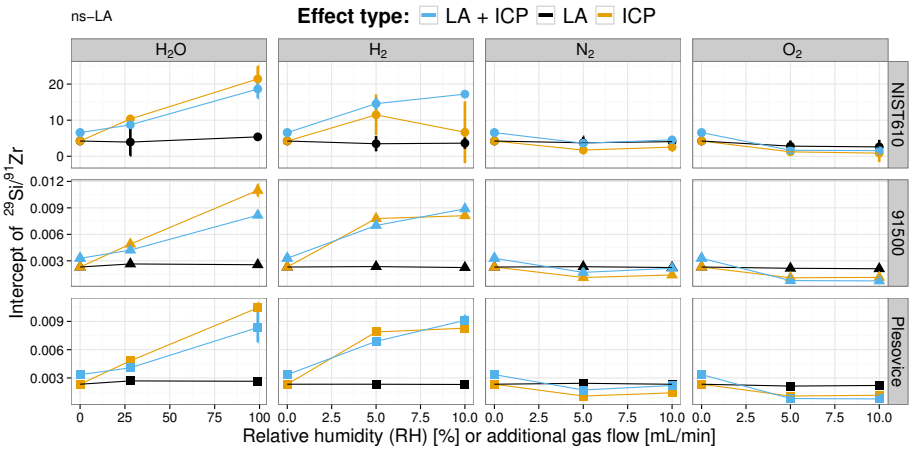

Figure A.4.: ns-LA: Intercepts of $^{29}Si/^{91}Zr$ ratios calculated from regression curves of point-by-point plots, as shown in Figure 4.2. Data points represent the mean of 3 to 12 measurements and error bars refer to the 95 % confidence interval of the mean.

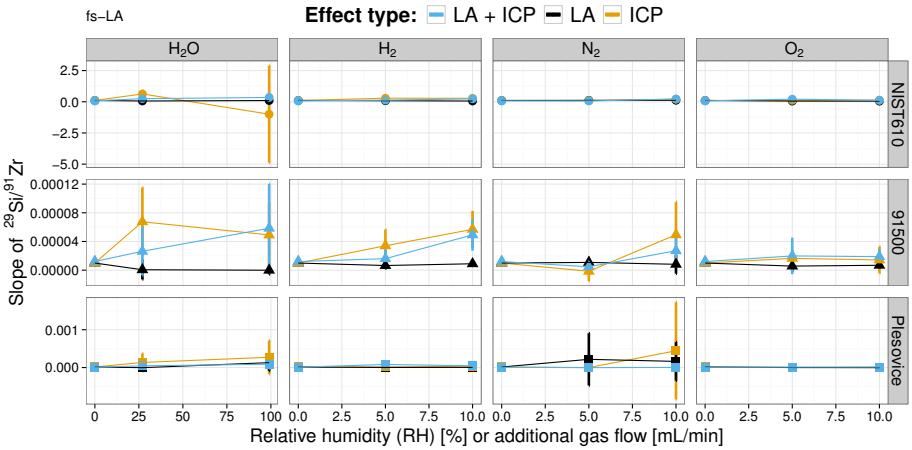

Figure A.5.: fs-LA: Slopes of $^{29}Si/^{91}Zr$ ratios calculated from regression curves of point-by-point plots, as shown in Figure 4.2. Data points represent the mean of 3 to 12 measurements and error bars refer to the 95 % confidence interval of the mean.

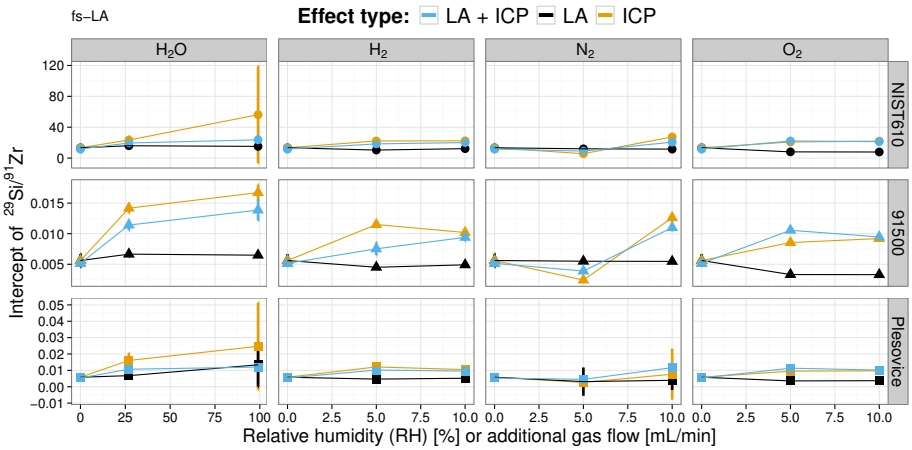

Figure A.6.: fs-LA:Intercepts of $^{29}Si/^{91}Zr$ ratios calculated from regression curves of point-by-point plots, as shown in Figure 4.2. Data points represent the mean of 3 to 12 measurements and error bars refer to the 95 % confidence interval of the mean.

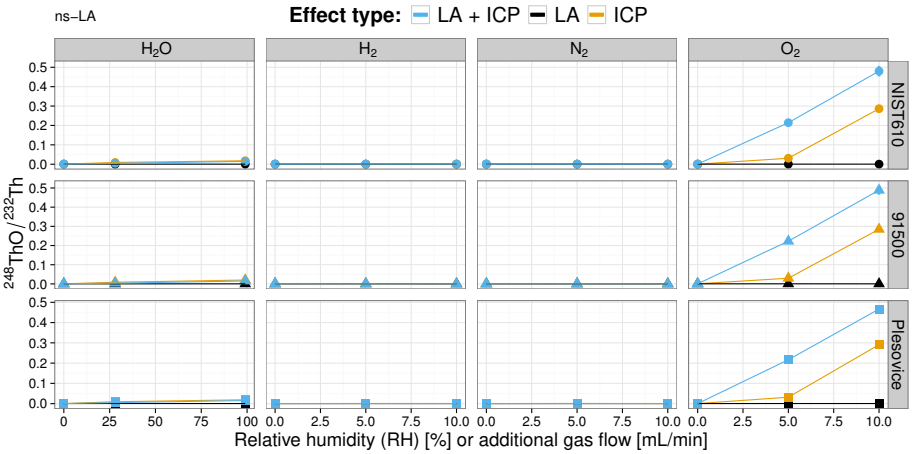

Figure A.7.: $^{232}Th^{16}O/^{232}Th$ ratios averaged over an acquisition timeframe of 53 s with ns-LA. Data points represent the mean of 3 to 12 measurements and error bars refer to the 95 % confidence interval of the mean.

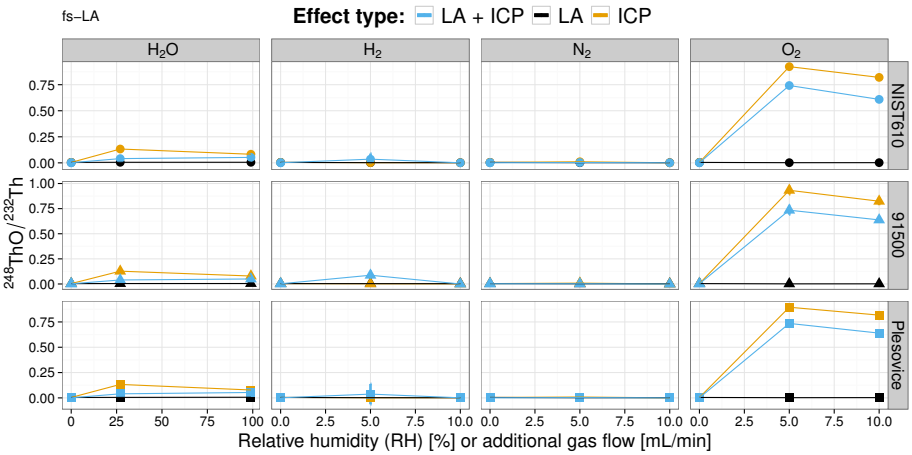

Figure A.8.: $^{232}Th^{16}O/^{232}Th$ ratios averaged over an acquisition timeframe of 50 s with fs-LA. Data points represent the mean of 3 to 12 measurements and error bars refer to the 95 % confidence interval of the mean.

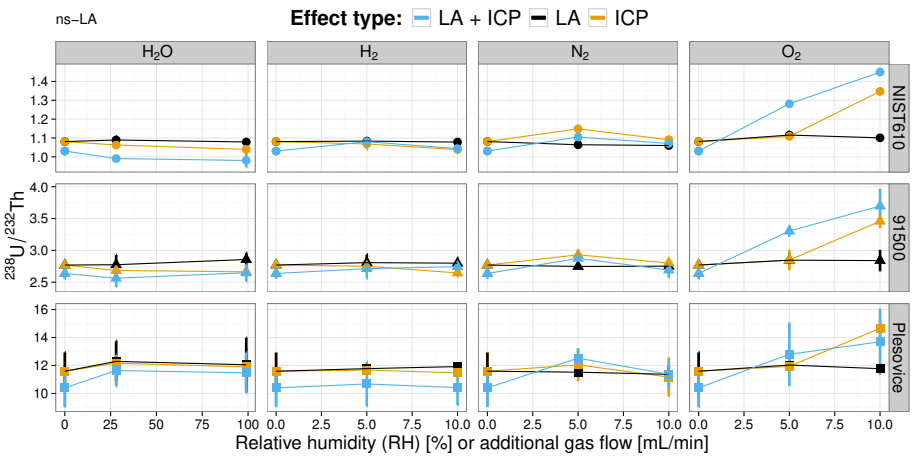

Figure A.9.: $^{238}U/^{232}Th$ ratios averaged over an acquisition timeframe of 53 s with ns-LA. Data points represent the mean of 3 to 12 measurements and error bars refer to the 95 % confidence interval of the mean.

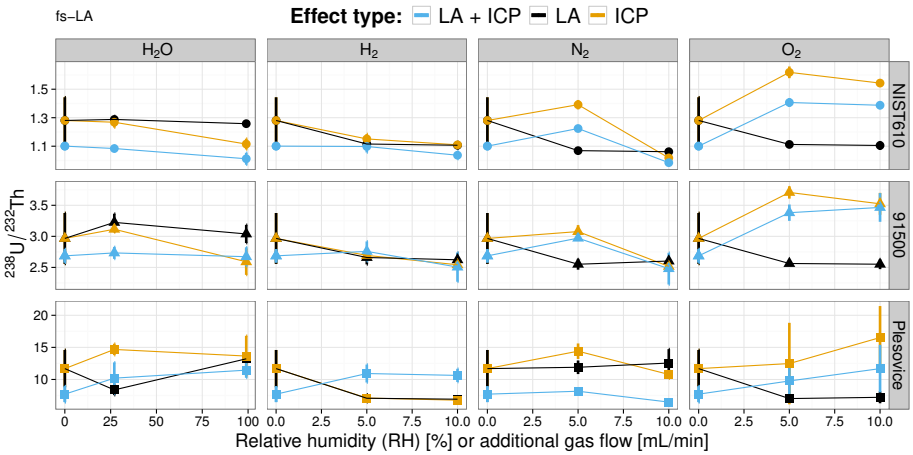

Figure A.10.: $^{238}U/^{232}Th$ ratios averaged over an acquisition timeframe of 50 s with fs-LA. Data points represent the mean of 3 to 12 measurements and error bars refer to the 95 % confidence interval of the mean.

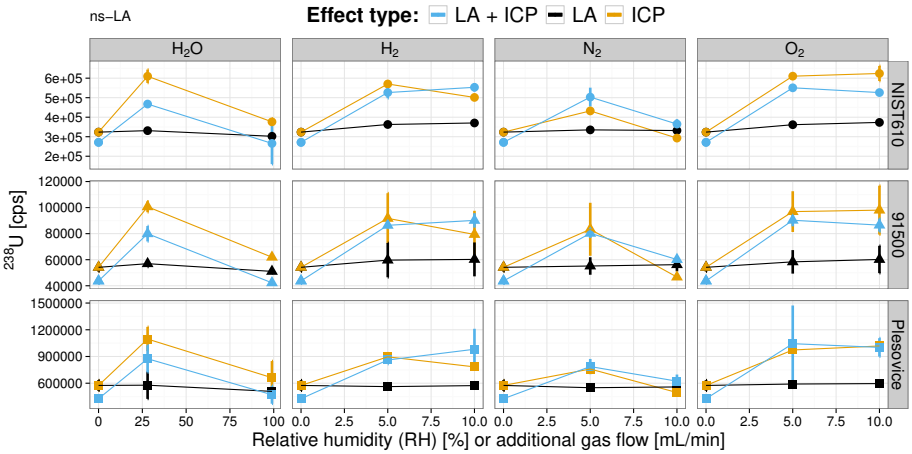

Figure A.11.: ns-laser: ^{238}U signal intensities averaged over an acquisition timeframe of 53 s with ns-LA. Data points represent the mean of 3 to 12 measurements and error bars refer to the 95 % confidence interval of the mean.

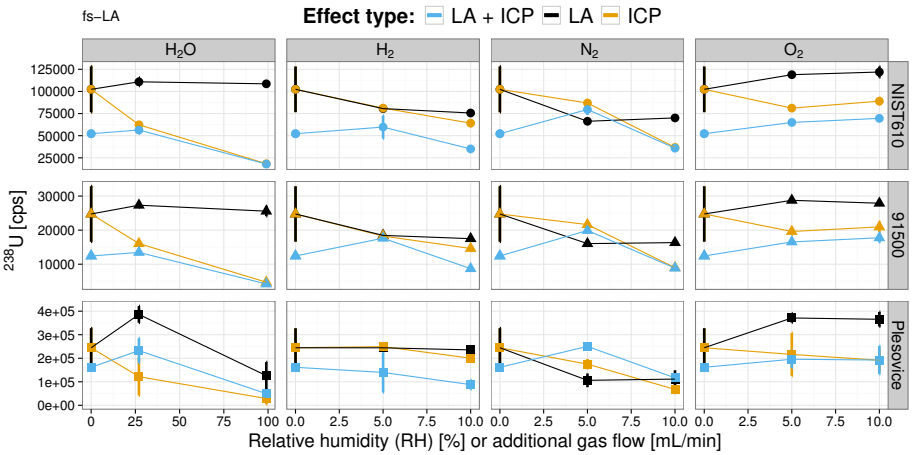

Figure A.12.: fs-laser: ^{238}U signal intensities averaged over an acquisition timeframe of 50 s with fs-LA. Data points represent the mean of 3 to 12 measurements and error bars refer to the 95 % confidence interval of the mean.

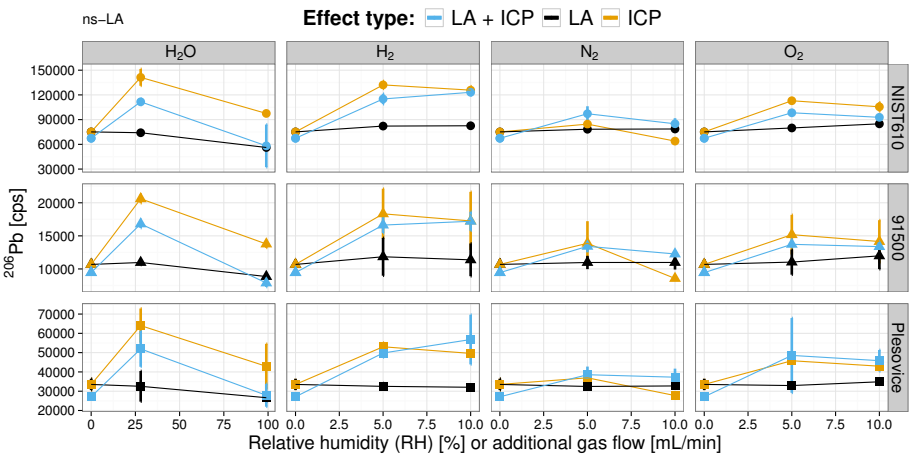

Figure A.13.: ns-laser: ^{206}Pb signal intensities averaged over an acquisition timeframe of 53 s with ns-LA. Data points represent the mean of 3 to 12 measurements and error bars refer to the 95 % confidence interval of the mean.

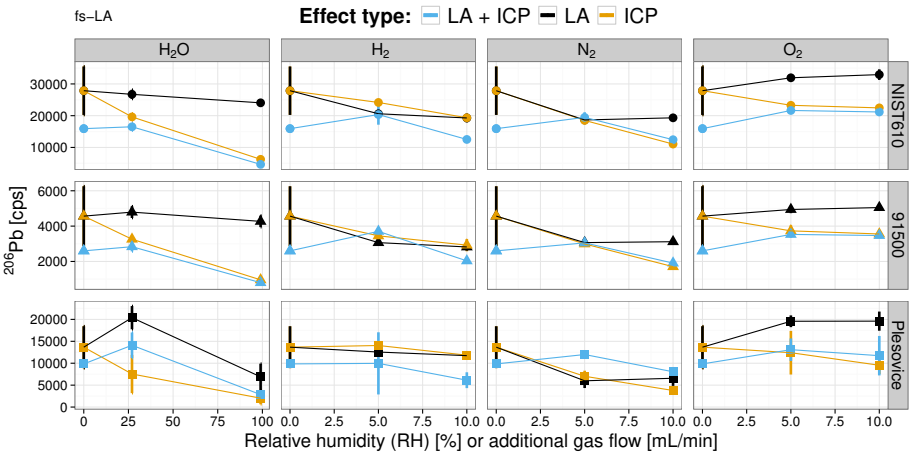

Figure A.14.: fs-laser: ^{206}Pb signal intensities averaged over an acquisition timeframe of 50 s with fs-LA. Data points represent the mean of 3 to 12 measurements and error bars refer to the 95 % confidence interval of the mean.